CASE FILE
COPY

NACA TN No. 1709

NATIONAL ADVISORY COMMITTEE FOR AERONAUTICS

TECHNICAL NOTE

No. 1709

INVESTIGATION OF THE EFFECTS OF A NACELLE ON THE AERODYNAMIC CHARACTERISTICS OF A SWEPT WING AND THE EFFECTS OF SWEEP ON A WING ALONE

By Gerald Hieser and Charles F. Whitcomb

Langley Aeronautical Laboratory
Langley Field, Va.

Washington

October 1948

NATIONAL ADVISORY COMMITTEE FOR AERONAUTICS

TECHNICAL NOTE NO. 1709

INVESTIGATION OF THE EFFECTS OF A NACELLE ON THE AERODYNAMIC CHARACTERISTICS OF A SWEPT WING AND THE EFFECTS OF SWEEP ON A WING ALONE

By Gerald Hieser and Charles F. Whitcomb

SUMMARY

An investigation was conducted to determine the effects of a nacelle on the aerodynamic characteristics of a swept wing and the effects of sweep on a wing alone. The aerodynamic characteristics were determined from force and pressure measurements and tuft studies at Mach numbers of 0.13 to 0.61 for the wing-nacelle combination and at 0.13 to 0.70 for the wing alone. The angle of attack was varied from 0° to the stalling angles at a Mach number of 0.13 and from -1.65° to 6° at the higher Mach numbers.

The results showed that the measured variation of lift-curve slope with sweep angle is in good agreement with theory up to 30° sweep, but at greater sweep angles the theory apparently underestimates the effects of sweep. The presence of the nacelle increased the lift-curve slope about 10 percent with the wing at 45° sweep but decreased the slope slightly at -45° sweep. The nacelle had no effect on the lift-curve slope of the unswept wing. The presence of the nacelle did not appreciably alter the stalling characteristics of the wing at sweep angles of 45° or -45°, but for the unswept wing the addition of the nacelle caused an appreciable reduction in the maximum lift coefficient and in the angle of attack at maximum lift.

In general, for Mach numbers up to 0.61 the drag increment due to the nacelle was lower for the swept configurations than for the unswept configurations.

The addition of the nacelle to the wing reduced the longitudinal stability at all sweep angles. For both the wing alone and the wing-nacelle combination, a marked increase in longitudinal stability resulted from positive sweep, whereas only a small increase was realized for negative sweep (-45°).

When the wing was swept back or swept forward to an angle of 45°, high pressure peaks and adverse pressure gradients occurred near the leading edge of the wing at the acute junction of the wing and nacelle.

INTRODUCTION

Recent investigations have been conducted to evaluate the effects of using sweep as a means of reducing and delaying the adverse effects due to compressibility on the aerodynamic characteristics of a wing.

One of the problems which arises is whether any unfavorable effects occur which tend to lessen or cancel the effects of sweep when a nacelle is added to a swept wing. A study of the effects of wing-nacelle interference at low speeds on a swept wing with various nacelle configurations is given in reference 1.

The purpose of the present investigation is to determine the effects of a nacelle on the aerodynamic characteristics of a swept wing (over a large speed range) and to compare these effects with the results obtained from the unswept wing and nacelle. In addition, the effects of sweep on the aerodynamic characteristics of a wing alone are presented. An NACA 65_2-215 wing in combination with a modified NACA 111 body was tested in the Langley 16-foot high-speed tunnel at sweep angles of 0°, 45°, and -45° for a range of Mach number from 0.13 to 0.61. The wing alone was tested at sweep angles of 0°, 15°, 30°, 45°, and -45° for a range of Mach number from 0.13 to 0.70.

SYMBOLS

A	aspect ratio (b^2/S)
a	speed of sound in air, feet per second
b/2	semispan of model, feet
b'/2	length of quarter-chord line between root and tip chords, feet (fig. 1)
c	section chord of wing parallel to air stream, feet
$\bar{c}$	mean aerodynamic chord measured parallel to air stream, feet (reference 2)
c_r	chord of root section of wing, feet
c_t	chord of tip section of wing, feet
c_Λ	section chord perpendicular to quarter-chord line of original wing, feet
$\bar{c}_\Lambda$	average chord, feet $\left(\frac{c_r' + c_t'}{2}\right)$

c_r' chord at root of wing determined by intersections of wing leading and trailing edges with line perpendicular to quarter-chord line of unswept wing at intersection of root chord of swept wing and quarter-chord line of unswept wing (fig. 1)

c_t' chord at tip of wing determined by intersections of wing leading and trailing edges with line perpendicular to quarter-chord line of unswept wing at intersection of tip chord of swept wing and quarter-chord line of unswept wing (fig. 1)

C_D drag coefficient (D/qS_w)

C_{D_N} nacelle drag coefficient $\left(\frac{S_w}{S_N}\left(C_{D_{\text{wing-nacelle}}} - C_{D_{\text{wing alone}}}\right)\right)$

C_L lift coefficient (L/qS_w)

C_{N_w} wing normal-force coefficient (N/qS_w)

c_n section normal-force coefficient (n/qS_w)

$C_{m_{\bar{c}/4}}$ pitching-moment coefficient about quarter-chord point of mean aerodynamic chord $(M'/q\bar{c}S_w)$

L lift, pounds

D drag, pounds

M' pitching moment about quarter-chord point of mean aerodynamic chord, foot-pounds

n section normal force, pounds

N wing normal force, pounds

q free-stream dynamic pressure, pounds per square foot $\left(\frac{1}{2}\rho V^2\right)$

S_w wing area, square feet

S_N maximum nacelle frontal area, square feet

ρ mass density of free stream, slugs per cubic foot

V free-stream velocity, feet per second

$dC_L/d\alpha$ lift-curve slope

M Mach number (V/a)

M_{cr} critical Mach number

y	spanwise distance along quarter-chord line of original wing, measured from tunnel wall, feet
x	distance in longitudinal plane, feet
l	nacelle length, feet
P	pressure coefficient $\left(\frac{p - p_o}{q}\right)$
p	local static pressure at any point, pounds per square foot
p_o	free-stream static pressure, pounds per square foot
α	angle of attack, corrected for tunnel-wall effects and balance-frame deflection, degrees
α_t	angle of attack, corrected for tunnel-wall effects, degrees
α_g	geometric angle of attack, degrees
Λ	sweep angle between line perpendicular to plane of symmetry and quarter-chord line of unswept wing
η	aspect-ratio-correction factor for lift (reference 3)

MODEL AND APPARATUS

A 10-foot semispan NACA 65_2-215 wing which had a mean chord of 3.33 feet in the unswept configuration was used for the present study in the Langley 16-foot high-speed tunnel. The wing was tapered linearly from a root chord of 4.44 feet to a tip chord of 2.22 feet and had no geometric twist or dihedral. The airfoil sections were perpendicular to the quarter-chord line of the unswept wing. The wing was mounted as a reflection-plane model, and sweep was obtained by pivoting the wing about the 50-percent station of the root chord. A different wing tip was used for each angle of sweep so that the tip was parallel to the tunnel air stream. The spanwise locations of the eight stations of pressure orifices with reference to the intersection of the quarter-chord line and the tunnel wall are given in table I. The chordwise locations are also included. Photographs of the wing mounted in the tunnel at each angle of sweep are shown as figure 2. Table II gives the dimensions of the wing at each angle of sweep.

The nacelle used was a modified NACA 111 solid body (no internal flow) and was mounted at the midsemispan so that its longitudinal axis corresponded with the wing chord line, and the 45-percent-chord station

of the nacelle corresponded with the 50-percent-chord station of the wing. The nacelle coordinates are given in table III. The maximum diameter of the nacelle was 1.18 feet and the length was 7.08 feet. Pressure orifices were located on the nacelle at stations 3/16 inch from the wing surface at the inboard and outboard junctures of the wing and nacelle. Orifices were also located on the nacelle surface in the vertical and horizontal planes through the longitudinal axis of symmetry. Photographs of the wing and nacelle mounted in the tunnel at sweep angles of 45° and -45° are shown as figure 3. A sketch showing the nacelle mounted on the unswept wing is given in figure 4.

In order to allow clearance for deflections of the tunnel balance frame, a gap of 1/2 inch was provided between the tunnel wall and the wing surface. This gap allowed leakage of air between the tunnel test section and the test chamber. In an attempt to reduce the effect of leakage on the flow about the wing, leakage deflection plates were installed on the wing surface. These plates were located 1/2 inch from the tunnel wall and extended 2 inches from the upper and lower surfaces of the wing as shown in figure 5.

Vertical plates were installed on the upper surface of the wing at 45° sweep in an attempt to reduce the cross flow over the wing. These plates were made from $\frac{1}{8}$-inch steel plate and were located parallel to the tunnel air stream at spanwise stations 12, 30, 48, 66, and 84 inches from the root. They were 1/2 inch deep at the 40-percent-chord station and extended to $1\frac{1}{2}$ inches behind the trailing edge. The top edges of the plates were parallel to the wing chord line. The wing with the plates installed is shown in the sketch of figure 6 and in the photograph of figure 7.

A further study of the flow over the wing at 45° sweep was made by comparison of the drag characteristics resulting from a straight vane parallel to the undisturbed tunnel air stream at the midsemispan and a curved vane at the same location. The contour of the curved vane was calculated from measured pressures at the midsemispan by assuming that the induced velocities were imparted only to the air-stream velocity component perpendicular to the quarter-chord line. The measured pressures were obtained at a Mach number of 0.56 and an angle of attack of 6°. Both vanes extended from 1 inch ahead of the leading edge to $1\frac{1}{2}$ inches behind the trailing edge and had a constant depth of 4 inches above the upper-surface contour. Sketches of the wing with the straight and curved vanes installed are shown in figure 8, and photographs of these configurations are presented as figure 9.

TESTS

The variation of Reynolds number with Mach number is given in figure 10 for each angle of sweep. Reynolds number is based on the average chord in the direction of the tunnel air stream.

Pressure and force measurements were obtained for the wing alone at sweep angles of 0°, 15°, 30°, 45°, and -45°, and these tests covered a Mach number range of 0.13 to 0.71. The angle of attack was varied from 0° to the stalling angles at a Mach number of 0.13 and from -1.65° to 6° at the higher Mach numbers.

Tuft studies and force and pressure measurements were obtained for the wing-nacelle combination at sweep angles of 0°, 45°, and -45° for Mach numbers of 0.13, 0.20, 0.40, and 0.61. The angle of attack ranged from 0° to stalling angles at a Mach number of 0.13 and from -1.65° to 6° at the other Mach numbers.

For angles of attack of 0°, 3°, and 6° and Mach numbers of 0.13 and 0.20, force and pressure measurements and tuft studies were obtained with the vertical plates installed on the wing at 45° sweep.

With the straight and curved vanes installed on the wing at 45° sweep, force measurements were obtained at Mach numbers of 0.20 and 0.56 and angles of attack of 5°, 6°, and 7°.

CORRECTIONS

The change in angle of attack due to the deflection of the tunnel balance frame was determined, and the resulting correction was applied to the angle of attack for all data except those for tuft studies and those at a Mach number of 0.13. At this Mach number the correction was negligible.

The angle of attack and all force coefficients were corrected for jet-boundary effects by the reflection-plane method outlined in reference 4. A small correction for drag of the leakage deflection plates was applied; however, no attempt was made to correct the data for possible effects of leakage at the tunnel wall.

RESULTS AND DISCUSSION

Force Characteristics

Lift.- The variation of lift coefficient with angle of attack for the wing alone at Mach numbers from 0.20 to approximately 0.70 and for sweep angles of 0°, 15°, 30°, 45°, and -45° are presented in figure 11. The effect of sweepback on the lift-curve slope is shown in figure 12 and is compared with the theoretical variation computed by the method outlined in reference 3. The agreement between the experimental and theoretical results is very good at sweep angles up to 30°; however, at larger angles, the velocity-component concept apparently underestimates

the effects of sweep on the lift-curve slope. Better agreement at the higher sweeps would be attained if it is assumed that the leading edge is the correct reference in measuring the sweep angle, since the leading edge sloped at an angle of about 3° with reference to the quarter-chord line.

The effect of sweep on the spanwise load distribution of the wing is presented in figure 13 for sweep angles of 0°, 45°, and -45° at wing normal-force coefficients C_{N_W} of 0.20 and 0.40. The center of load shifted outward at sweepback because of the fact that the inboard vortices were more effective in producing upwash on the sections near the tip. This shift resulted in a decrease of induced angle of attack and, consequently, an increase of the effective angle of attack which caused an increase in the loading over the tip portion of the wing. At sweepforward the inboard vortices were less effective in producing upwash at the tip and resulted in a reduction of loading over the outboard portion of the wing.

The variation of lift coefficient with angle of attack for the wing-nacelle combination is given in figure 14 for Mach numbers of 0.20, 0.40, and 0.61 and sweep angles of 0°, 45°, and -45°. The slopes of these curves are compared with the slopes of the curves from the wing-alone data and are presented as a function of Mach number in figure 15. There was no change in the slope due to the presence of the nacelle on the unswept wing in the Mach number range investigated. At $\Lambda = 45°$ the presence of the nacelle increased the lift-curve slope by about 10 percent, whereas at $\Lambda = -45°$ the effect of the nacelle was to decrease the slope slightly. These changes resulted from a number of effects. The nacelle may be more or less effective as a lifting surface than the portion of the wing which is projected through the nacelle. The interference between the flow fields of the wing and the nacelle affects the lift. The change of the air-flow pattern over the wing which arises from sweep might be altered somewhat, especially when the nacelle protrudes ahead of the leading edge and above the upper surface of the wing. The distribution of downwash over the wing portions inboard and outboard of the nacelle may be influenced.

The slope of the lift curve was considerably less at 45° sweepforward than at 45° sweepback. At negative angles of sweep the location of the trailing vortices with respect to the flow field about the wing was such that the vortices were more effective in producing downwash than at positive angles of sweep. Consequently, a greater induced angle of attack and therefore a smaller effective angle of attack resulted.

A comparison of the lift characteristics through the stall of the wing alone and the wing-nacelle combination for sweep angles of 0°, 45°, and -45° at a Mach number of 0.13 is shown in figure 16. The presence of the nacelle on the unswept wing reduced the stalling angle from 22° to 14° and reduced the maximum lift coefficient from 1.36 to 1.06.

The nacelle, however, had no serious effect on the stalling characteristics for the swept configurations. At 45° sweepback the maximum lift coefficient obtained for both the wing alone and the wing-nacelle combination was about 1.10; whereas, at 45° sweepforward the maximum lift coefficient obtained was 0.97. At these swept configurations, for both the wing alone and the wing-nacelle combination, the progress of stall was gradual, and no sharp loss of lift was encountered up to about 32° angle of attack.

Drag.- The variation of drag coefficient with lift coefficient for the wing alone at sweep angles of 0°, 15°, 30°, 45°, and -45° is presented in figure 17 for Mach numbers from 0.20 up to the maximum tunnel Mach number (approx. 0.70). In general, the range of lift coefficients in which the drag coefficients remained lower for the swept wing than for the unswept wing increased with increasing Mach number. At lift coefficients below about 0.23, the drag coefficient of the 45° sweptforward wing was lower than for the 45° sweptback wing. At higher lift coefficients, the drag for 45° sweepforward increased more rapidly with increasing lift than for 45° sweepback. This difference of increase in drag with lift is associated with the lower lift-curve slope of the wing at sweepforward.

The drag coefficient was slightly higher for the 15° swept wing than for the unswept wing at all values of lift coefficient and Mach number. Apparently, the benefits due to sweep which tended to reduce the drag (for $\Lambda = 15°$) were smaller at finite values of lift coefficient than the adverse effects due to the smaller aspect ratio and lower lift-curve slope. The cause of the drag difference at and near zero lift is not apparent, but the difference is relatively small in magnitude.

In figure 18 the variation of drag coefficient with lift coefficient is presented for the wing-nacelle combination at sweep angles of 0°, 45°, and -45° and Mach numbers of 0.20, 0.40, and 0.61. A comparison of these drag coefficients with the drag of the wing alone for lift coefficients of 0, 0.20, and 0.40 is presented as a function of Mach number in figure 19. The increments of drag coefficient due to the nacelle at a lift coefficient of 0.20 over the Mach number range from 0.20 to 0.61 were approximately 0.0016, 0.0010, and 0.0012 for 0°, 45°, and -45° sweep, respectively. In order to compare the nacelle drag increment for the various sweeps and Mach numbers, the nacelle drag coefficient C_{D_N} (based on the maximum nacelle frontal area) is presented as a function of lift coefficient in figure 20. In general, the nacelle drag coefficient for the wing at 45° and -45° sweep was lower than for the unswept wing. This difference was probably due in part to the smaller wetted area of the nacelle in the swept positions.

One of the primary effects due to the presence of the nacelle on a wing is the fact that the nacelle represents a solid boundary which inhibits spanwise flow over the wing surfaces. In order to gain some indication of the effects of such a solid boundary on the drag of a swept wing, the variation of drag coefficient with lift coefficient is

presented in figure 21 for the wing at 45° sweepback with the curved and straight vanes installed. A somewhat lower drag resulted from the curved-vane configuration.

Pitching moment.- The variation of pitching-moment coefficient with lift coefficient for the wing alone at Mach numbers ranging from 0.20 to approximately 0.70 is given in figure 22 for sweep angles of 0°, 15°, 30°, 45°, and -45°. The pitching-moment data for the wing-nacelle combination are shown in figure 23 for sweep angles of 0°, 45°, and -45° and Mach numbers of 0.20, 0.40, and 0.61. The effect of nacelle and sweep on the slope of the pitching-moment curve is presented in figure 24 at a Mach number of 0.61. The effect of the nacelle was to reduce the stability slightly at all angles of sweep. Sweeping the wing in the positive direction resulted in a marked increase of stability which was caused by the outward shift in the center of load as was shown in figure 13. At -45° sweep the stability was increased due to the inward shift of the center of load.

Pressure Distributions

Pressure distributions of the wing-nacelle inboard and outboard junctures are presented in figures 25 to 27 for sweep angles of 0°, 45°, and -45° at lift coefficients of 0.20 and 0.40 and Mach number of approximately 0.60. No adverse pressure peaks were present on the unswept configuration. At $\Lambda = 45°$, high negative pressure peaks and adverse pressure gradients existed near the leading edge at the inboard juncture, whereas at the negative sweep position the same flow characteristics resulted at the outboard juncture near the leading edge of the wing. The critical Mach number was surpassed for the sweptback position at lift coefficients of both 0.20 and 0.40 and for the sweptforward position at a lift coefficient of 0.40. Despite these supercritical pressure peaks, the nacelle drag for the swept configurations based on nacelle frontal area was lower than for the unswept configuration as is shown in figure 20. Apparently the pressure peaks caused by wing-nacelle interference were too localized in the Mach number range investigated to influence the over-all drag materially. At higher Mach numbers, however, the adverse pressure peaks at these configurations would undoubtedly be extended sufficiently to increase the over-all drag. Tests of a high-aspect-ratio swept wing in combination with a fuselage conducted in the Langley 8-foot high-speed tunnel show that a severe drag rise occurs at the acute juncture in a Mach number range above that of the present investigation. The swept wing-nacelle interference which causes such a drag rise may be reduced by proper juncture modifications, the nature of which would require a detailed study. The data in reference 1 indicate that a modification in the contour of the nacelle portion which protrudes ahead of the wing leading edge to conform with the flow pattern immediately ahead of a swept wing is effective in reducing the pressure peaks at the juncture.

Figures 28 to 30 show pressure distributions on the upper and lower surfaces in the vertical plane of symmetry of the nacelle for sweep angles of 0°, 45°, and -45° at a Mach number of about 0.60 and lift coefficients of 0.20 and 0.40. For the swept configurations the pressure gradients behind the maximum negative pressures were more gradual than for the unswept configuration. In addition, the effect of the sweep was to move the center of pressure forward on the nacelle. No extreme pressure peaks occurred over this portion of the nacelle for any of the test conditions.

Pressure contours for the upper and lower surfaces of the wing alone are presented in figures 31 to 42. As would be expected from the theory of sweep, the negative pressures on both the upper and lower surfaces were reduced as the sweep was increased. Figures 31 to 33 show the effects of sweep on the location of the peak pressures for a lift coefficient of 0.20 and a Mach number of 0.61. At zero sweep, the peak pressures on the upper surface occurred at about the 35-percent-chord station over the entire span of the wing. For the wing at 45°, the peaks toward the inboard portion of the wing remained at about the 35-percent-chord station, whereas near the tip they shifted forward to the leading edge. At $\Lambda = -45°$ the peaks along the span occurred at the leading edge except for those near the tip which were shifted slightly rearward. The effects of sweep on the spanwise distribution of peak pressures are also evident in figures 31 to 33. The peaks shifted outward for positive sweep and inward for negative sweep. This effect is consistent with the spanwise-loading curves presented in figure 13. It is apparent from figures 32 and 33 that the spanwise pressure gradient at sweepforward was greater than at sweepback; and since the peak pressures occurred farther forward on the wing at sweepforward, the gradient effected a spanwise flow over a greater portion of the wing.

Figures 34 and 35 present pressure contours on the wing at a lift coefficient of 0.20 and a Mach number of 0.61 for sweep angles of 15° and 30°, respectively. These figures show that the peak pressures on the upper surface were shifted progressively outboard as the sweep angle was increased. In addition, increasing the sweep reduced the magnitude of the pressures on both the upper and lower surfaces.

A comparison of figures 31 and 34 shows that the spanwise pressure gradient along the trailing edge for the 0° and 15° sweep positions were of approximately the same magnitude but opposite in slope. This fact indicates that the spanwise flow in the boundary layer should be of about the same magnitude.

Pressure contours for the wing at $\Lambda = 0°$, 45°, and -45° for a lift coefficient of 0.20 and a Mach number of 0.20 are presented in figures 36 to 38. A comparison of these pressures with those of figures 31 to 33 indicates that a change in Mach number from 0.20 to 0.61 had no appreciable effect on the pressure contours.

The contours of figures 39 and 40 are shown with the wing at 45° sweepback for a lift coefficient of zero and Mach numbers of 0.20 and 0.61, respectively. The upper surface peaks across the span occurred between the 45- and 50-percent-chord stations at both Mach numbers. Increasing the lift coefficient to 0.40 shifted the peak pressures on the upper surface to the leading edge of the wing (figs. 41 and 42).

Figures 43 to 52 show the pressure contours for the wing-nacelle combination. These data are presented for the same lift coefficients, Mach numbers, and sweep angles as are given for the wing alone in figures 31 to 33 and 36 to 42. As was previously shown in figures 26 and 27, high localized pressure peaks existed at the leading edges of the wing-nacelle inboard juncture of the sweptback wing and the wing-nacelle outboard juncture of the sweptforward wing. In general, the lines of constant pressure on both the upper and lower surfaces at these junctures were so altered because of the wing-nacelle interference that they became normal to the air stream. This fact indicates that in the vicinity of the juncture where the critical pressures were exceeded the resulting shock also occurred in a direction normal to the air stream; therefore, the loss through the shock was greater than would have been experienced had the shock been oblique to the oncoming flow.

The pressure contours on the 45° sweptback wing with vertical plates installed, for a lift coefficient of 0.40 and a Mach number of 0.20, are presented in figure 53. Apparently the plates were somewhat effective in reducing the extreme localized pressure peaks at the leading edge near the tip, but they did not alter the pressure pattern on the trailing portion of the wing.

Visual Observation of Flow Characteristics

The flow patterns in the boundary layer on the wing alone and the wing-nacelle combination for sweep angles of 0°, 45°, and -45° at various angles of attack and Mach numbers are presented in figures 54 to 57. These patterns were interpreted from tuft studies of the flow over the model. With the wing at $\Lambda = 0°$ and $\Lambda = 45°$ and angles of attack for a lift coefficient of 0.40, the addition of the nacelle caused a slight deviation of the flow in the immediate vicinity of the nacelle only (figs. 54 and 55). Figure 56 shows that, at the same lift coefficient, the addition of the nacelle to the sweptforward wing resulted in no detectable deviation in the flow. In addition, figures 55 and 56 indicate that neither the distortion of the air stream due to the velocity components which result from sweep nor the spanwise flow near the trailing edge was altered by the presence of the nacelle.

Comparisons of the flow patterns over the wing and the wing-nacelle combinations are presented in figure 57 at geometric angles of attack of 18°, 22°, and 20° for sweep angles of 0°, 45°, and -45°, respectively. At $\Lambda = 0°$ the addition of the nacelle appreciably increased the area over which unsteady flow occurred, which indicates that a substantial loss of lift resulted. The patterns for the swept configurations show that the presence of the nacelle had very little influence on the flow characteristics over the wing and did not appreciably increase the area of unsteady flow. The results shown by these patterns serve to supplement the lift data of figure 16.

The flow pattern over the wing at 45° sweepback and at a geometric angle of attack of 6° with the vertical plates mounted on the upper surface is presented in figure 58. This pattern shows that the plates were relatively ineffective in reducing the boundary-layer spanwise flow over the trailing portion of the wing. Visual observations of tufts mounted on the surfaces of the plates indicated that the air flowed upward on the inboard surfaces of the plates and downward on the surfaces facing outboard.

Figure 59 presents the flow patterns over the wing at $\Lambda = 45°$ with the straight and curved vanes installed. The distortion of flow due to sweepback was reduced immediately outboard of the straight vane, whereas the curved vane had no noticeable influence on the pattern of flow.

CONCLUSIONS

The results of an investigation to determine the effects of a nacelle on the aerodynamic chracteristics of a swept wing and the results of the effects of sweep on the aerodynamic characteristics of the wing alone led to the following conclusions:

1. The experimental variation of wing lift-curve slope with sweep angle is in good agreement with the theoretical variation up to 30° sweep. At greater sweeps, however, the velocity-component concept apparently underestimates the effects of sweep on the lift-curve slope.

2. The presence of the nacelle increased the lift-curve slope of the 45° sweptback wing by about 10 percent, whereas the nacelle slightly decreased the lift-curve slope of the 45° sweptforward wing. The nacelle did not affect the lift-curve slope of the unswept wing.

3. The presence of the nacelle did not appreciably alter the lift and stalling characteristics of the wing at sweep angles of 45° or -45°, but for the unswept wing the addition of the nacelle caused an appreciable reduction of the maximum lift coefficient and of the angle of attack for maximum lift. At 45° or -45° sweep the progress of stall was gradual and no sharp loss of lift was encountered up to an angle of attack of about 32°.

4. In general, for Mach numbers up to 0.61 the drag increment due to the nacelle was lower for the swept configurations than for the unswept configurations. At a lift coefficient of 0.20 and Mach numbers ranging from 0.20 to 0.61, the drag increments were approximately 0.0016, 0.0010, and 0.0012 for 0°, 45°, and -45° sweep, respectively.

5. The presence of the nacelle reduced the longitudinal stability of the wing slightly at all sweep angles. For both the wing alone and the wing-nacelle combination, a marked increase in longitudinal stability resulted from positive sweep, whereas only a small increase was realized for negative sweep (-45°).

6. When the wing was swept back or swept forward to an angle of 45°, high pressure peaks and adverse pressure gradients occurred near the leading edge of the wing at the acute junction of the wing and nacelle.

Langley Aeronautical Laboratory
National Advisory Committee for Aeronautics
Langley Field, Va., June 8, 1948

REFERENCES

1. Buschner, R.: Der Anbau von TL-Triebwerken an den Tragflügel. 4. Teilbericht: Druckverteilungs-messungen an einem Pfeilflügel mit einem Triebwerk. UM Nr. 3176, Deutsche Luftfahrtforschung (Göttingen), 1944.

2. Anon: Determination of Center of Gravity and Mean Aerodynamic Chord ACTR No. 2790, Material Div., Army Air Corps, Aug. 1, 1929.

3. Letko, William, and Goodman, Alex: Preliminary Wind-Tunnel Investigation at Low Speeds of Stability and Control Characteristics of Sweptback Wings. NACA TN No. 1046, 1946.

4. Sivells, James C., and Deters, Owen J.: Jet-Boundary and Plan-Form Corrections for Partial-Span Models with Reflection Plane, End Plate, or No End Plate in a Closed Circular Wind Tunnel. NACA TN No. 1077, 1946.

TABLE I

WING PRESSURE ORIFICE LOCATIONS

Spanwise locations		Chordwise locations, x/c (a)	
Distance along quarter-chord line from tunnel wall (in.)		Upper surface	Lower surface
$\Lambda = 0^\circ$	$\Lambda = 30^\circ$	0	0
15.00	22.70	.004	.004
30.00	37.70	.008	.008
45.00	52.70	.011	.010
52.25	59.95	.015	.025
67.75	75.45	.025	.050
75.00	82.70	.050	.100
90.00	97.70	.075	.200
104.00	111.70	.100	.250
$\Lambda = 15^\circ$	$\Lambda = 45^\circ$	.150	.350
18.55	28.45	.250	.450
33.55	43.45	.350	.550
48.55	58.45	.450	.650
55.80	65.70	.550	.750
71.30	81.20	.650	.850
78.55	88.45	.750	.950
93.55	103.45	.850	-----
107.55	117.45	.950	-----
$\Lambda = -45^\circ$			
1.75			
16.75			
31.75			
39.00			
54.50			
61.75			
76.75			
90.75			

[a] Measured for all sweep angles.

NACA

TABLE II

GENERAL DIMENSIONS OF THE NACA 65_2-215 WING

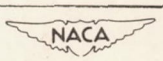
Λ (deg)	b/2 (ft)	A	c_r (ft)	c_t (ft)	$\bar{c}$ (ft)	c_r' (ft)	c_t' (ft)	S_w (sq ft)	b'/2 (ft)	$\bar{c}_\Lambda$ (ft)
0	10.00	6.00	4.44	2.22	3.46	4.44	2.22	33.33	10.00	3.33
15	9.81	5.76	4.54	2.27	3.53	4.51	2.25	33.38	10.15	3.38
30	8.96	4.78	4.99	2.49	3.88	4.59	2.29	33.50	10.32	3.44
45	7.51	3.32	6.02	2.99	4.68	4.69	2.33	33.85	10.64	3.51
-45	6.72	2.66	6.75	3.35	5.24	4.18	2.09	33.94	9.51	3.13

NACA

TABLE III

NACELLE COORDINATES

Distance along longitudinal axis of nacelle (in.)	Radius of nacelle (in.)
0	0
1.062	1.345
2.123	2.031
4.246	3.050
6.369	3.793
8.492	4.387
12.738	5.251
16.984	5.886
21.230	6.355
25.476	6.709
29.722	6.950
33.967	7.077
38.213	7.077
42.459	6.978
46.705	6.737
50.951	6.355
55.197	5.803
59.443	5.123
63.689	4.331
67.935	3.474
72.181	2.625
76.427	1.762
80.673	.877
82.799	.441
84.919	0



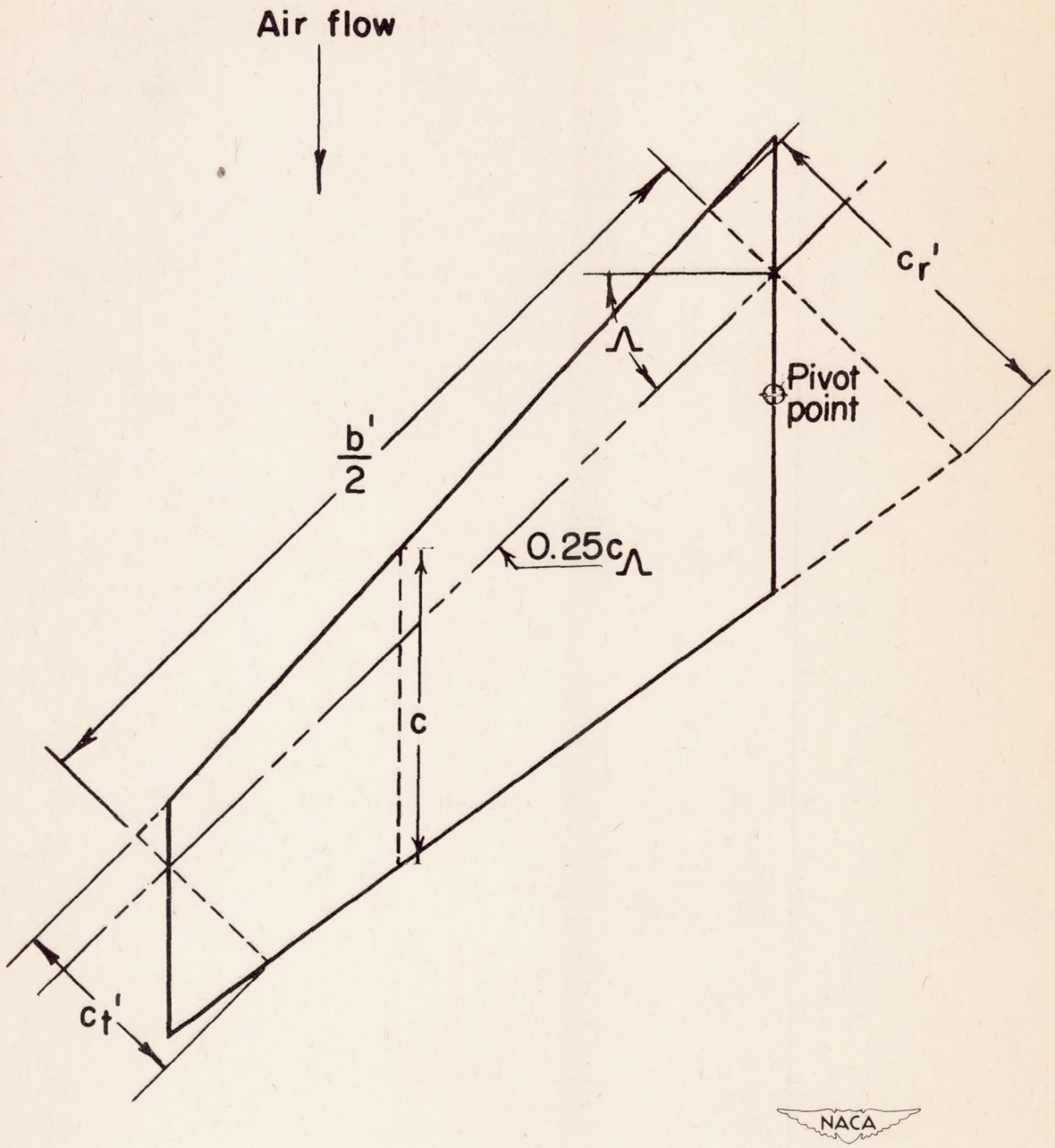
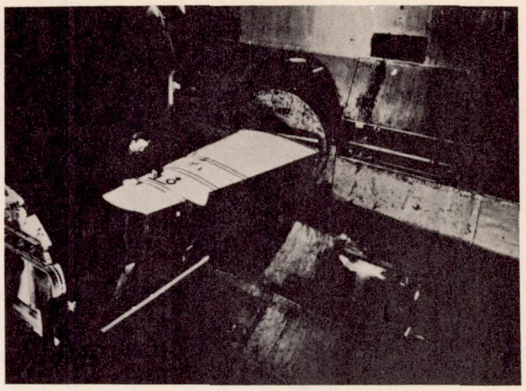
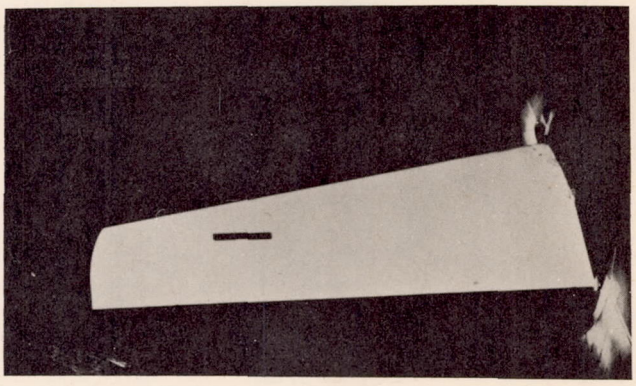


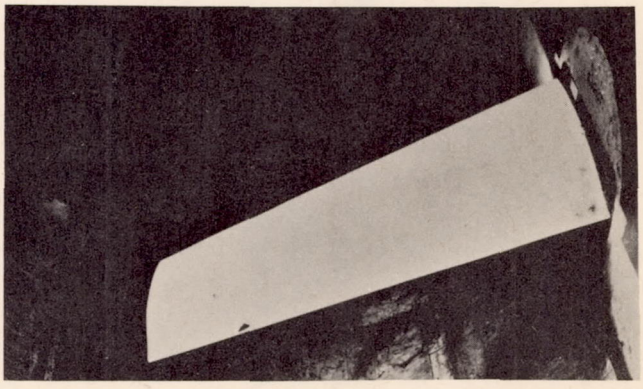
Figure 1.— Chords and spans on swept wing.
Wing shown at $\Lambda = 45°$.



(a) $\Lambda = 0^{\circ}$.



(b) $\Lambda = 15^{\circ}$.

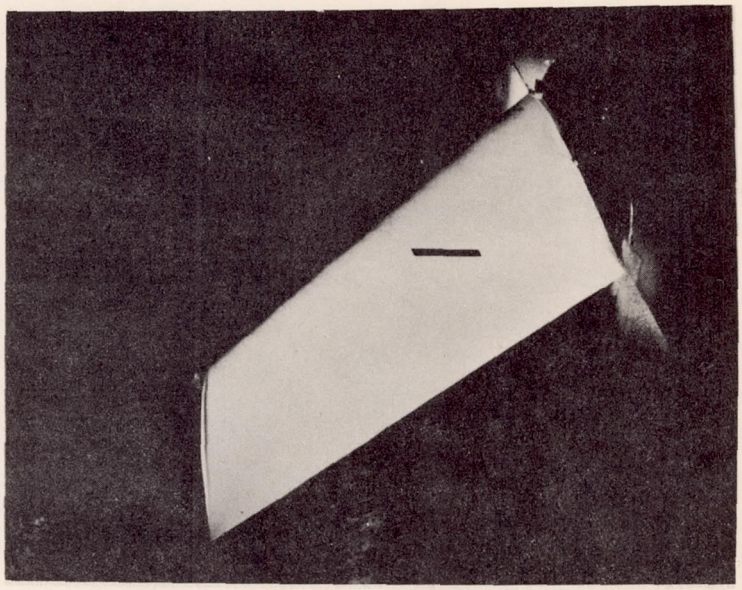


(c) $\Lambda = 30^{\circ}$.

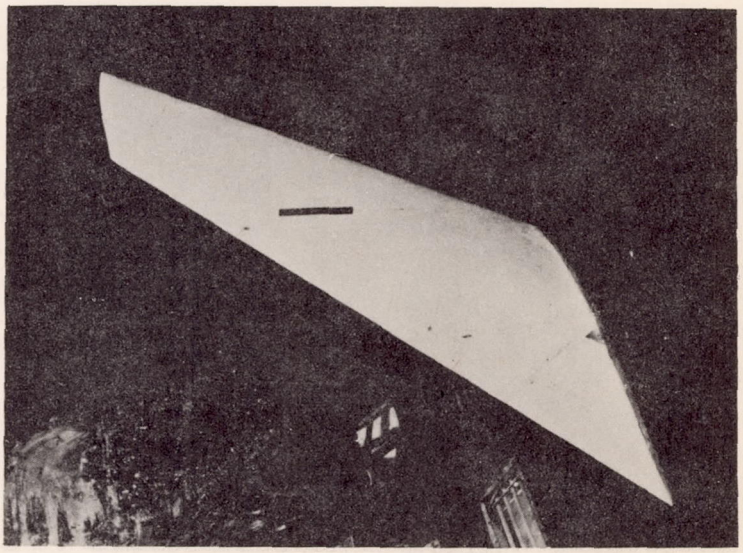
Figure 2.- Wing mounted in Langley 16-foot high-speed tunnel.

NACA

L-56603



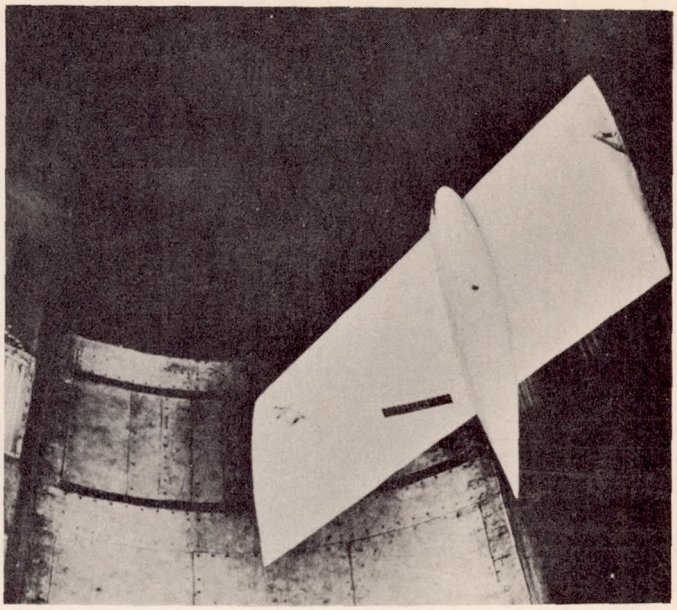
(d) $\Lambda = 45^{\circ}$.



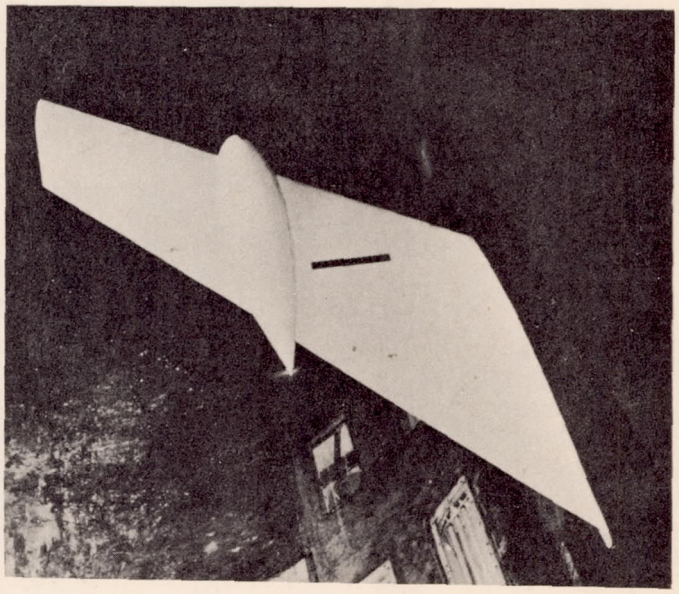
(e) $\Lambda = -45^{\circ}$.

Figure 2.- Concluded.

NACA L-56604



(a) $\Lambda = 45^{\circ}$.



(b) $\Lambda = -45^{\circ}$.

Figure 3.- Wing-nacelle combination mounted in Langley 16-foot high-speed tunnel.

L-56605

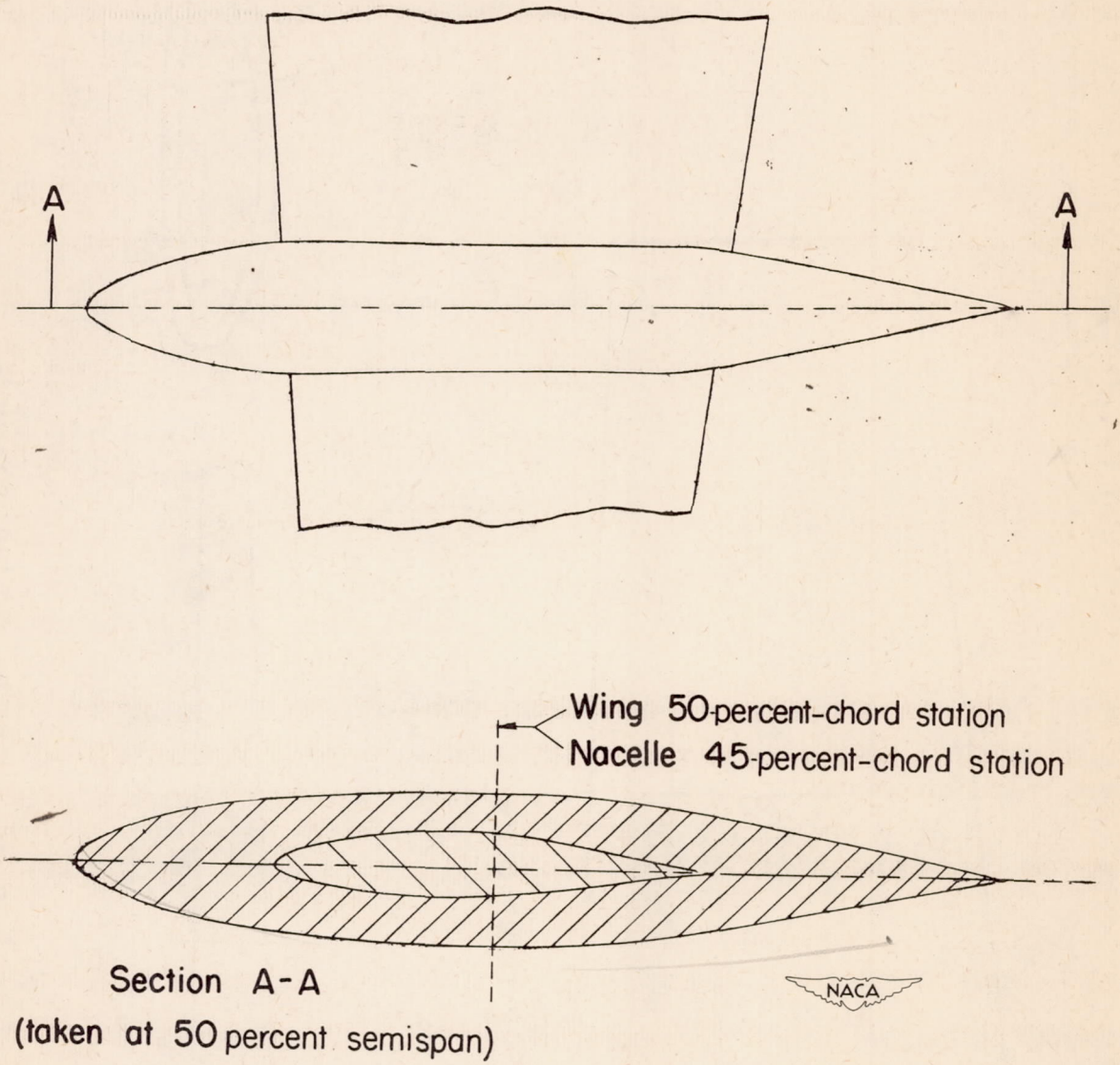


Figure 4 .—— Location of nacelle on wing at $\Lambda = 0°$.

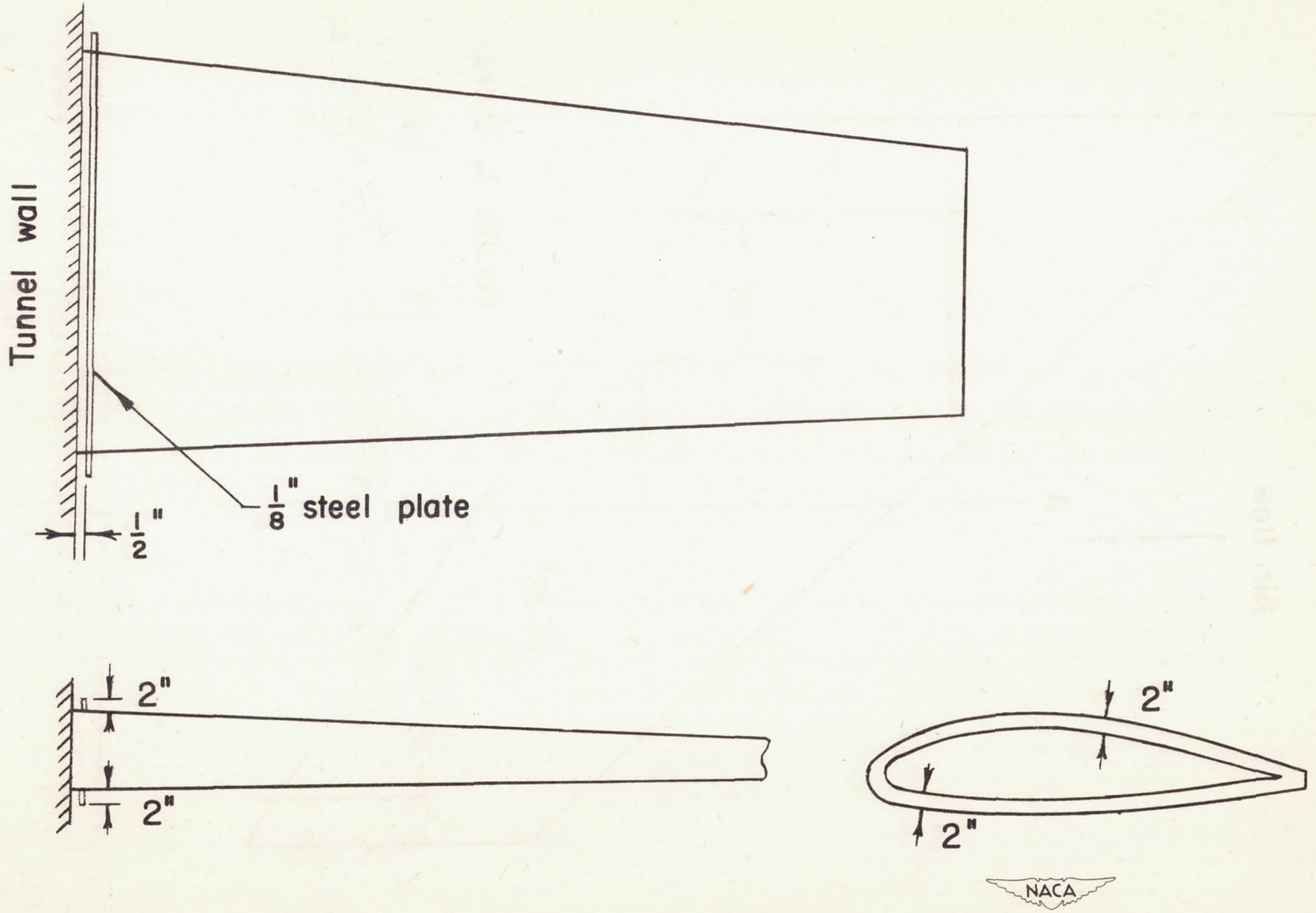


Figure 5.—Location of leakage deflection plates.

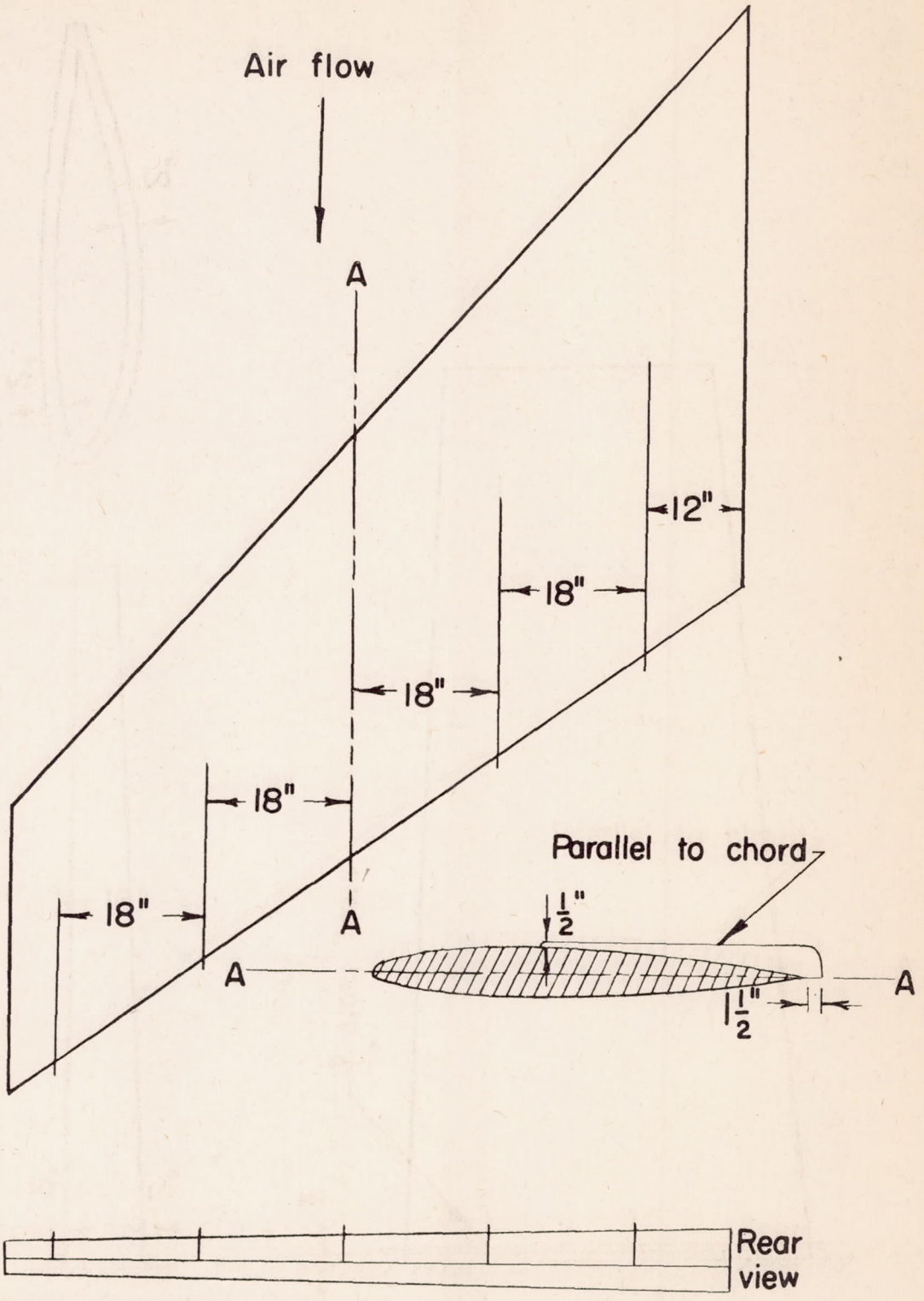


Figure 6.— Wing at 45° sweepback with vertical plates installed on upper surface.

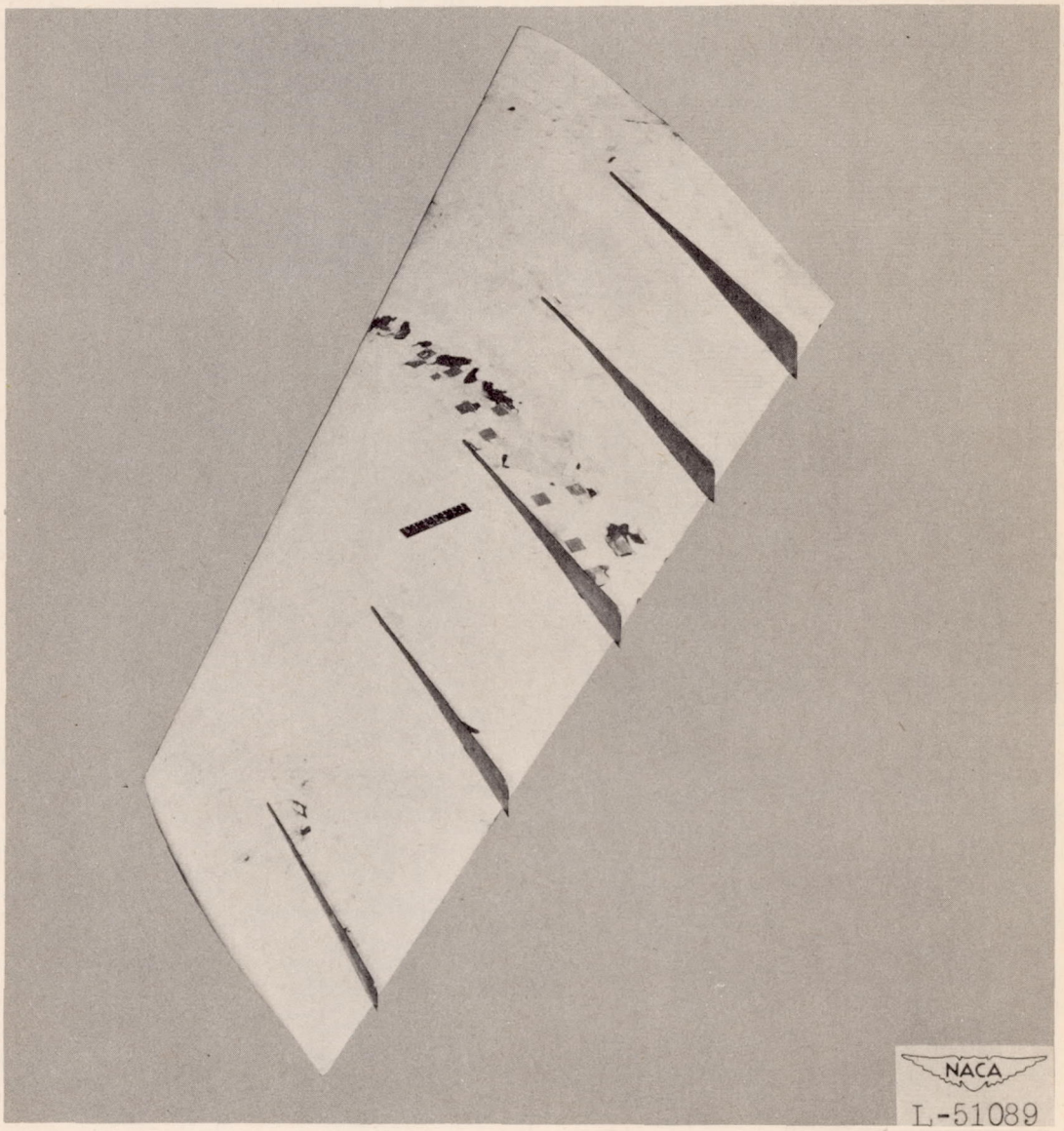


Figure 7.- Wing at 45° sweepback with vertical plates installed on upper surface.

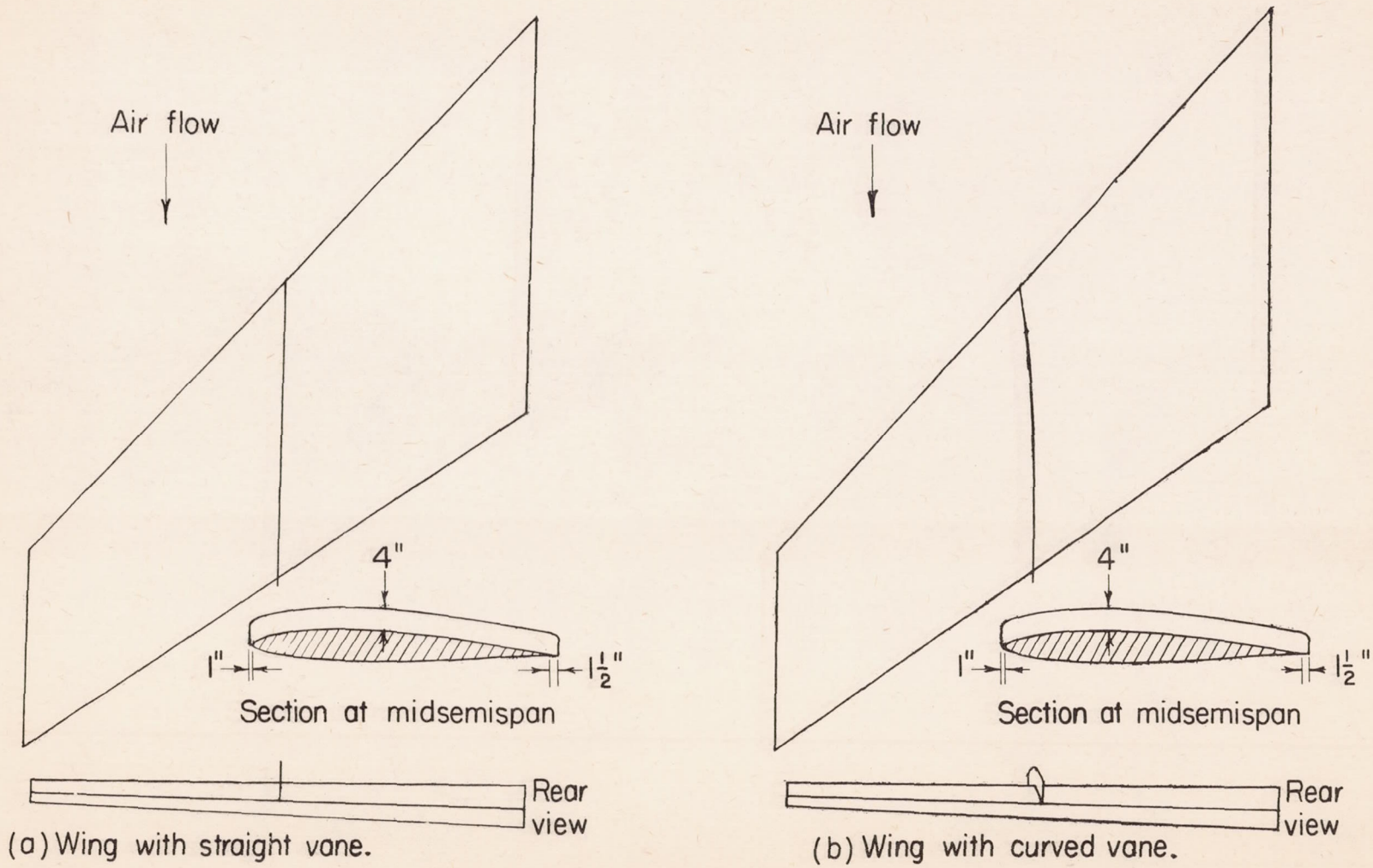
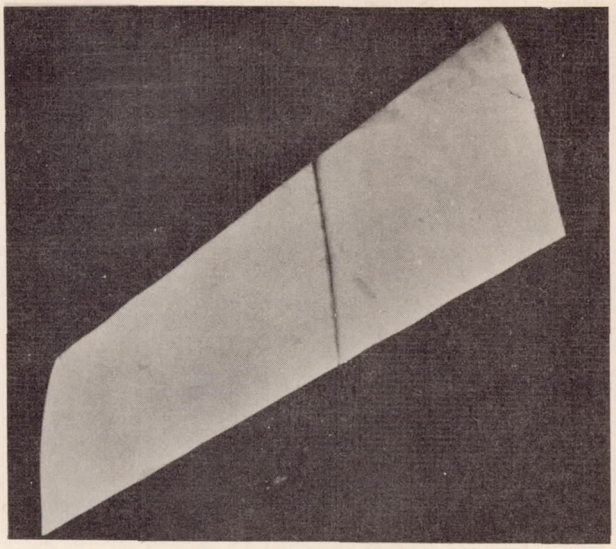
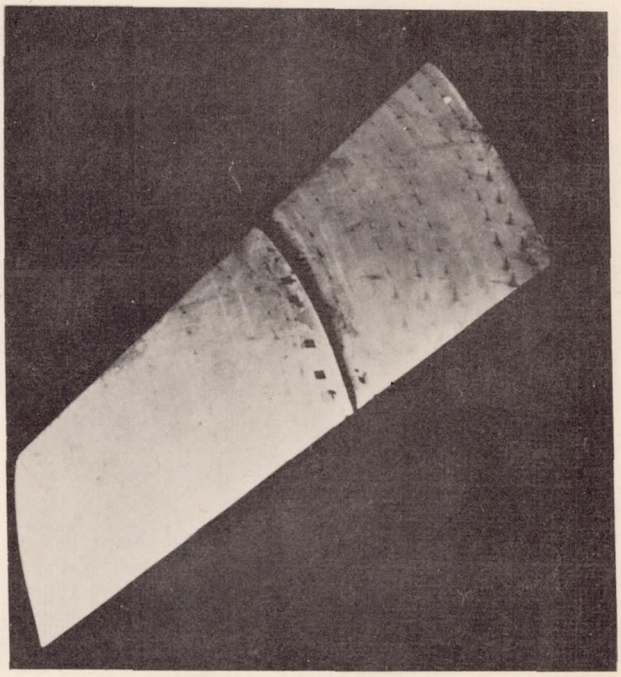


Figure 8.— Wing at 45° sweepback with straight and curved vanes mounted at midsemispan.



(a) Wing with straight vane.



(b) Wing with curved vane.

Figure 9.- Wing at 45° sweepback with straight and curved vanes installed.

NACA
L-56606

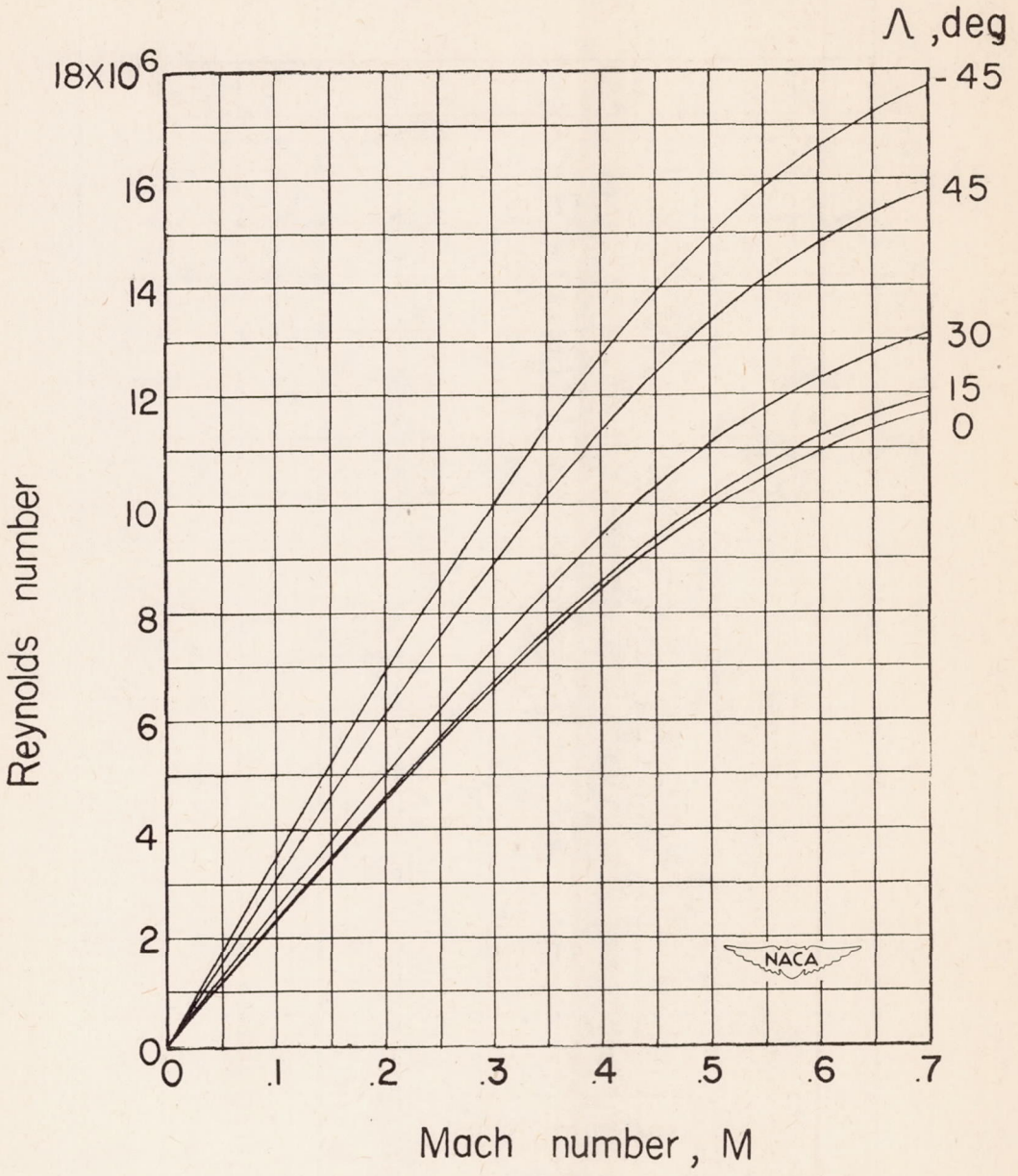
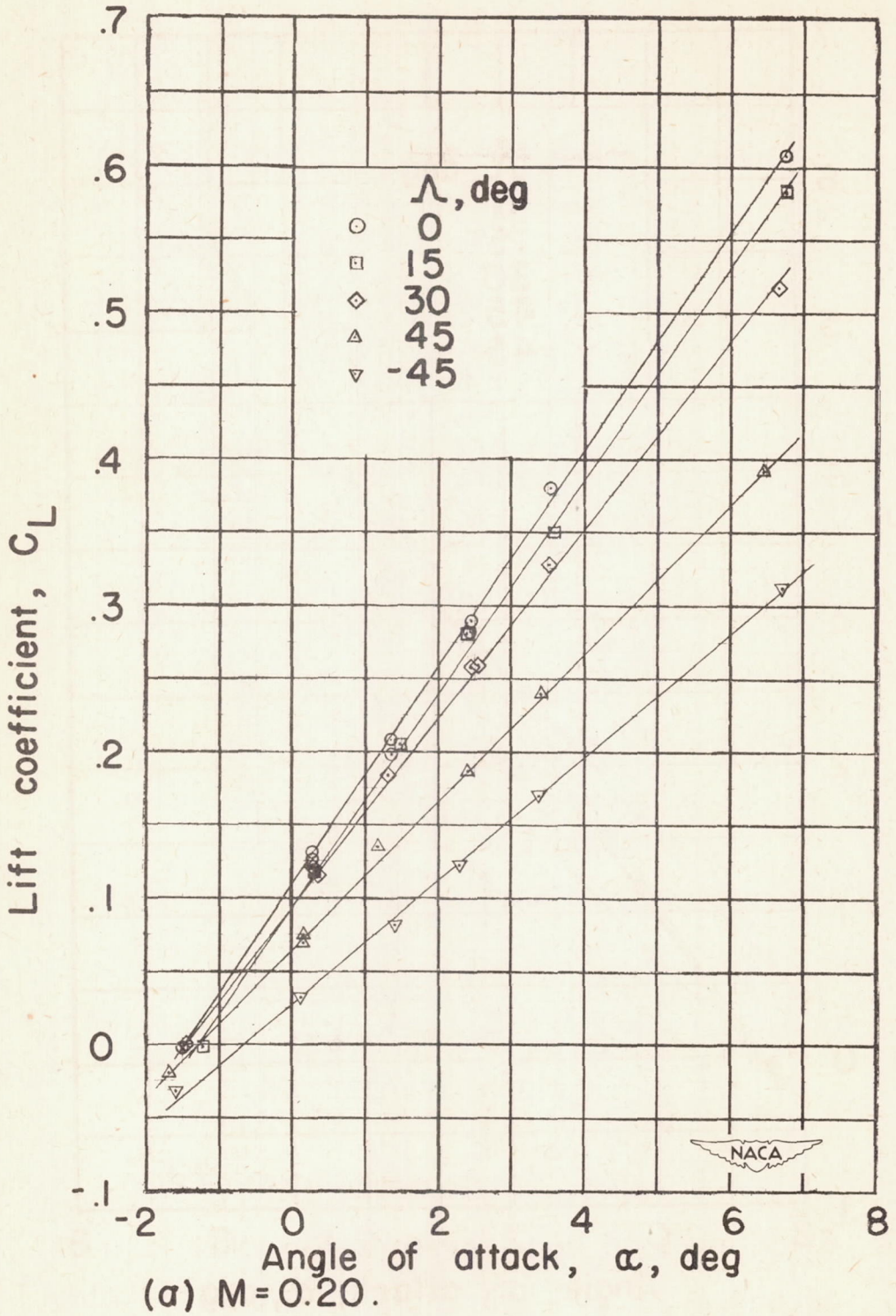
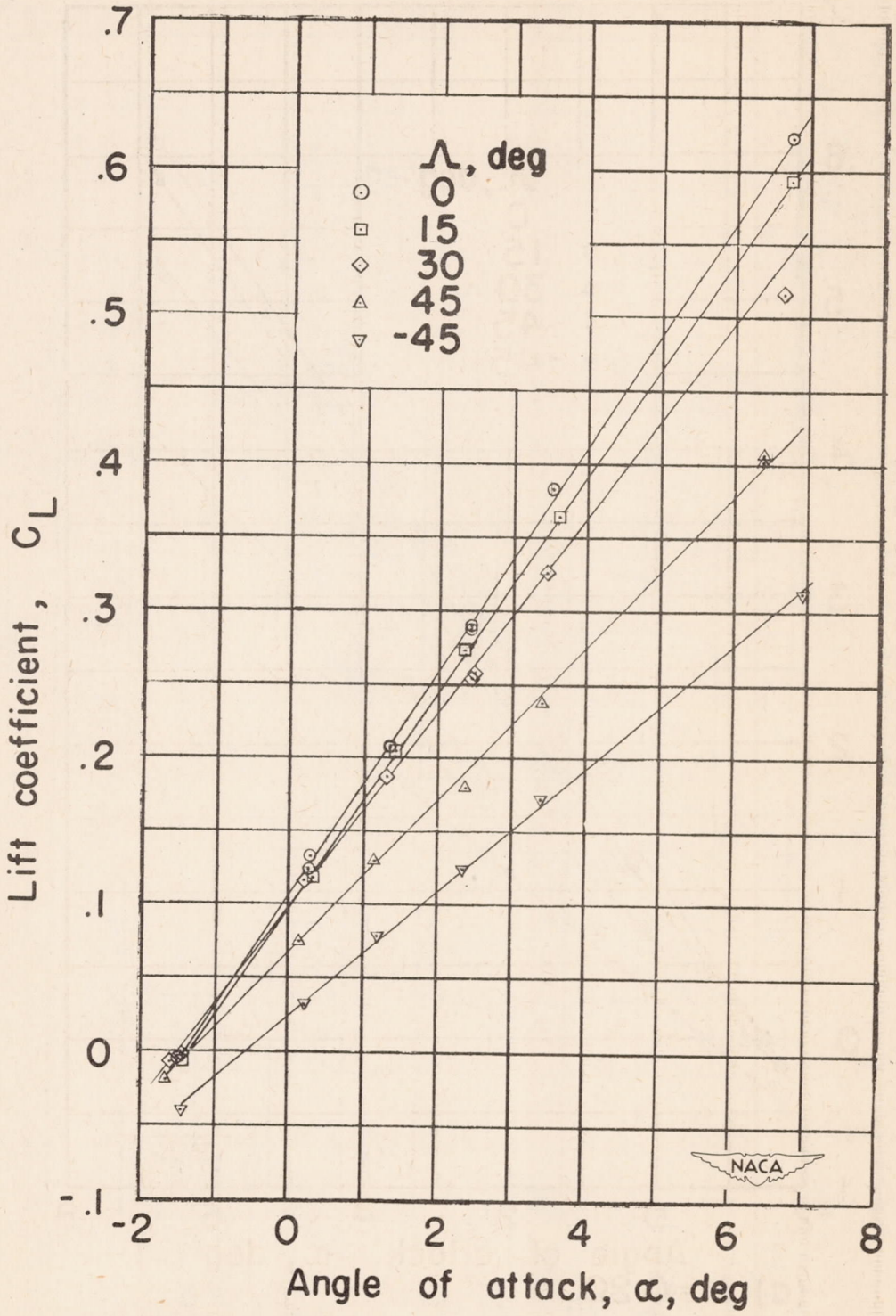


Figure 10.— Variation of Reynolds number with Mach number and sweep. (Reynolds number is based on average chord in stream direction.)



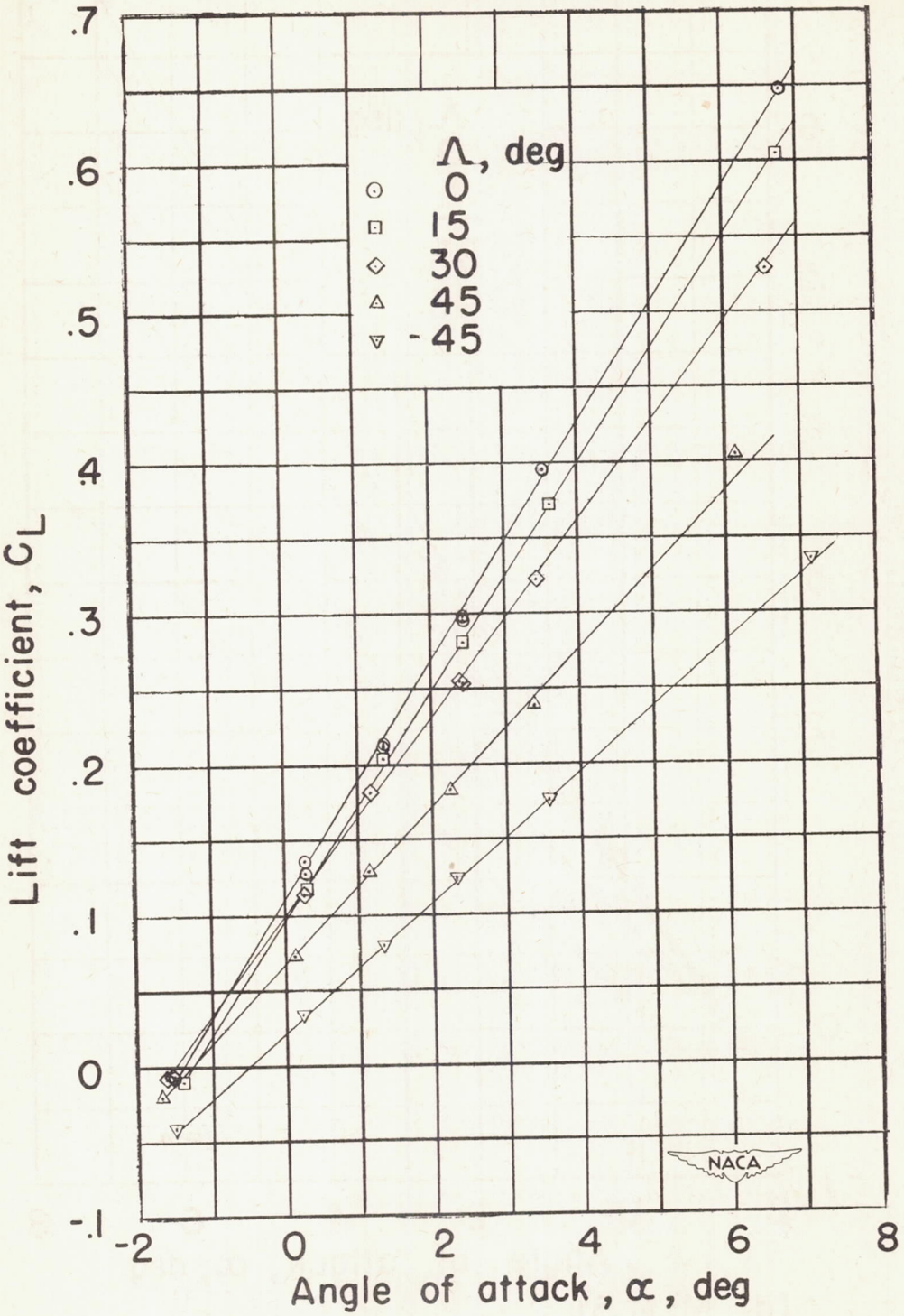
(a) M = 0.20.

Figure 11.— Variation of lift coefficient with angle of attack for wing alone.



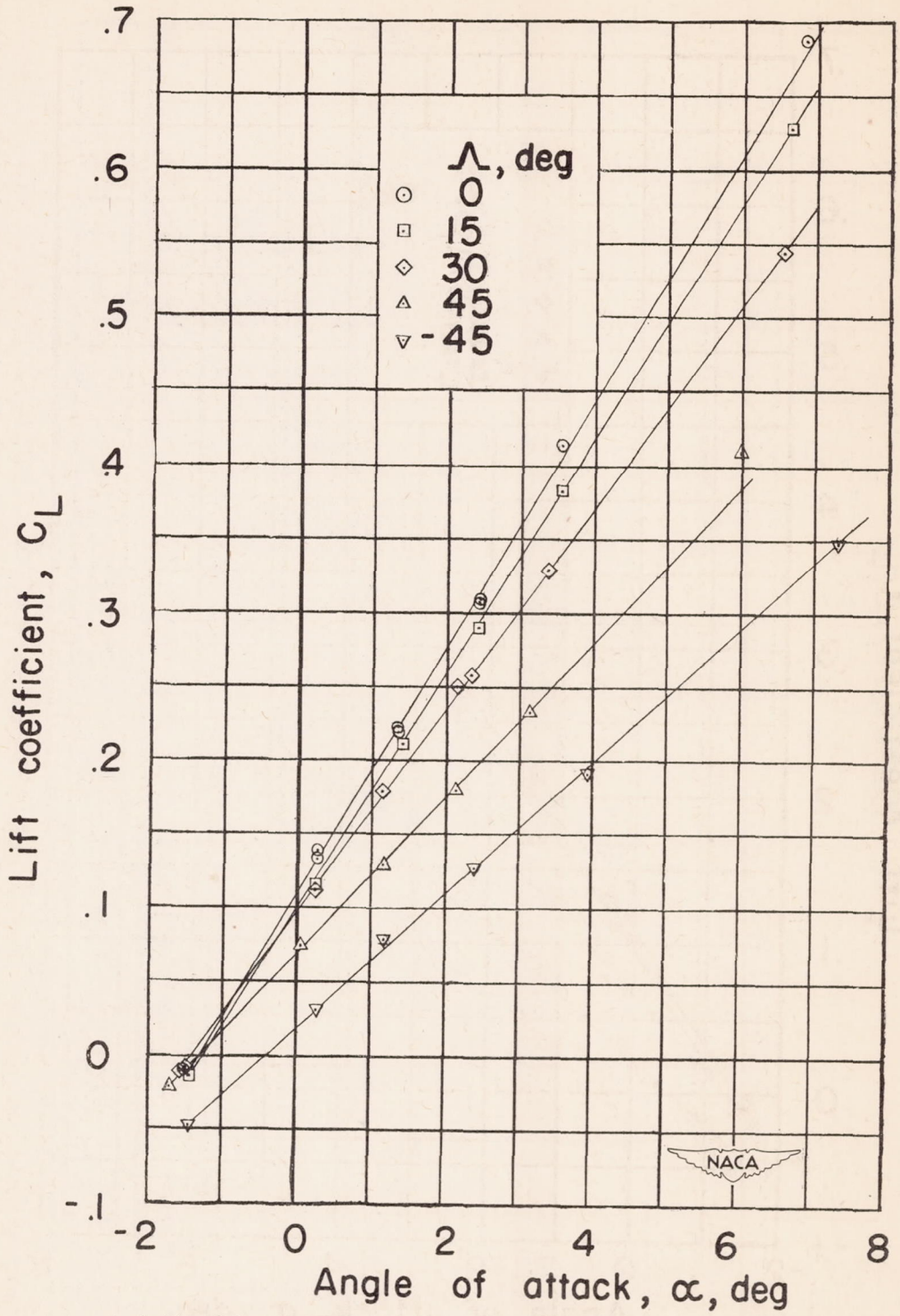
(b) M = 0.30.

Figure 11.— Continued.



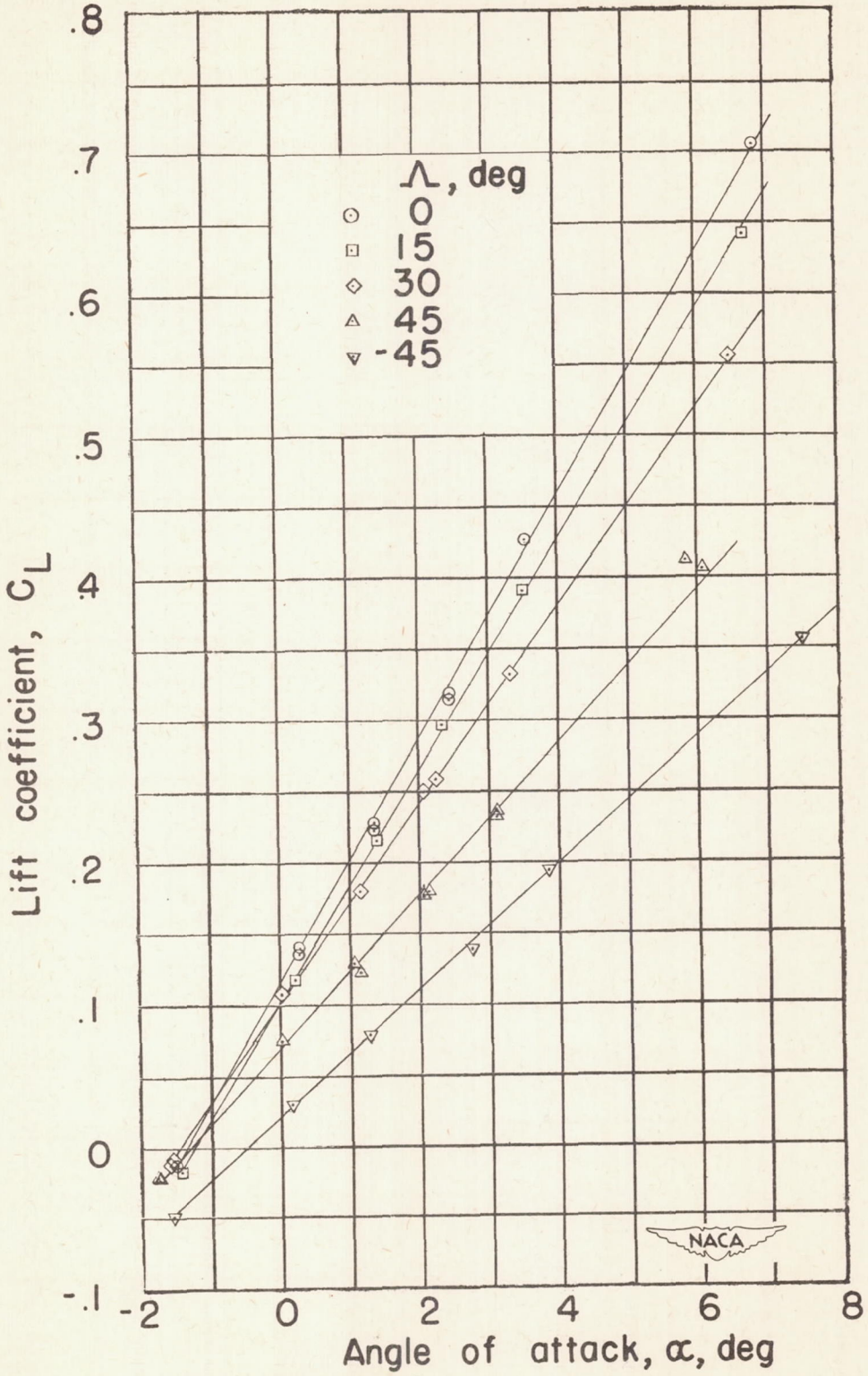
(c) M = 0.40.

Figure 11.— Continued.



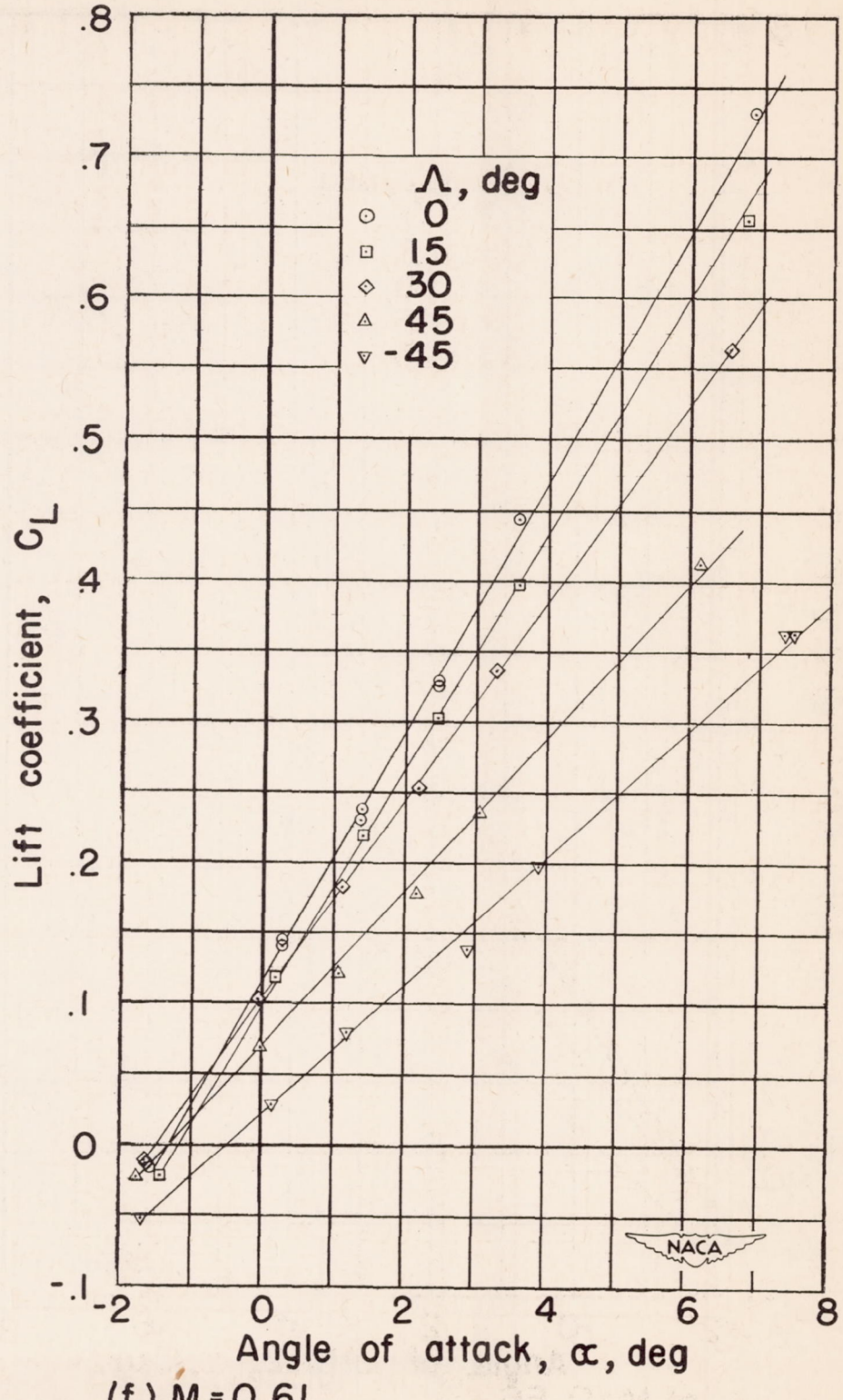
(d) M=0.51.

Figure 11.— Continued.



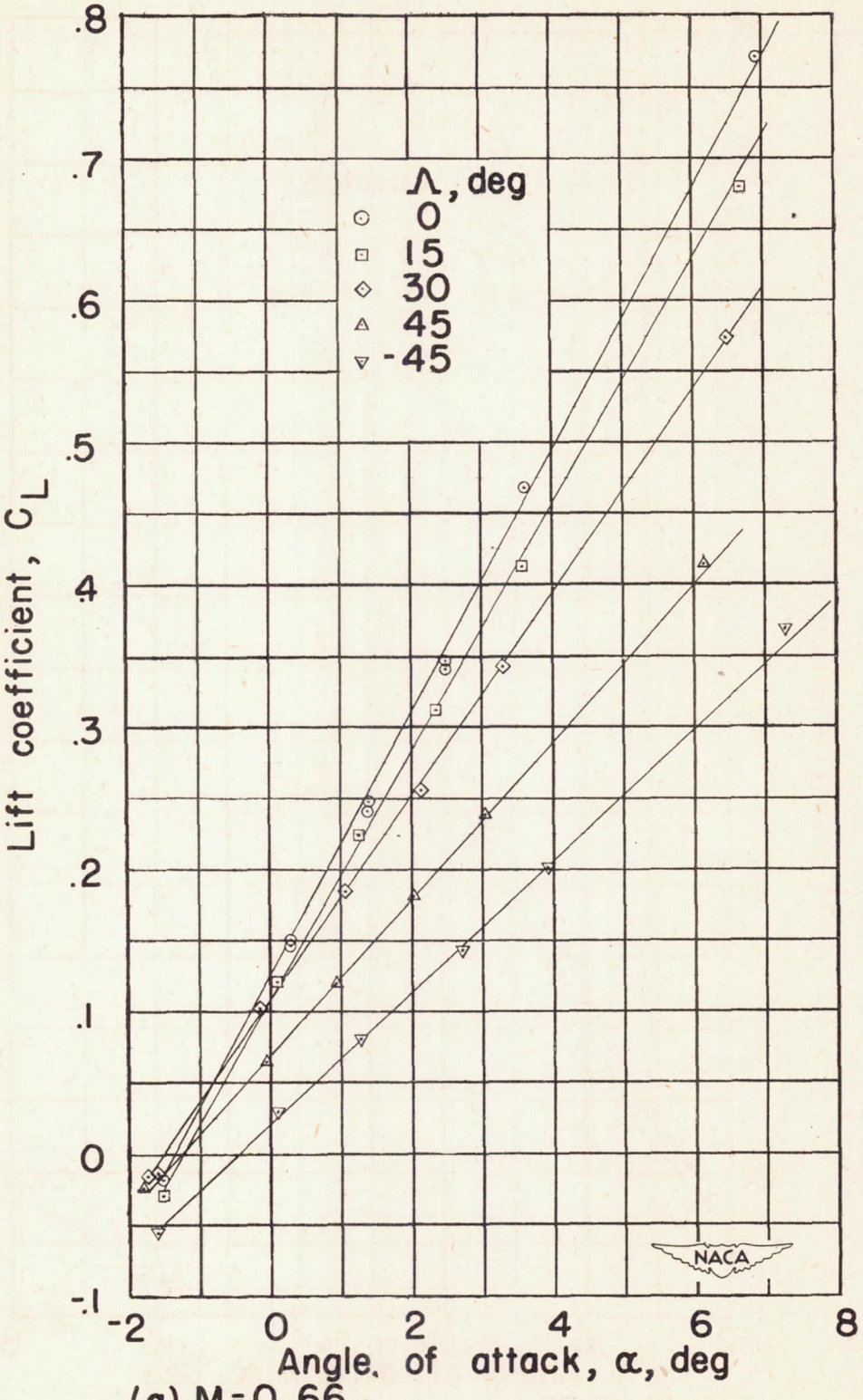
(e) M=0.56.

Figure 11.— Continued.



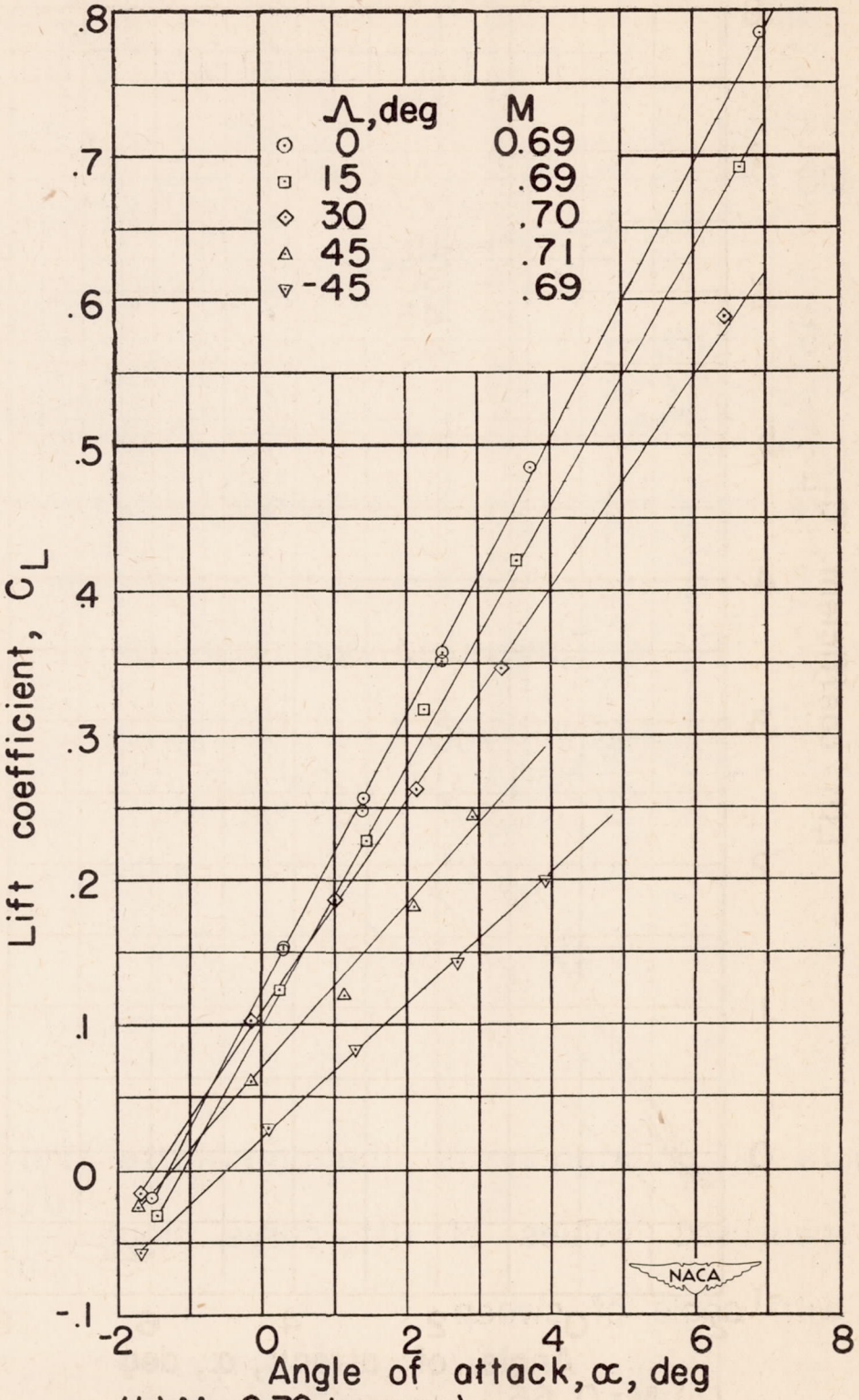
(f) M = 0.61.

Figure 11.— Continued.



(g) M=0.66.

Figure 11.— Continued.



(h) M = 0.70 (approx.).

Figure 11.— Concluded.

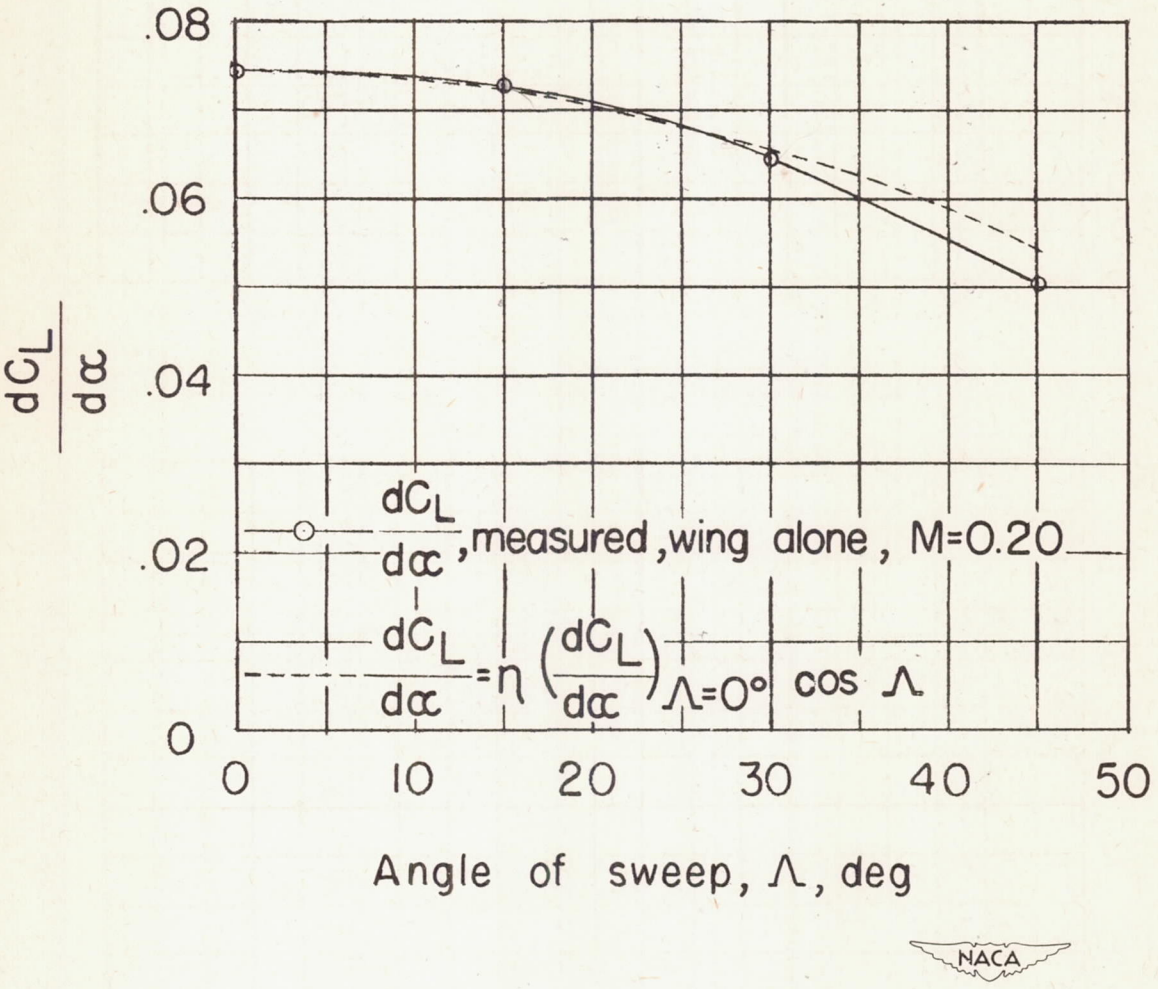


Figure 12.— Variation of the calculated and measured values of lift-curve slope $\frac{dC_L}{d\alpha}$ with angle of sweep.

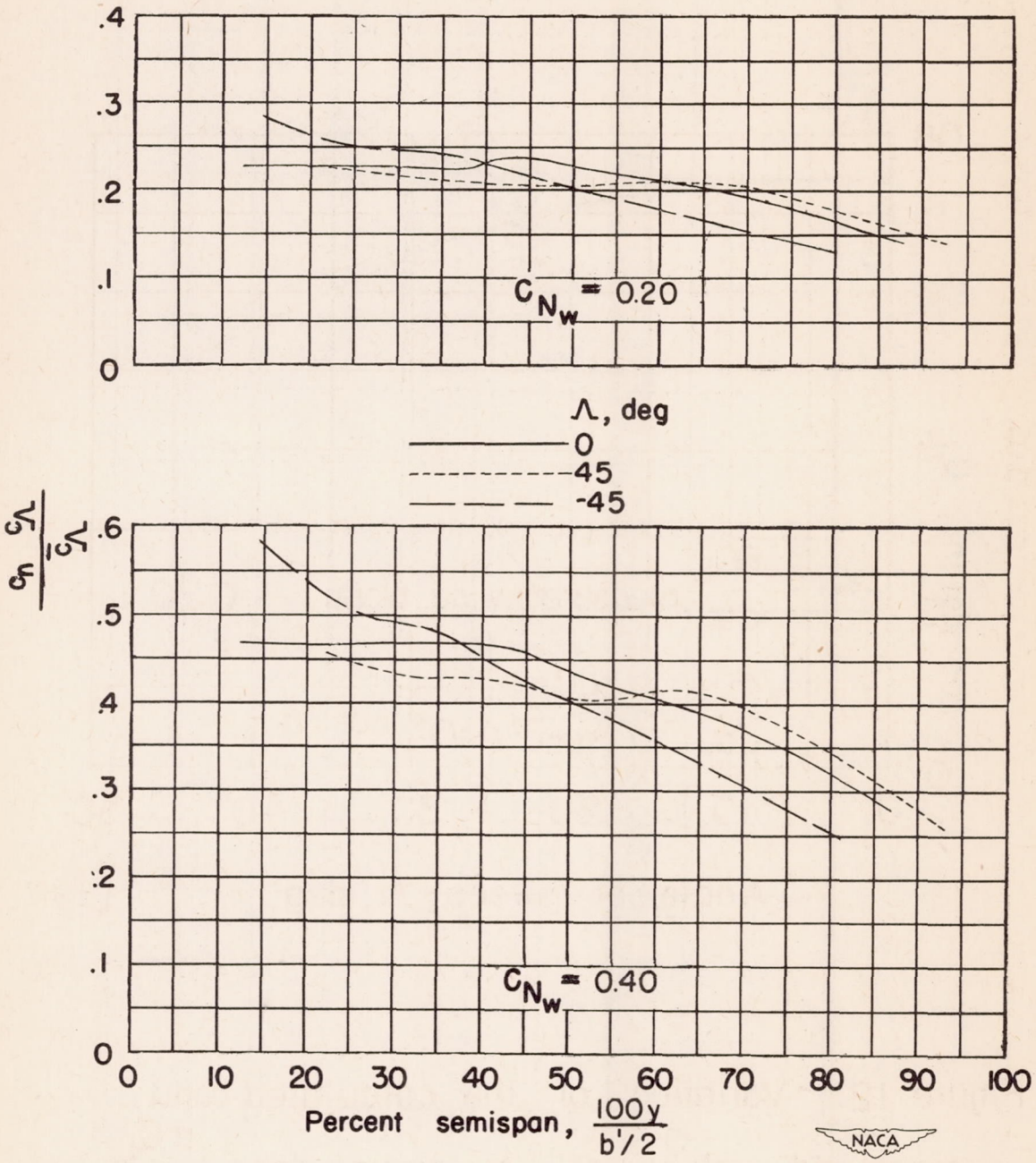
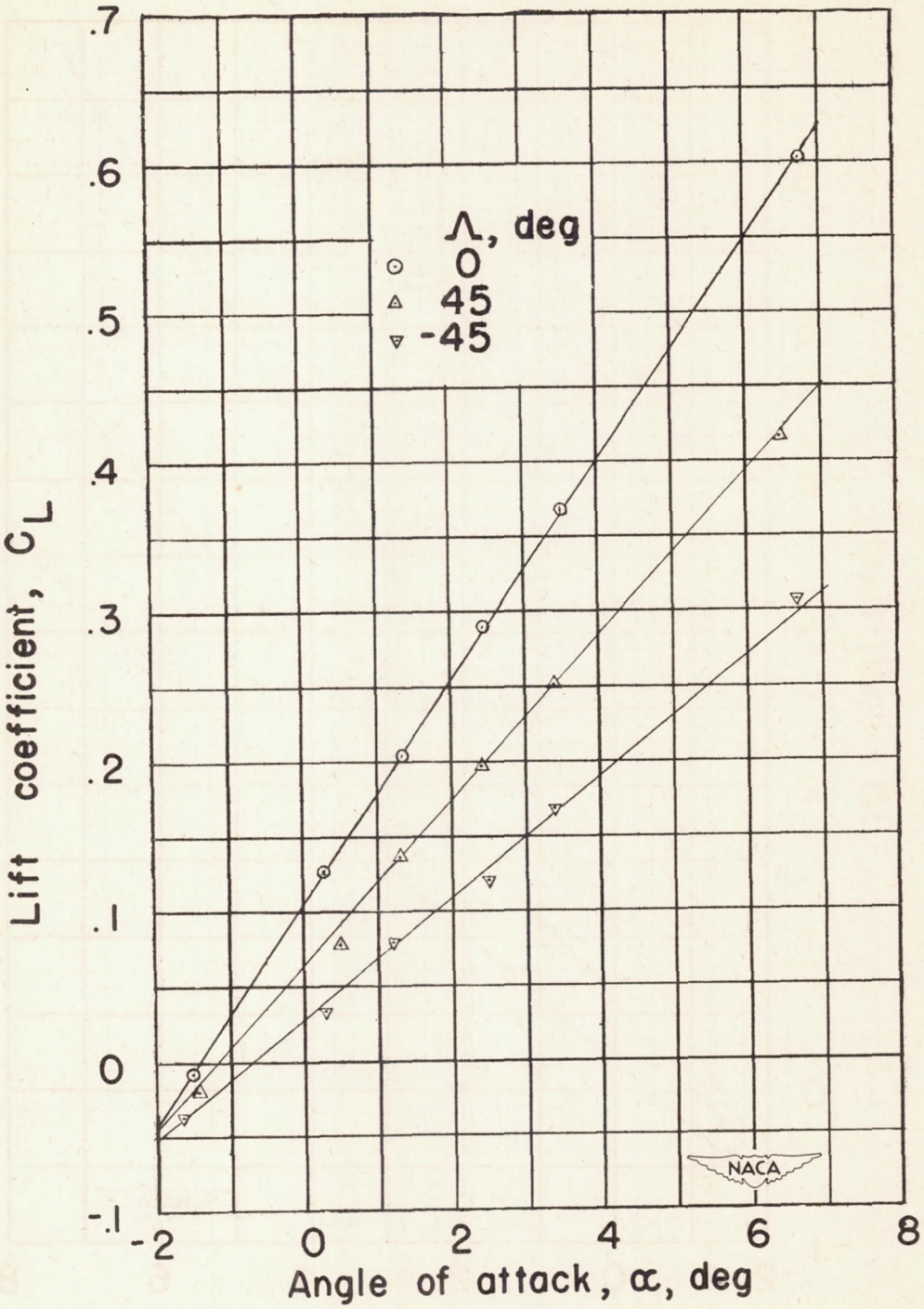
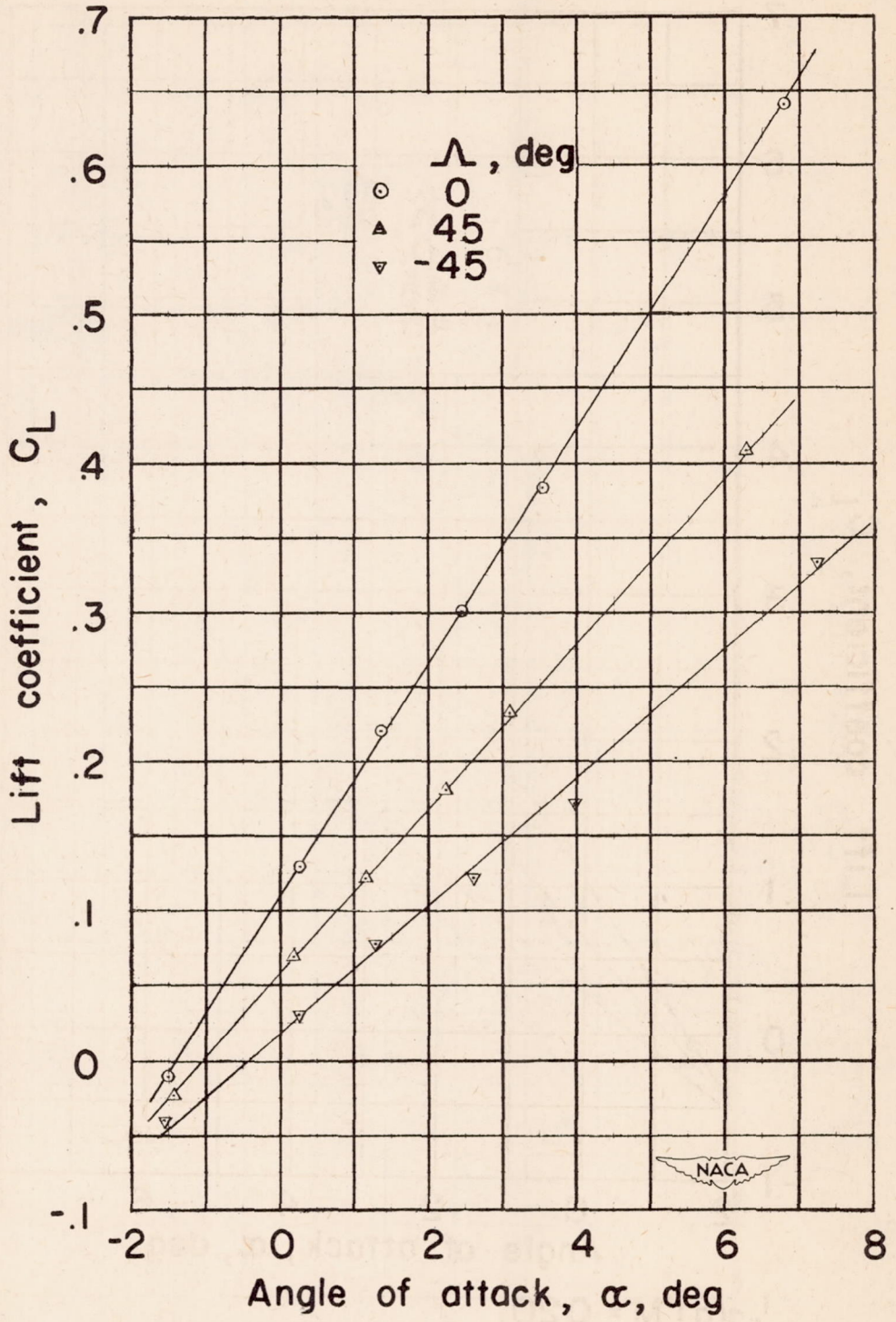


Figure 13. — Variation of spanwise load distribution with angle of sweep. M = 0.61.



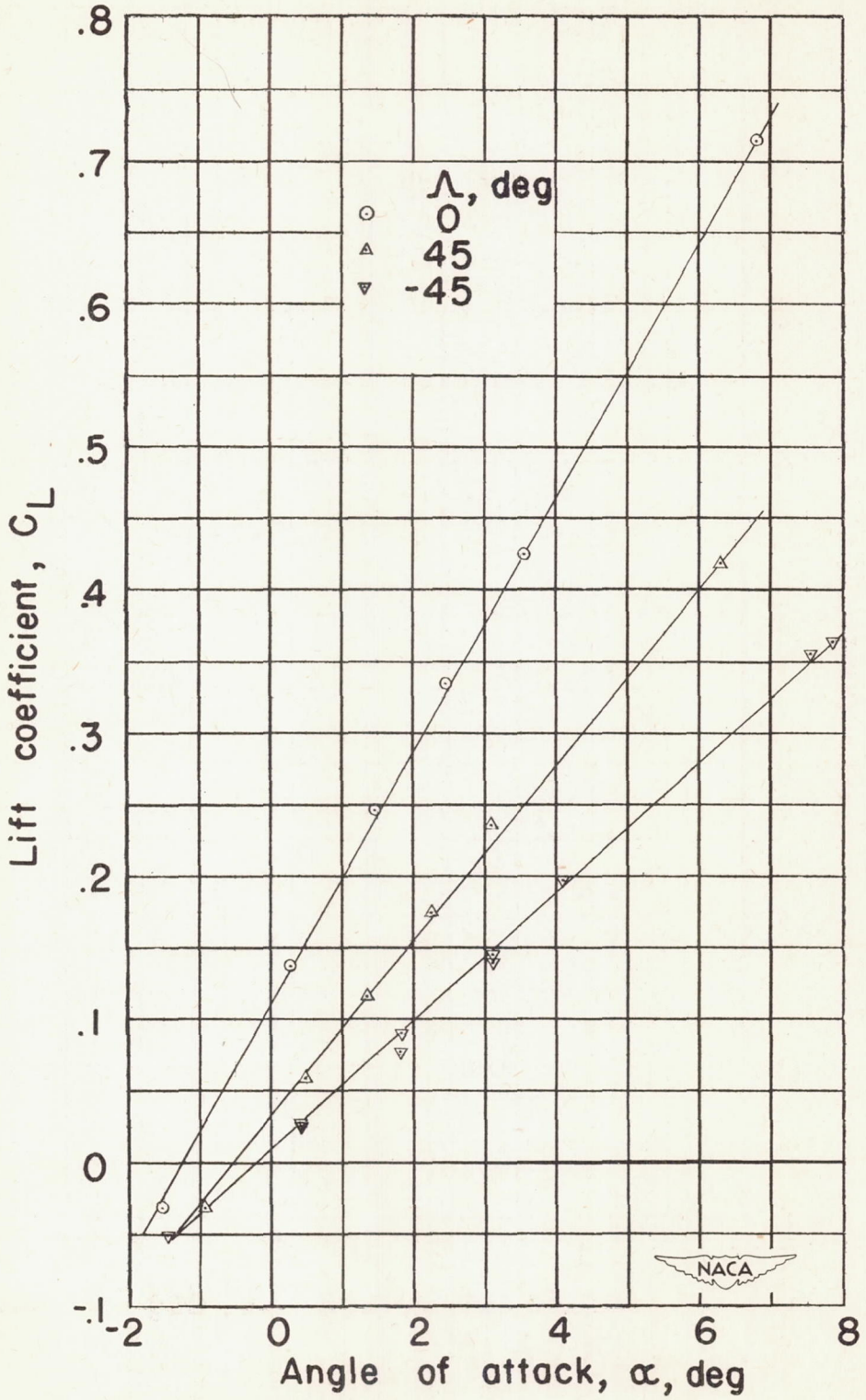
(a) M = 0.20.

Figure 14.—Variation of lift coefficient with angle of attack for wing-nacelle combination.



(b) M=0.40.

Figure 14. — Continued.



(c) M = 0.61.

Figure 14. — Concluded.

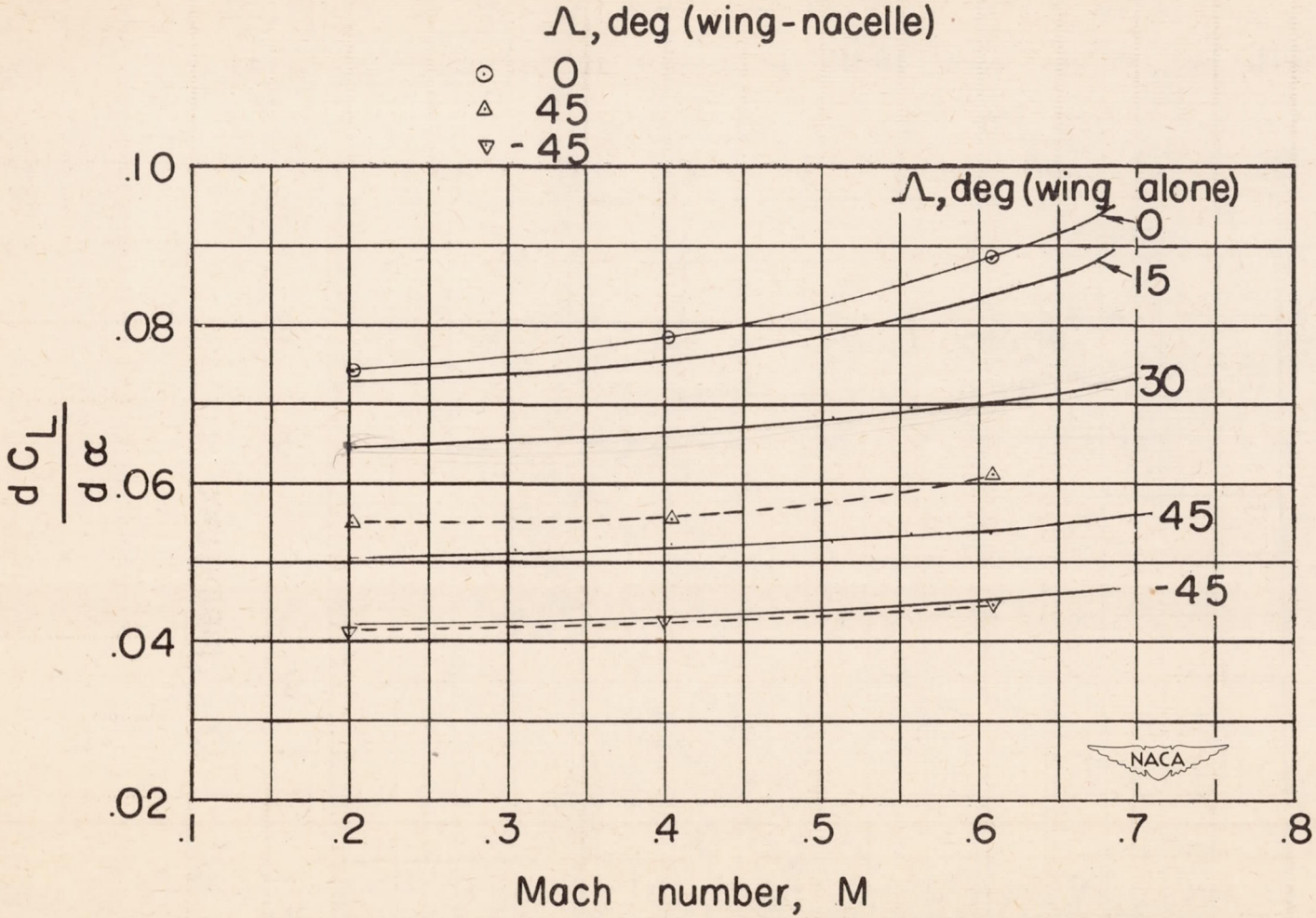


Figure 15.— Variation of lift-curve slope with Mach number for wing alone and wing-nacelle combination.

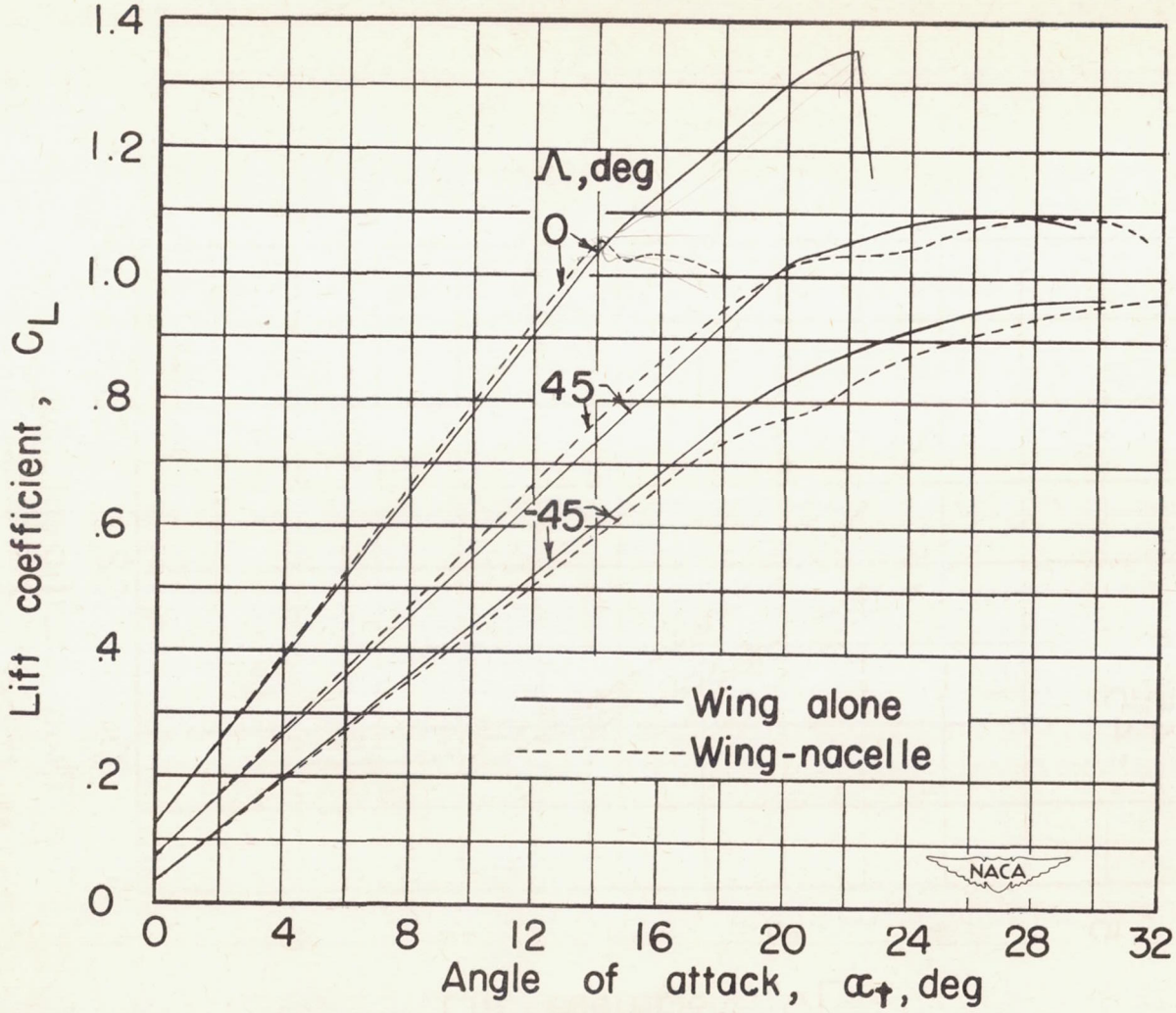
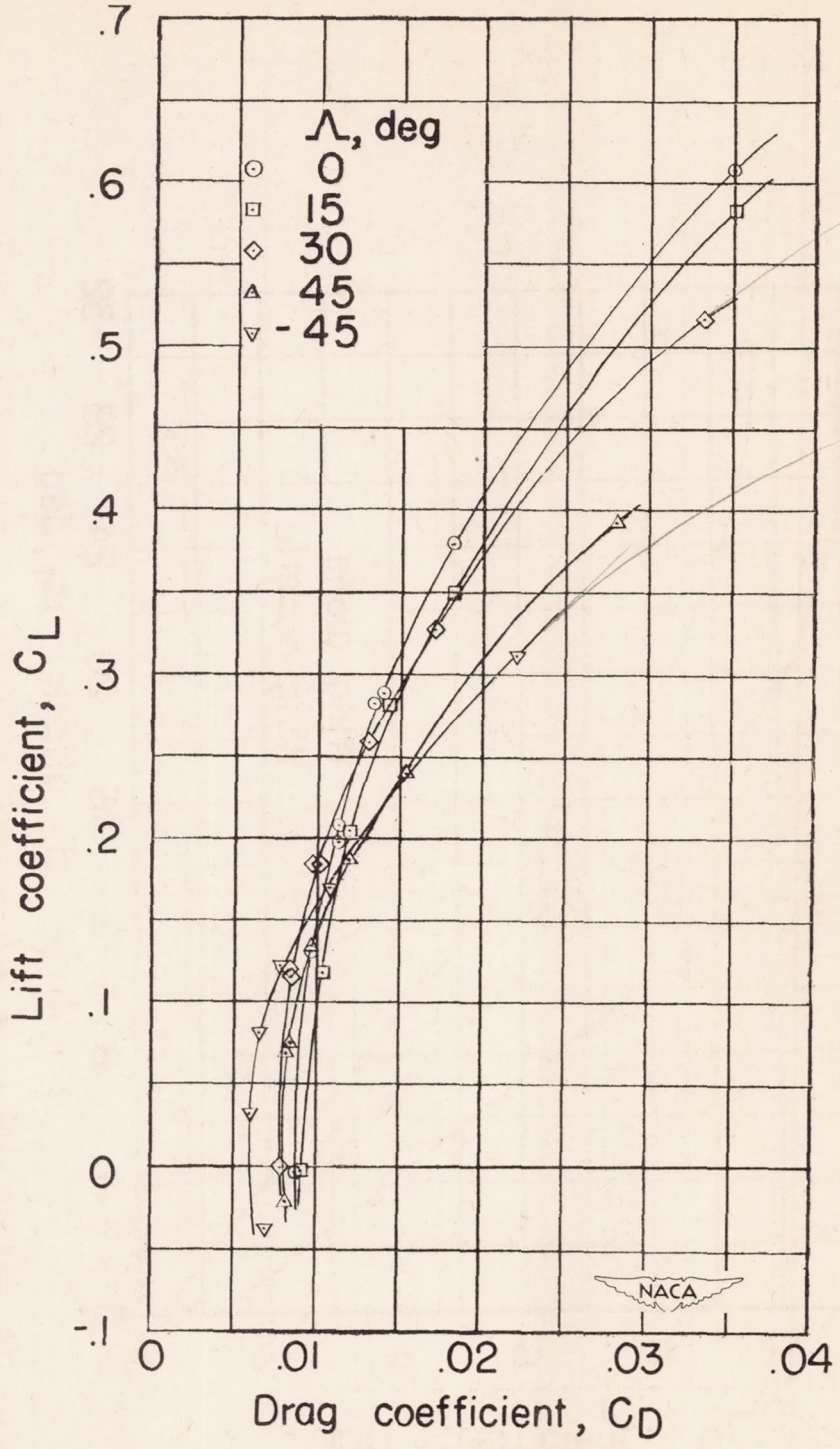
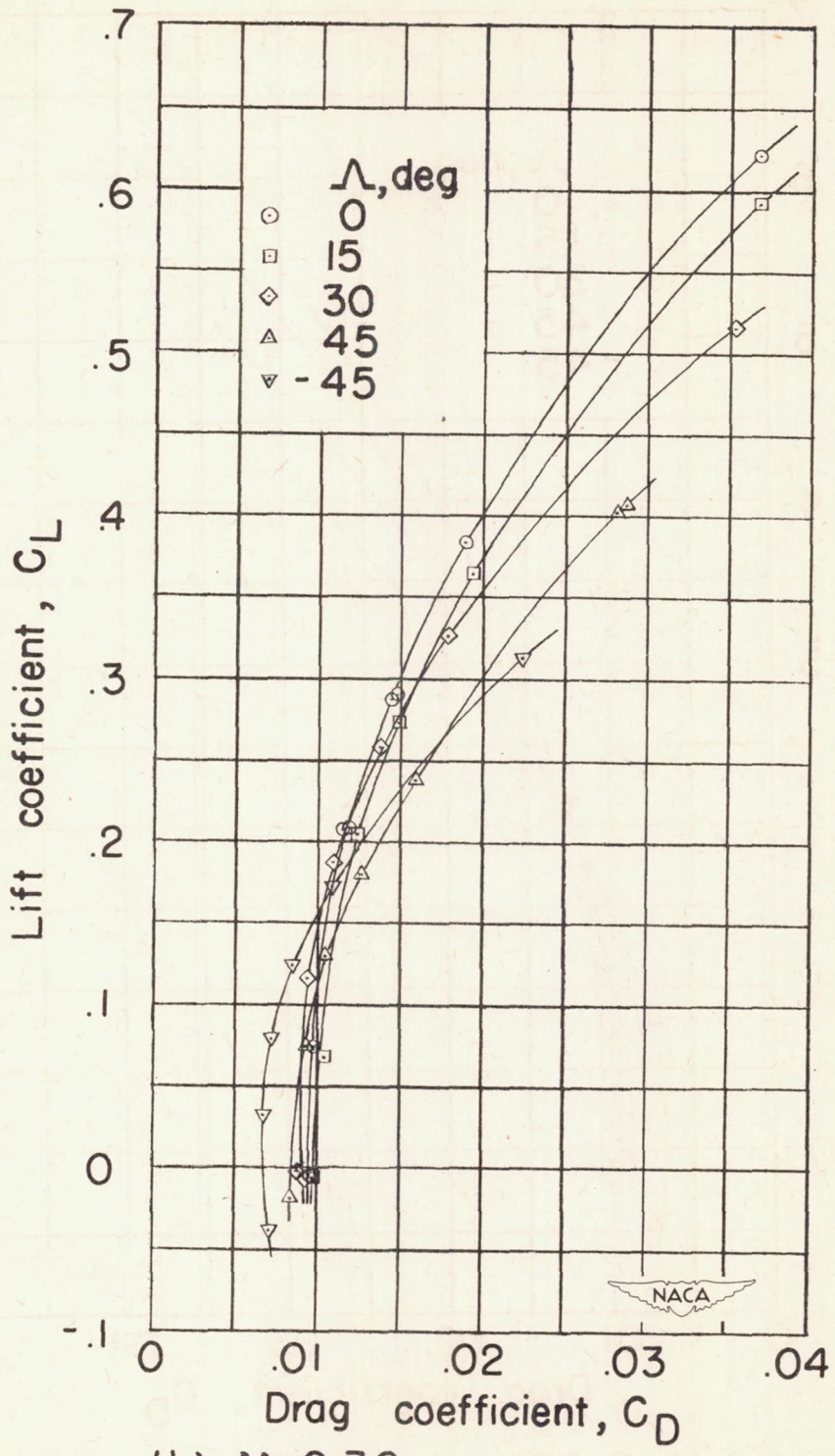


Figure 16.—Variation of lift coefficient with angle of attack for wing alone and wing-nacelle combination. M=0.13.



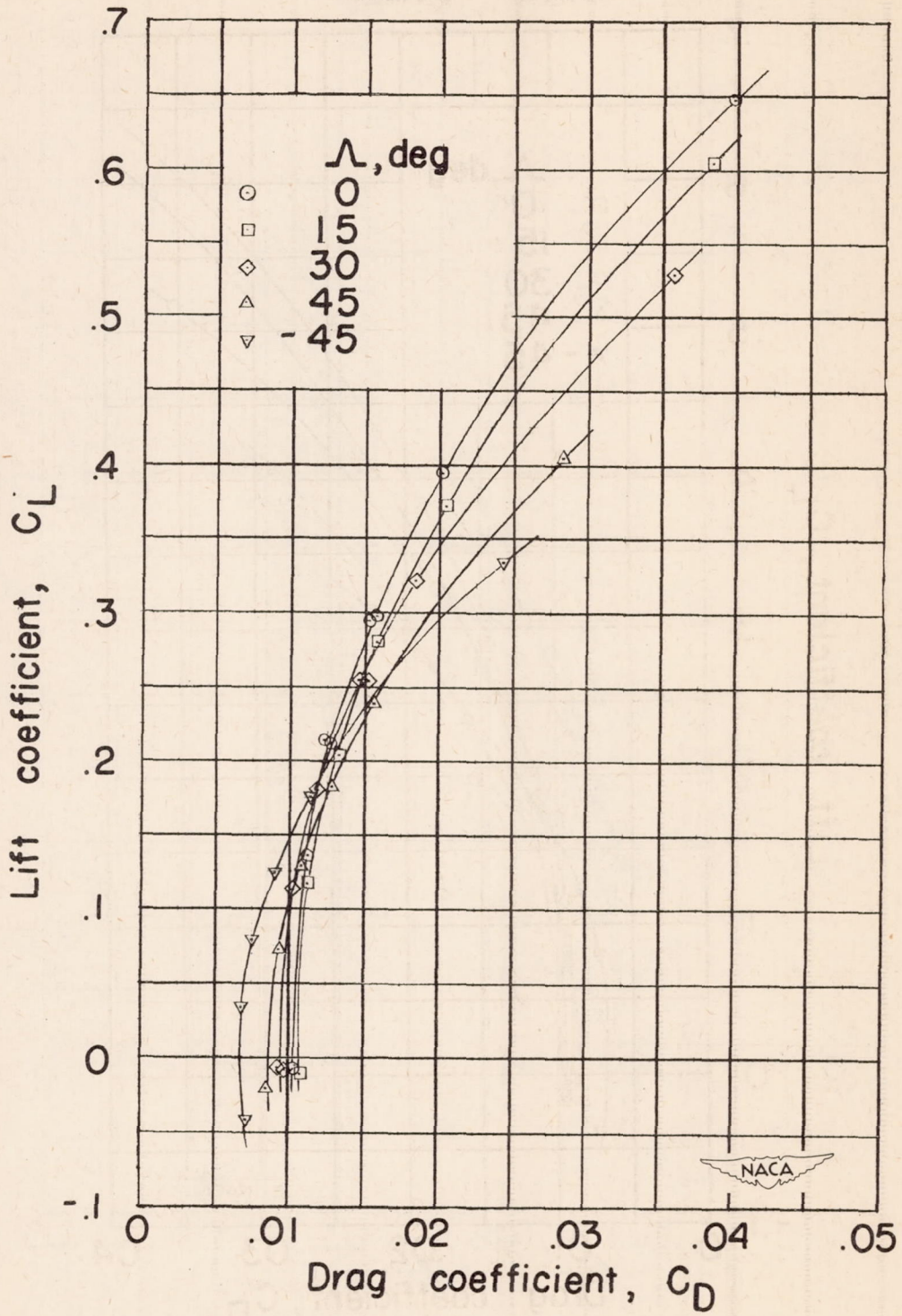
(a) M = 0.20.

Figure 17.—Variation of drag coefficient with lift coefficient for wing alone.



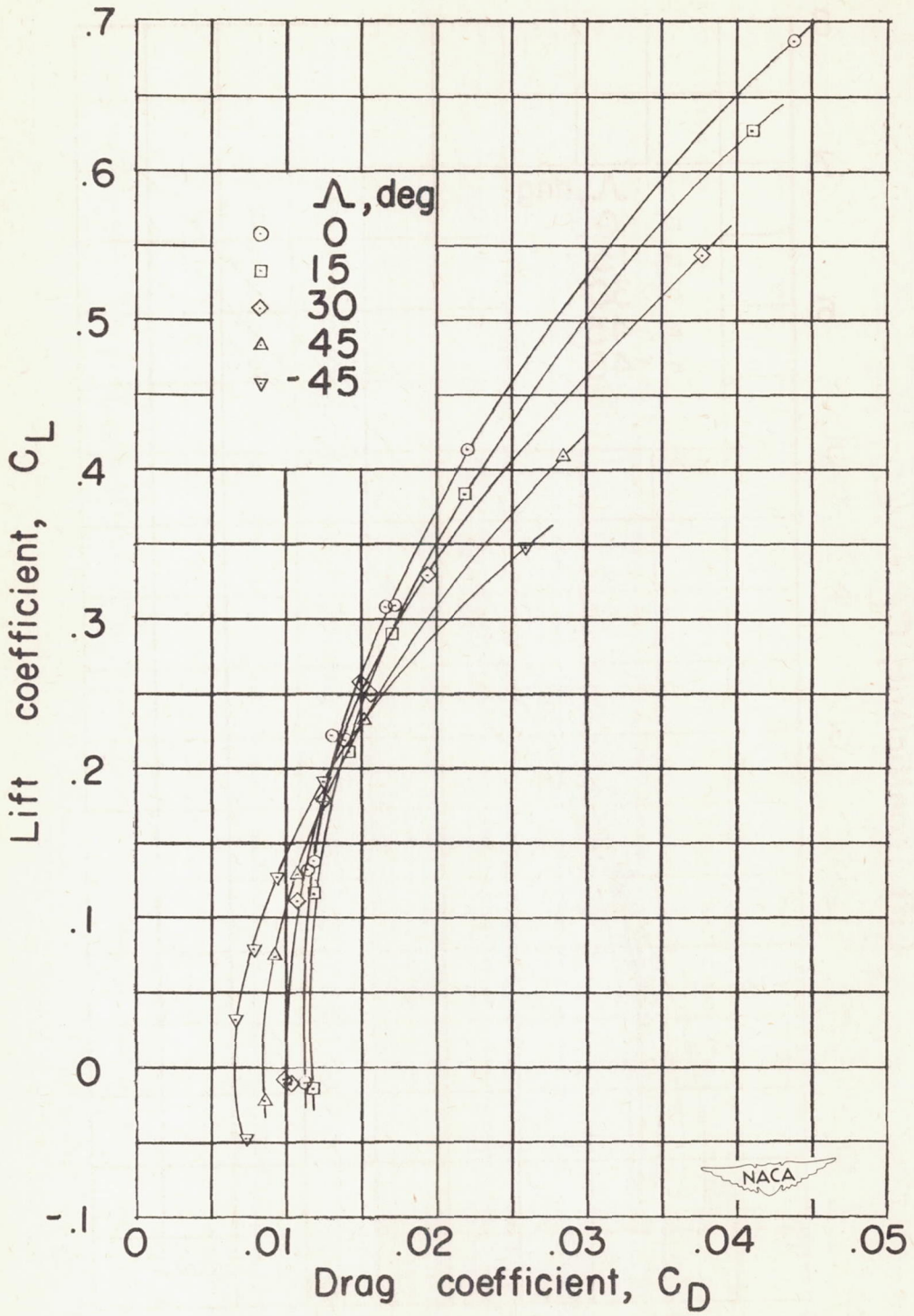
(b) M=0.30.

Figure 17.— Continued.



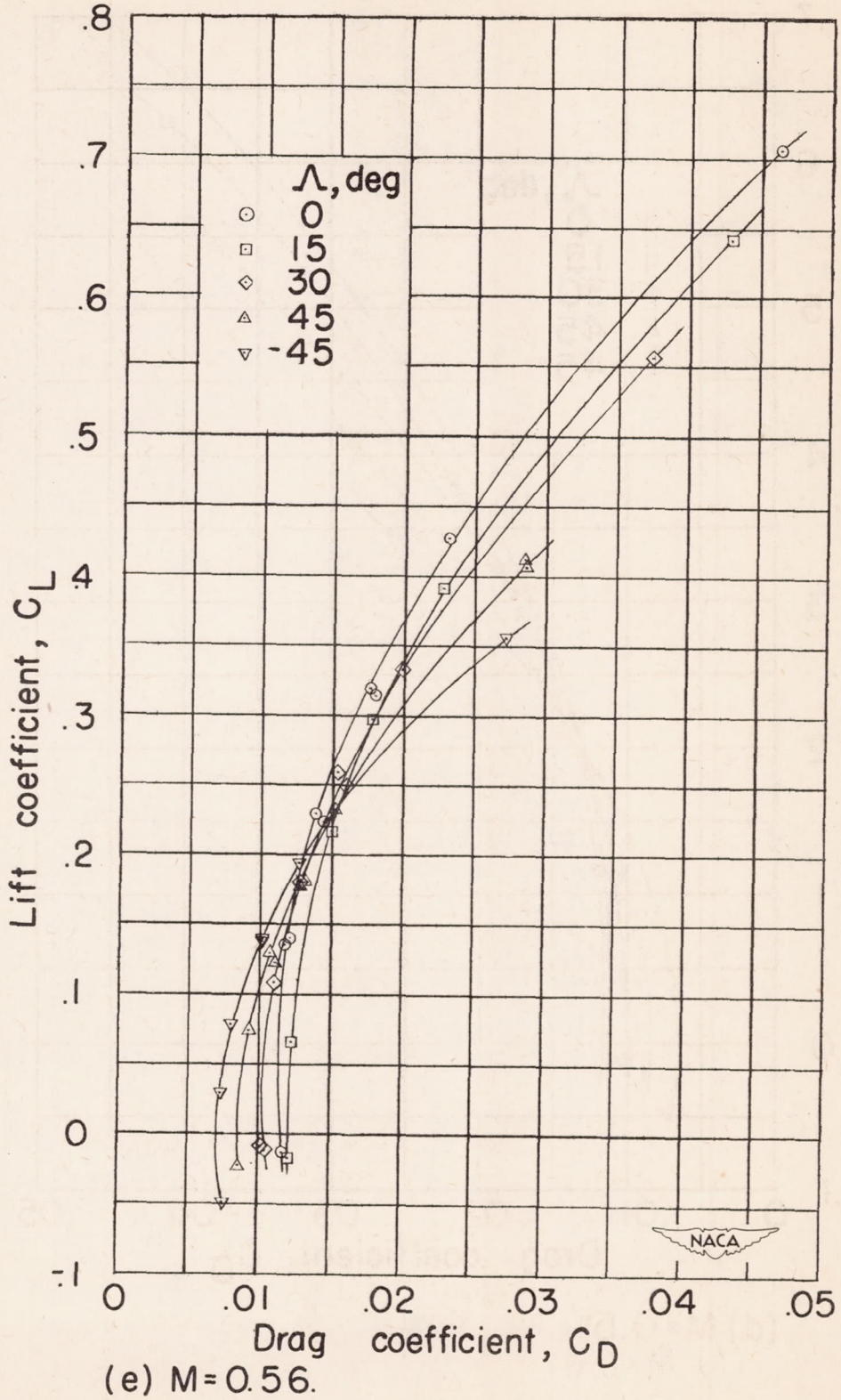
(c) M = 0.40.

Figure 17.— Continued.



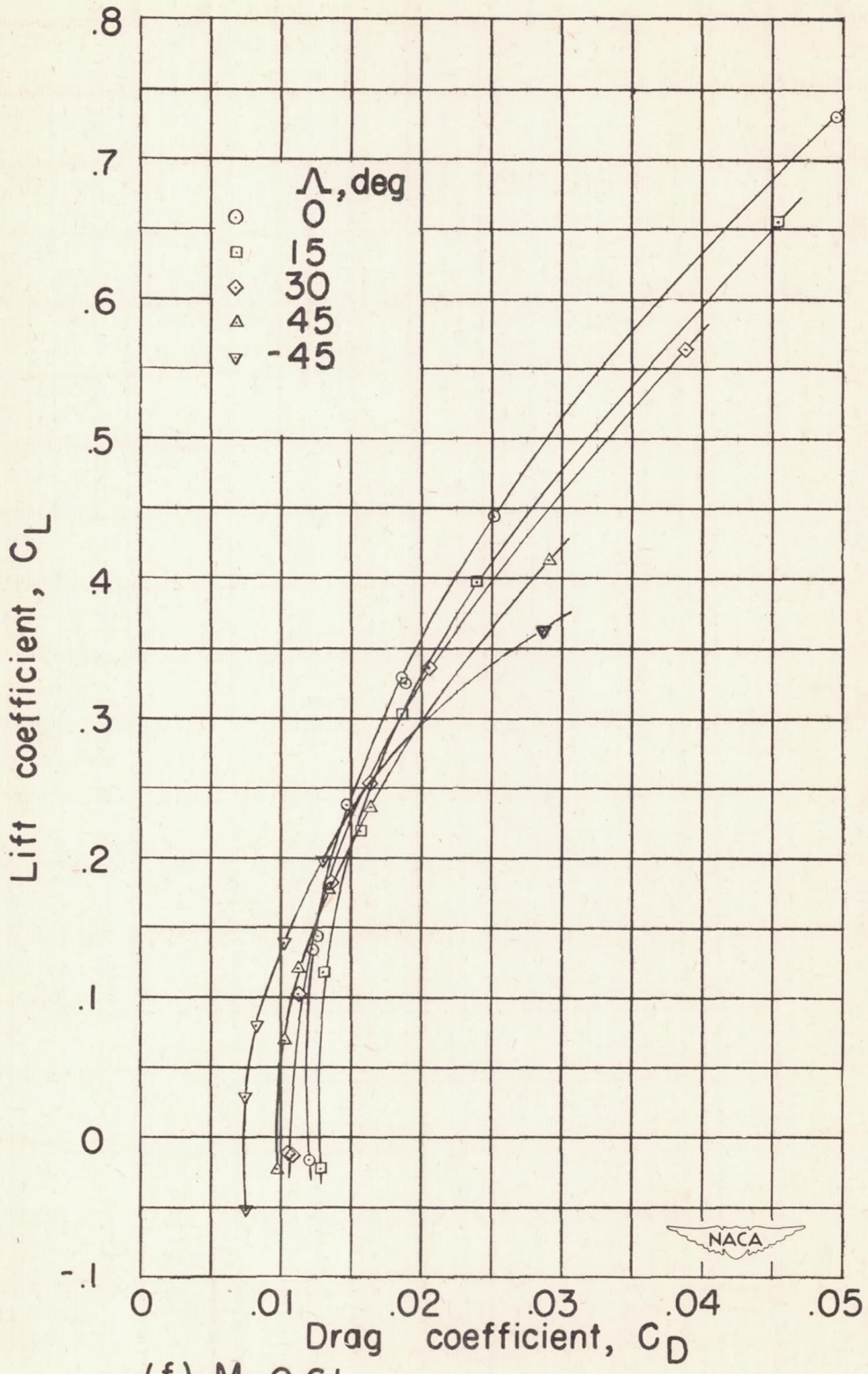
(d) M = 0.51.

Figure 17. — Continued.



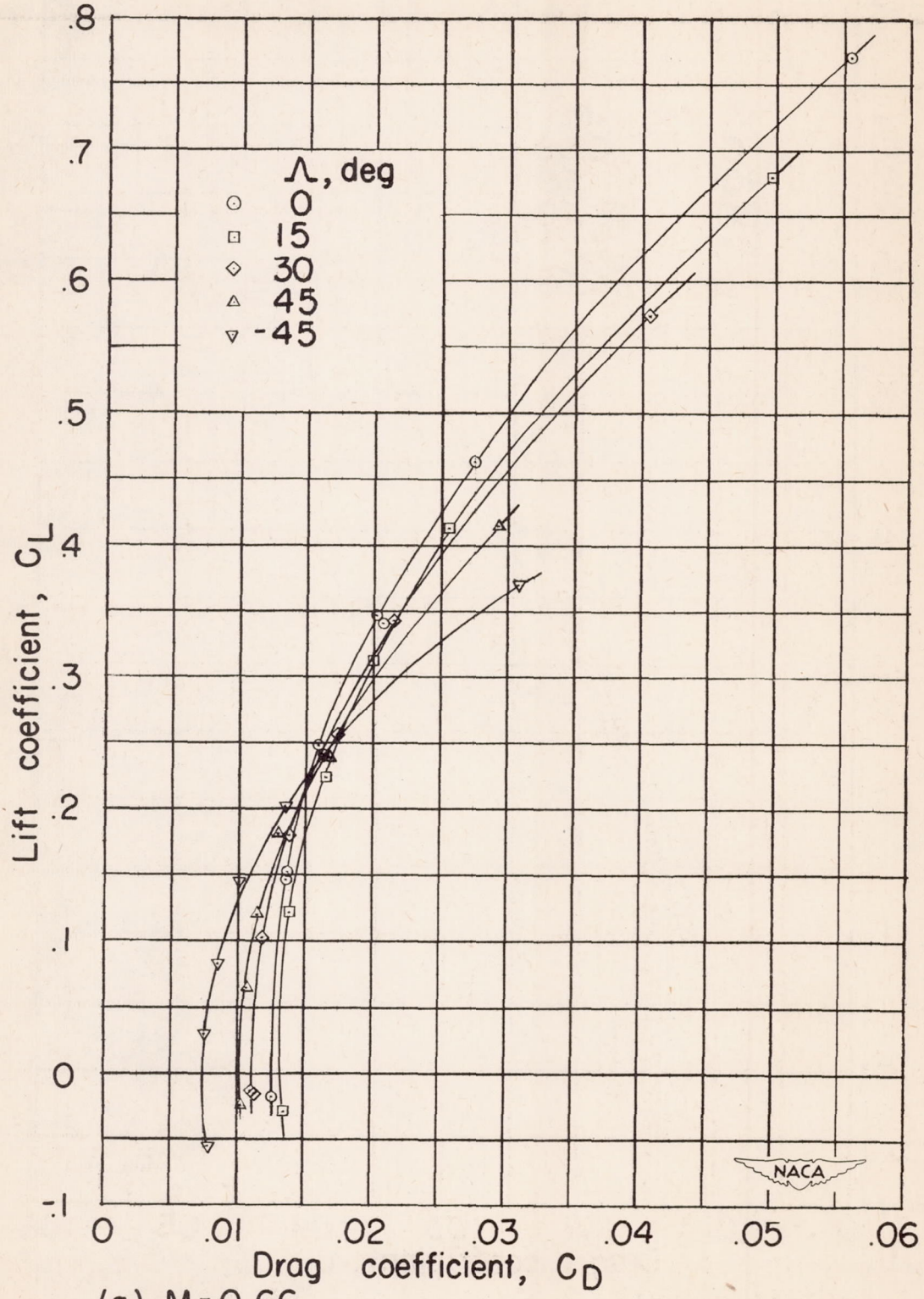
(e) M=0.56.

Figure 17.— Continued.



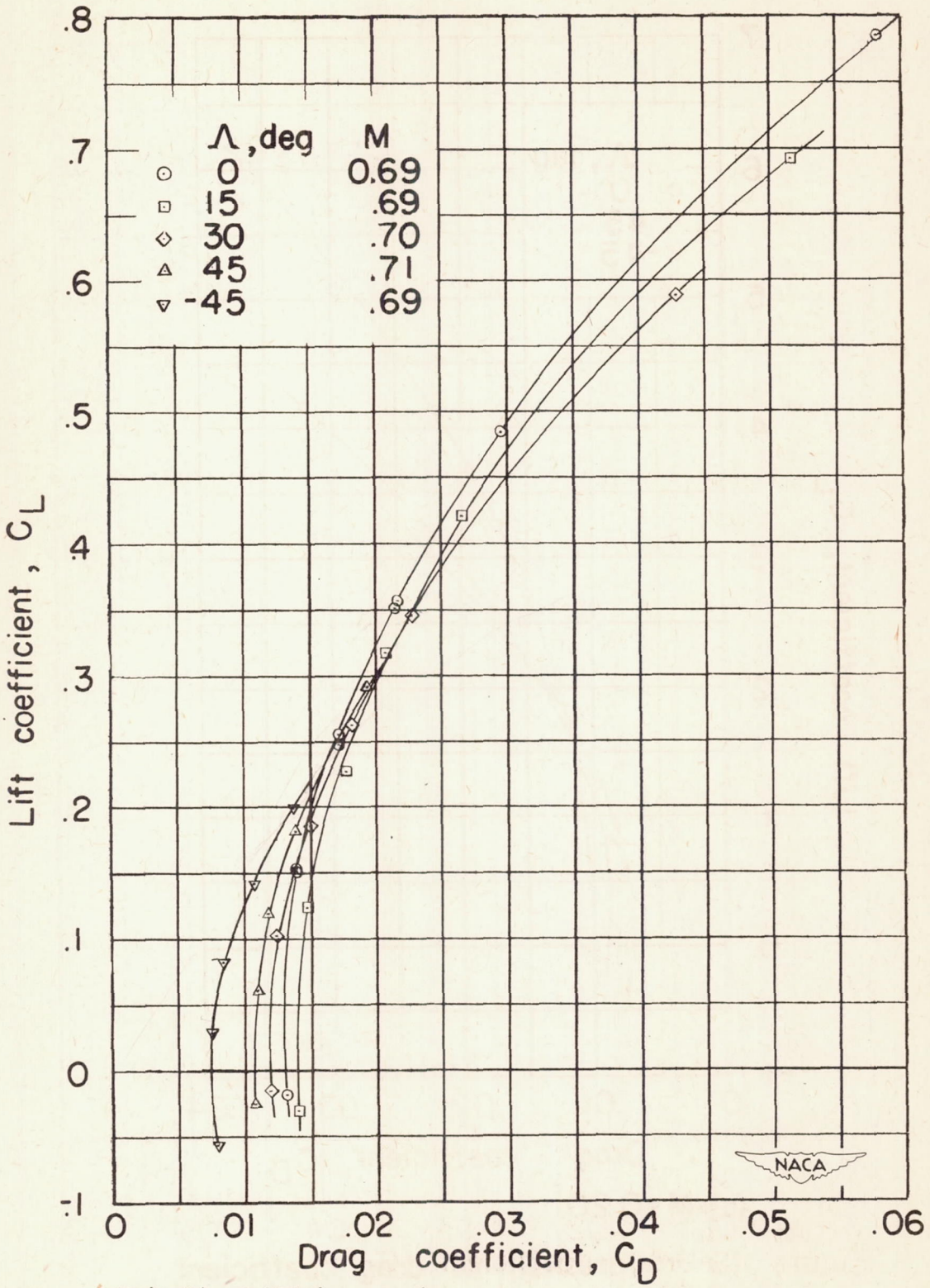
(f) M=0.61.

Figure 17.— Continued.



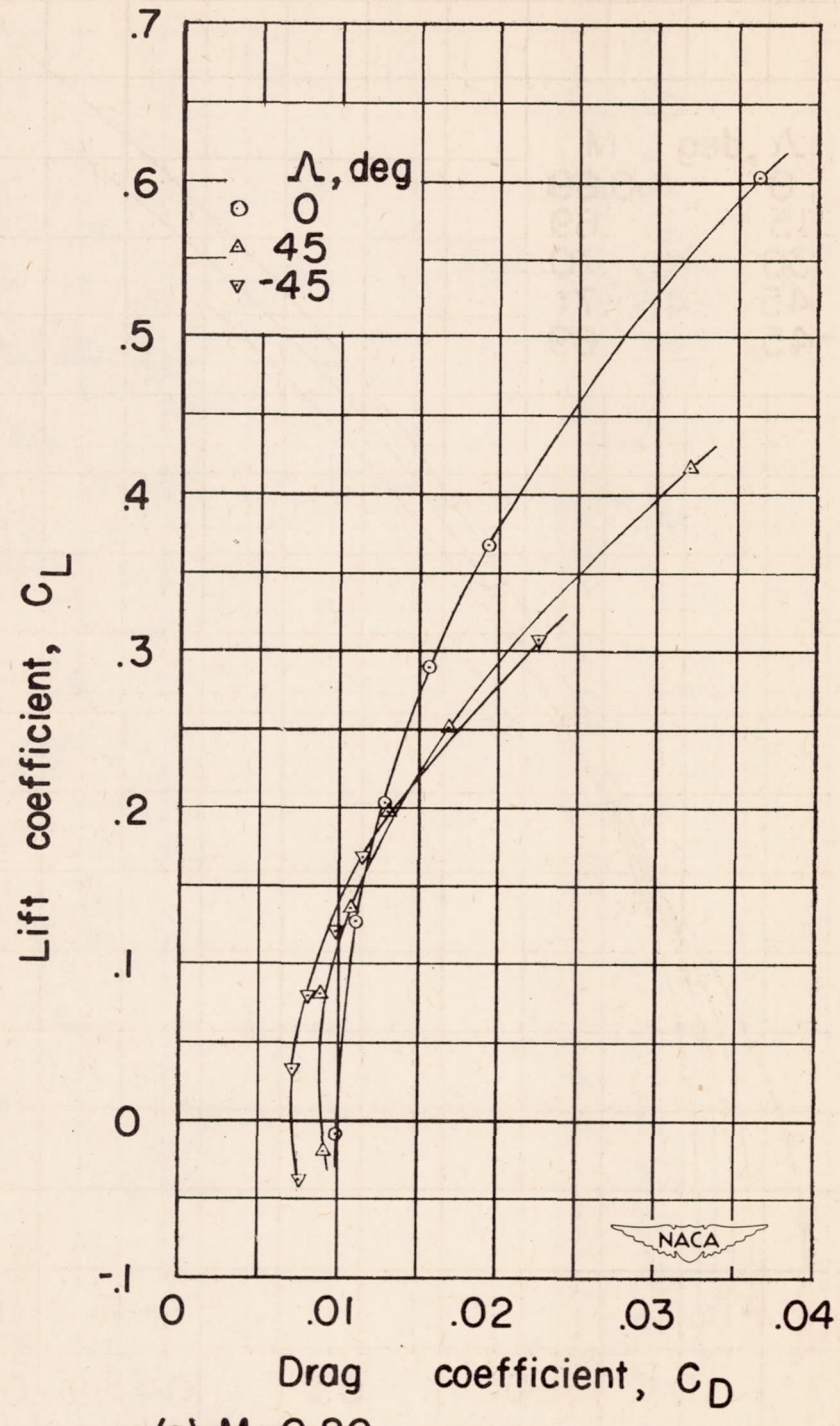
(g) M = 0.66.

Figure 17. — Continued.



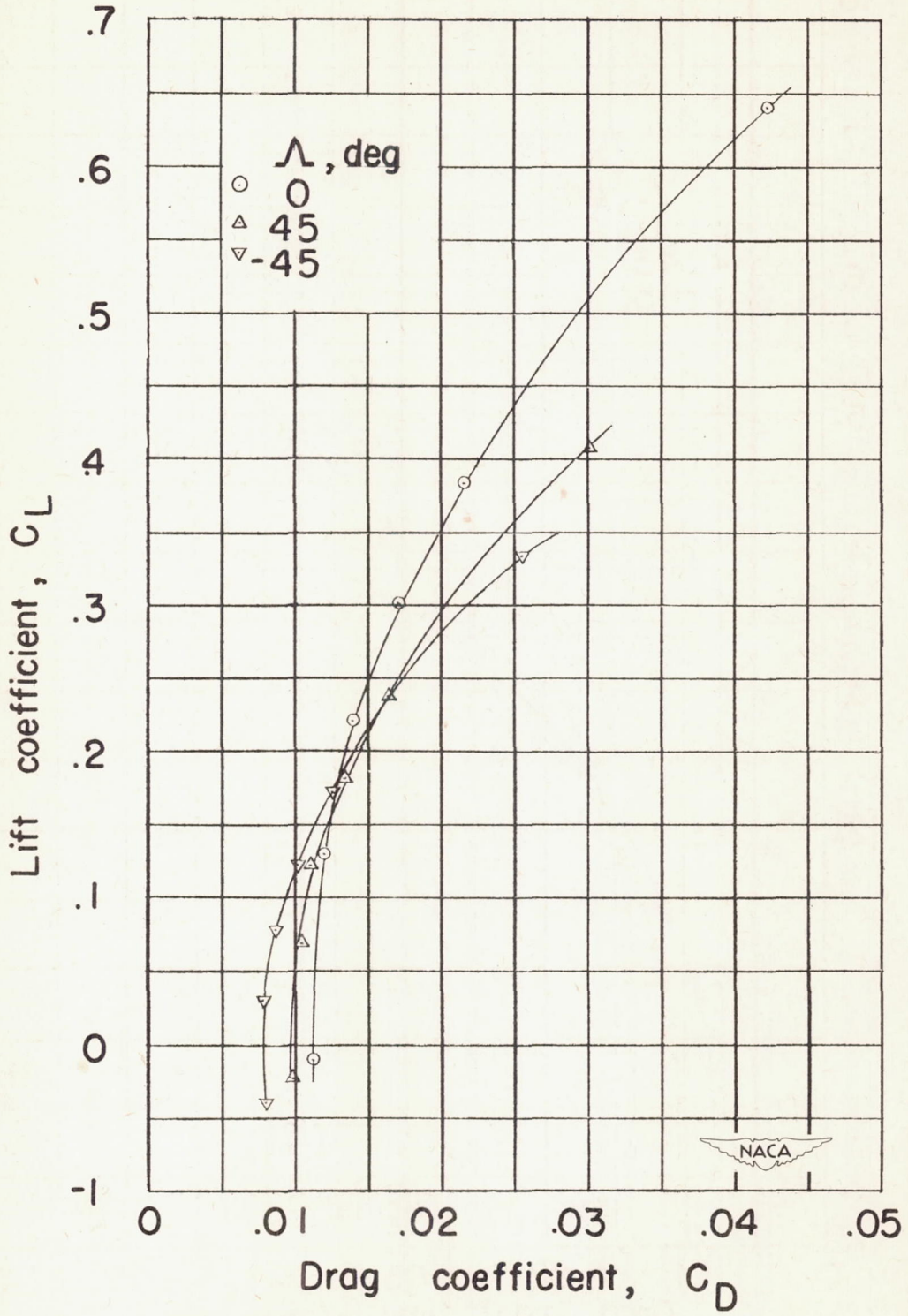
(h) M = 0.70 (approx).

Figure 17. — Concluded.



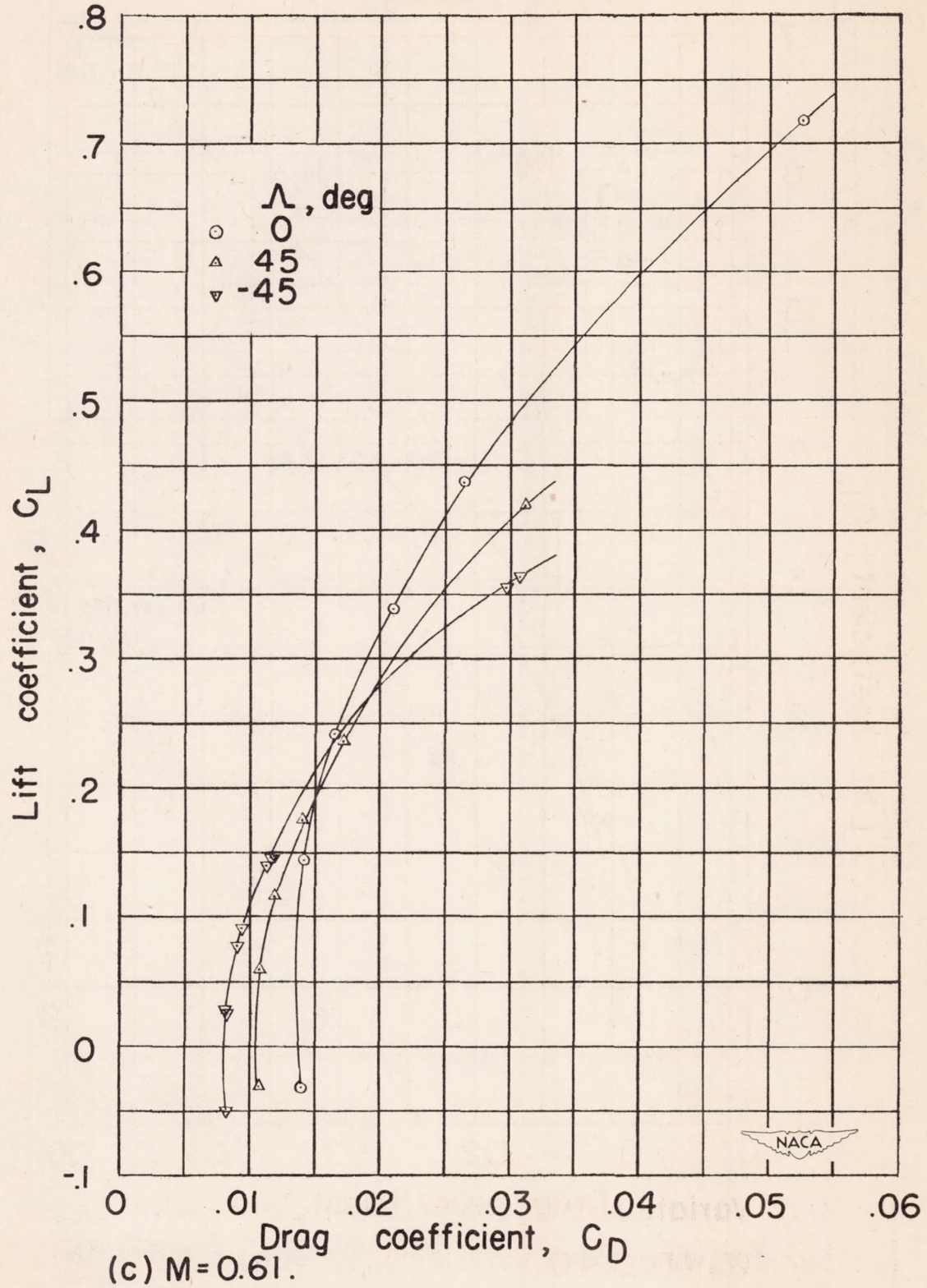
(a) M = 0.20.

Figure 18. — Variation of drag coefficient with lift coefficient for wing-nacelle combination.



(b) M= 0.40.

Figure 18.— Continued.



(c) M = 0.61.

Figure 18.— Concluded.

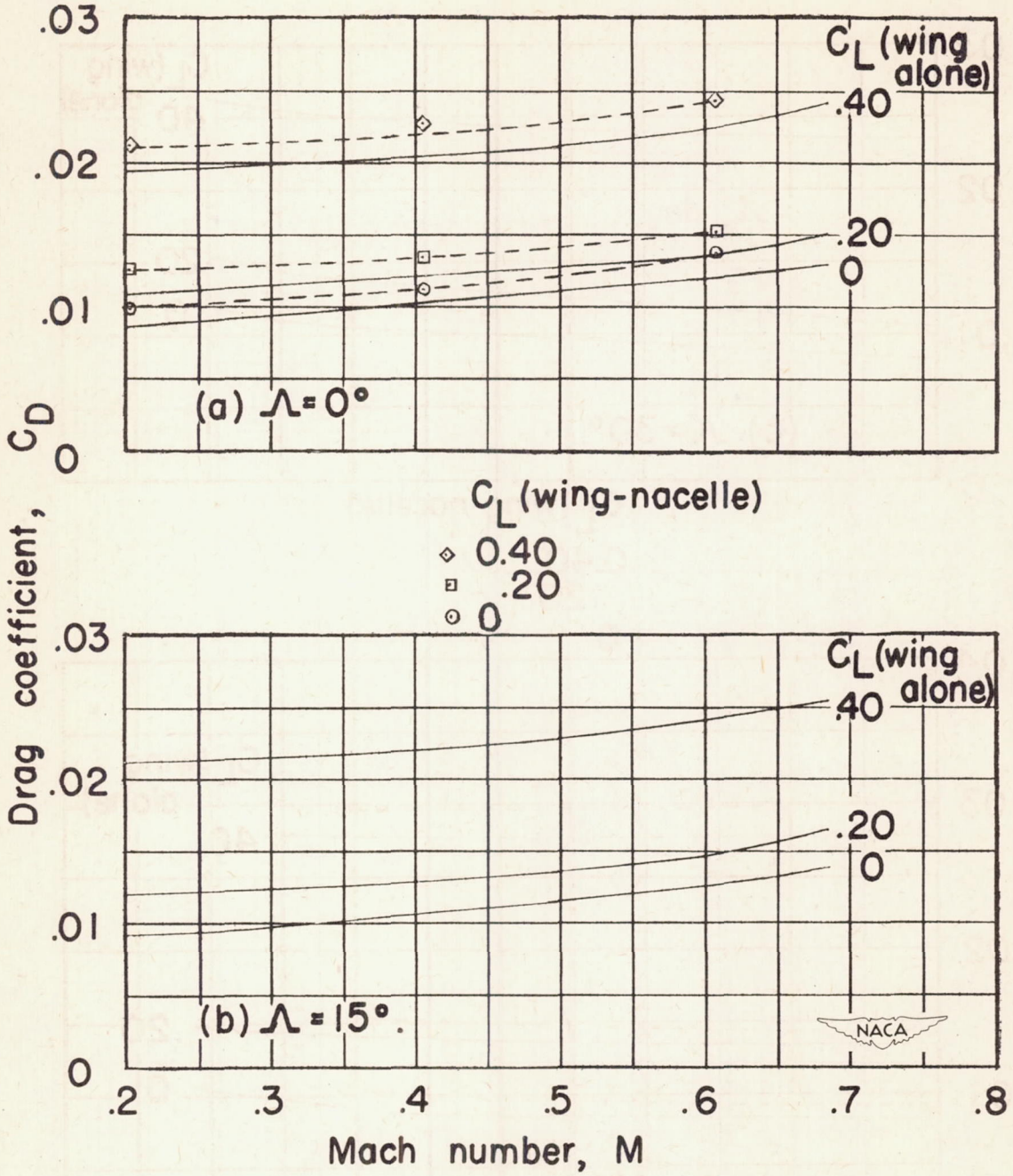


Figure 19.— Variation of drag coefficient with Mach number for wing alone and wing-nacelle combination.

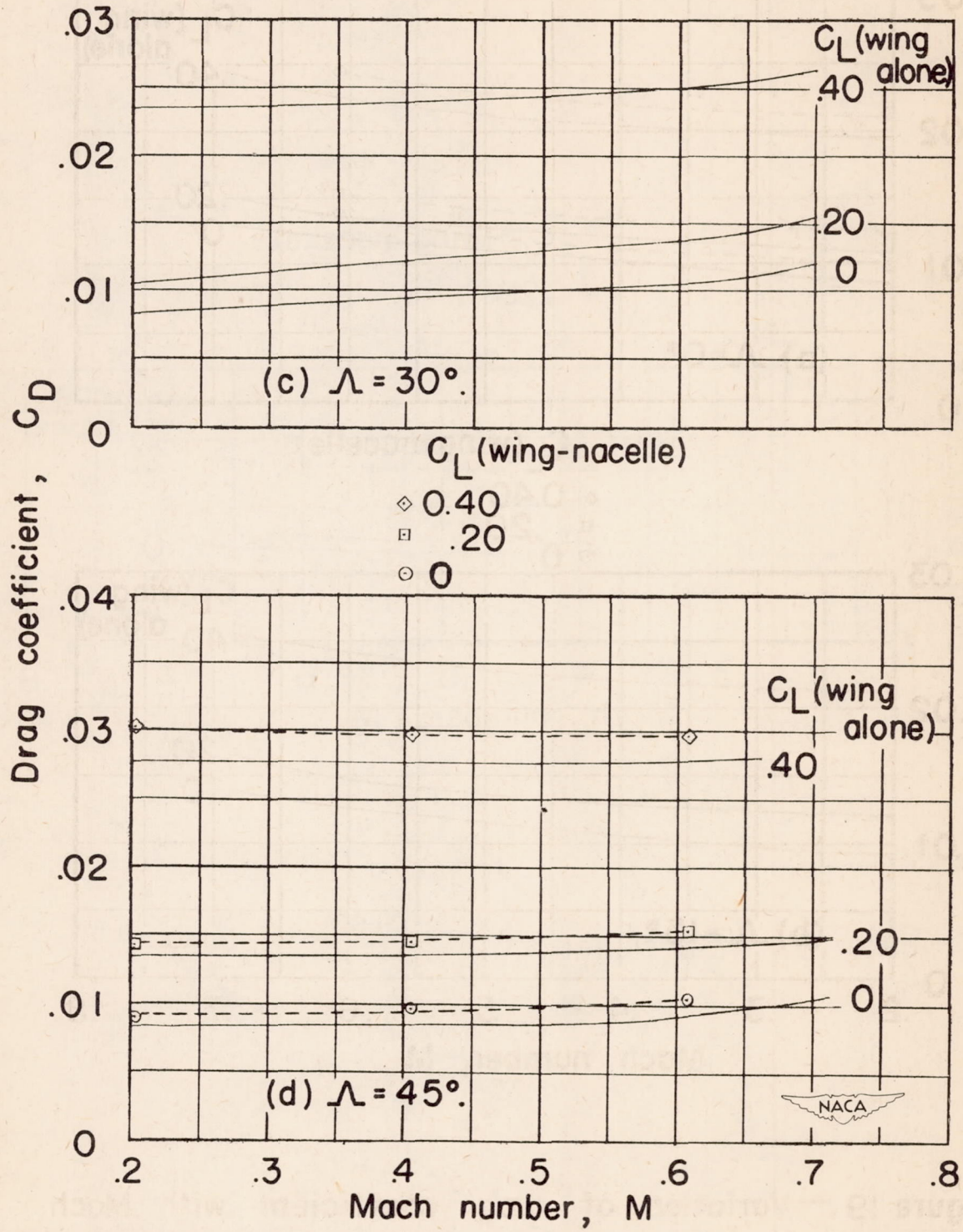
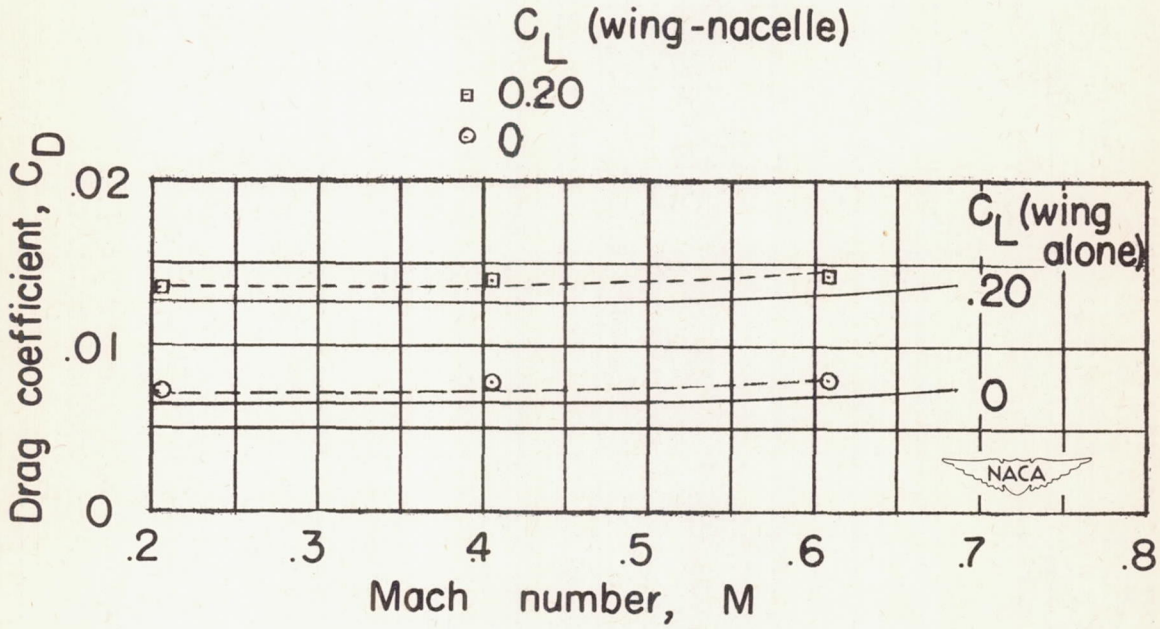


Figure 19. — Continued.



(e) $\Lambda = -45$.

Figure 19. — Concluded.

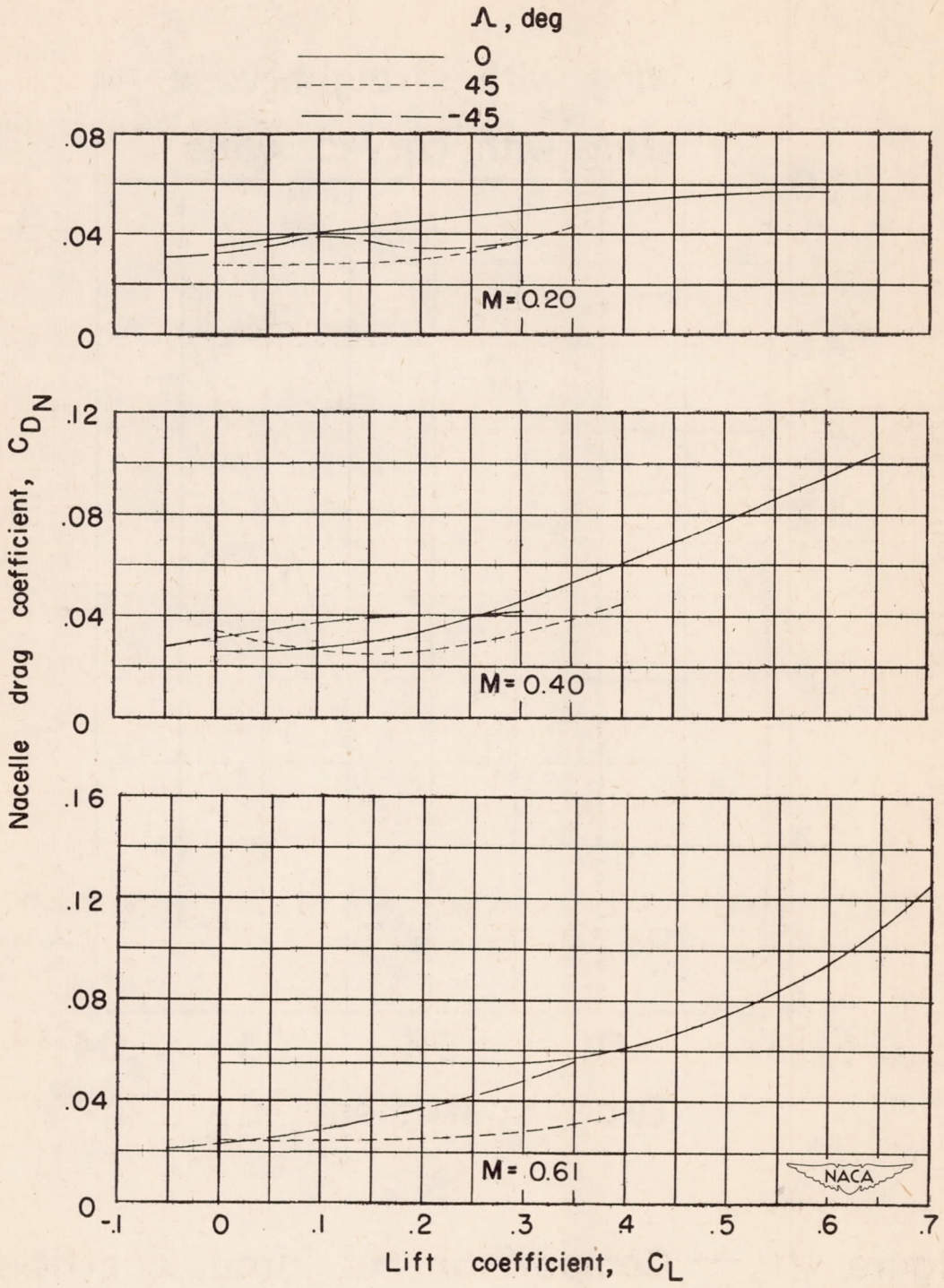


Figure 20. — Variation of nacelle drag coefficient with lift coefficient.

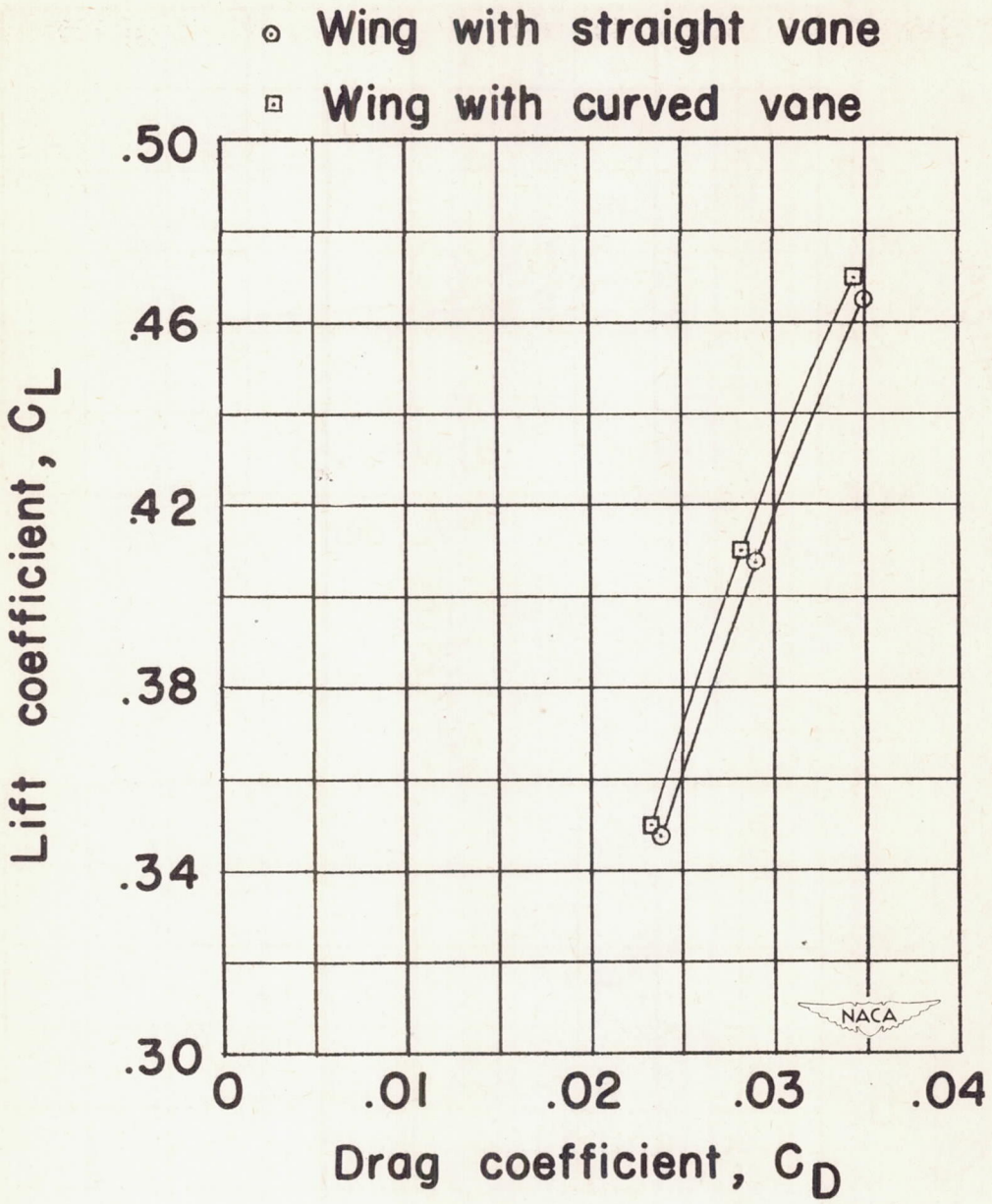


Figure 21.— Comparison of drag coefficient for wing with straight vane and wing with curved vane. $\Lambda = 45°$; $M = 0.56$.

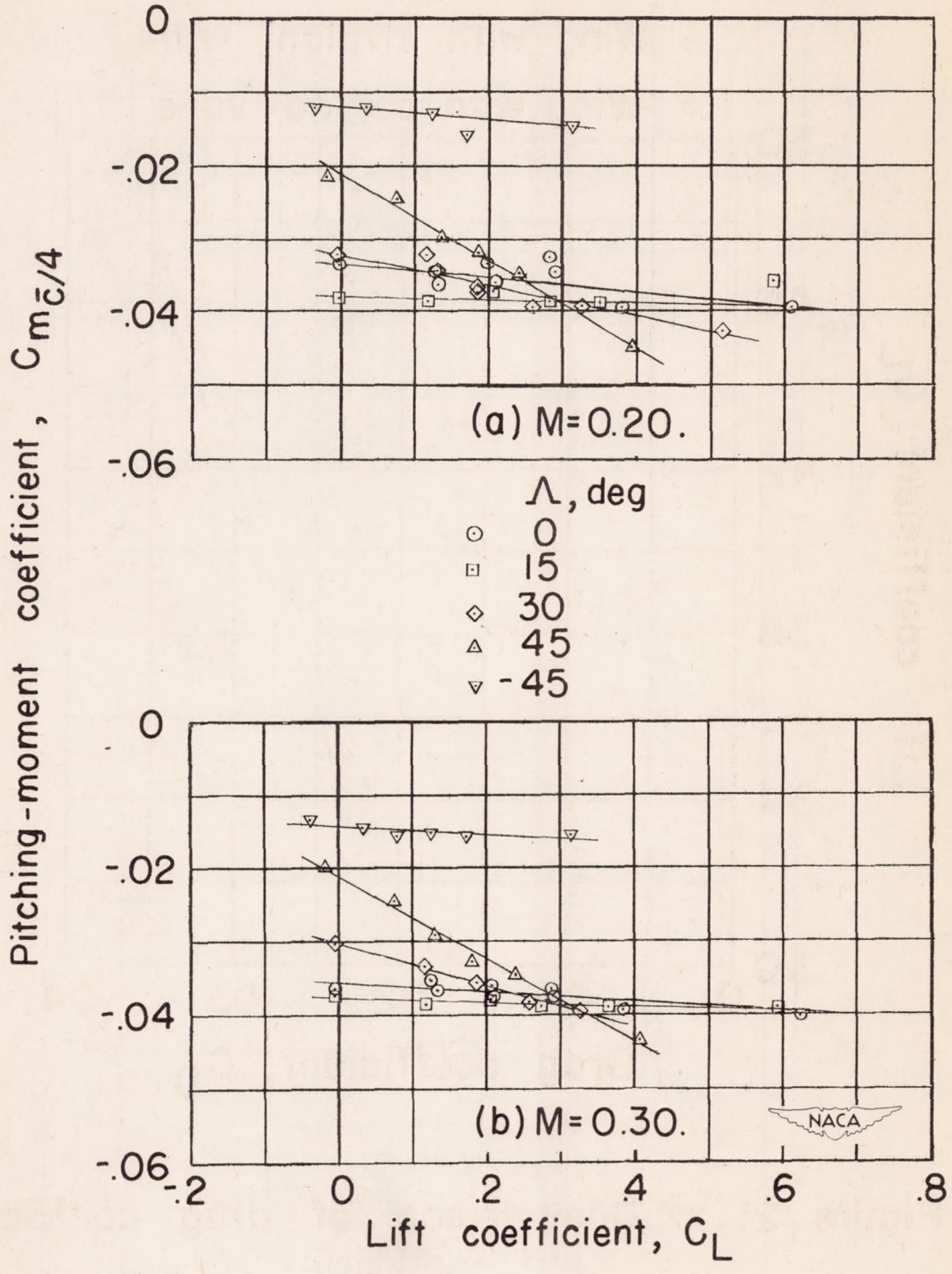


Figure 22.—Variation of pitching-moment coefficient with lift coefficient for wing alone.

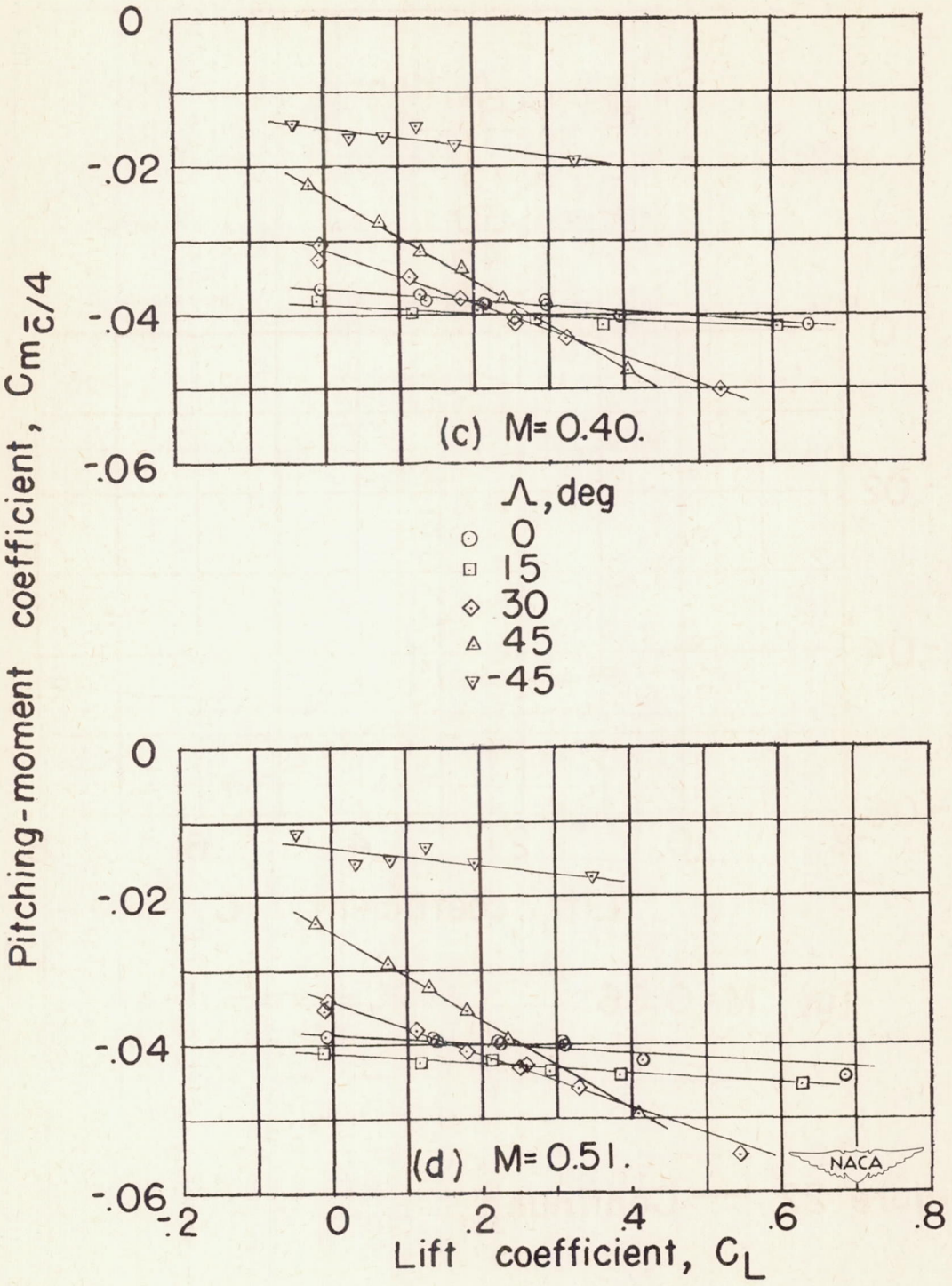
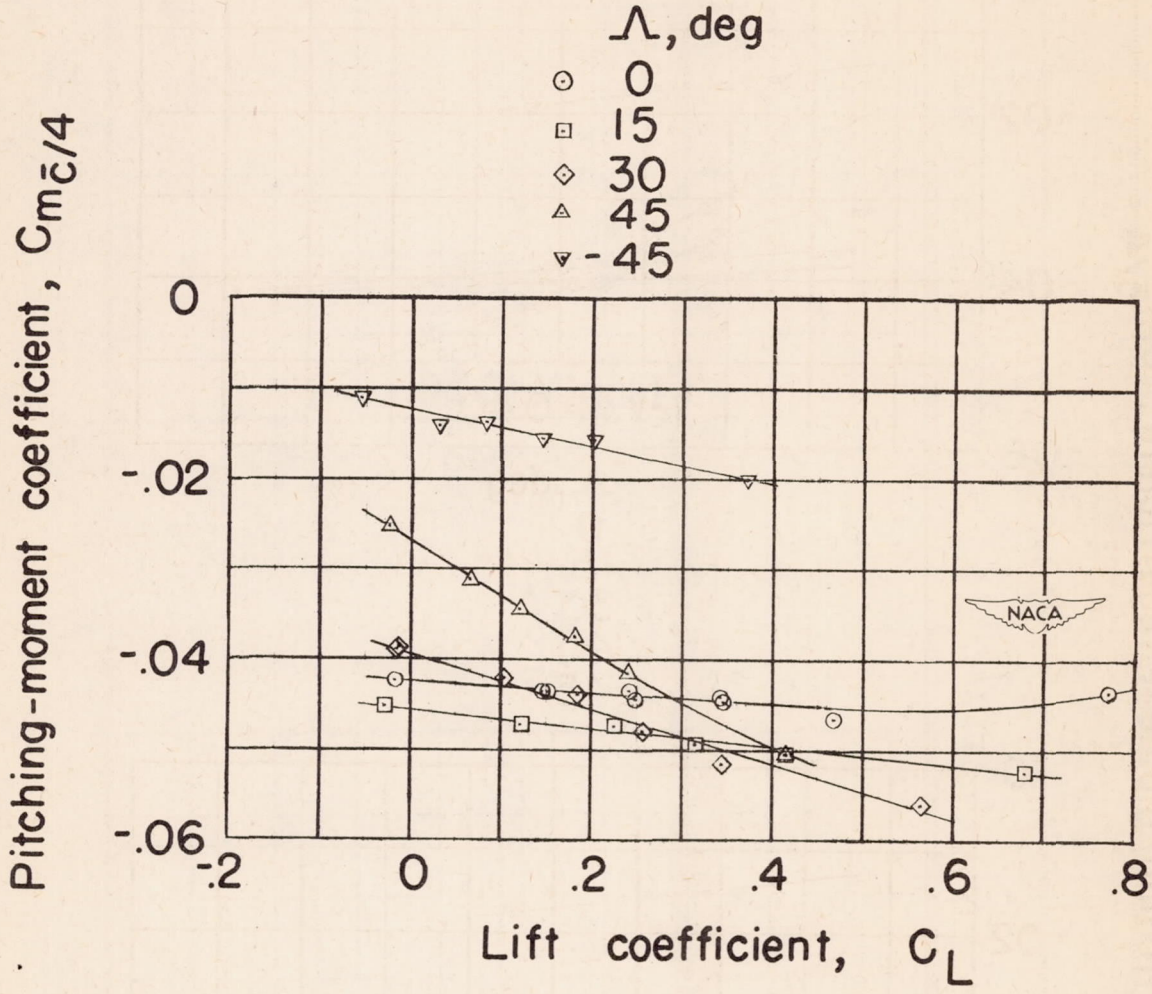


Figure 22.— Continued.



(g) M=0.66.

Figure 22. — Continued.

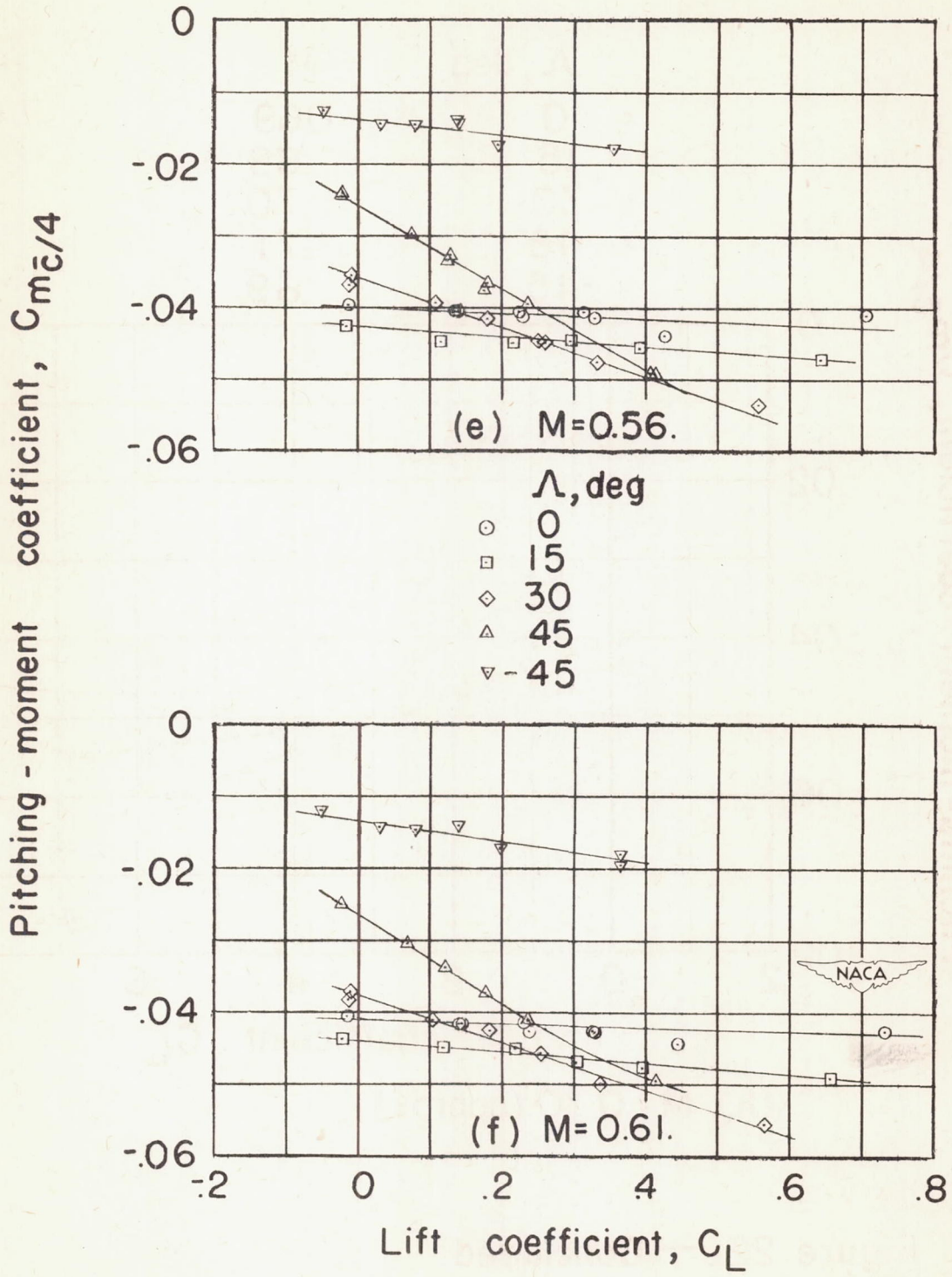
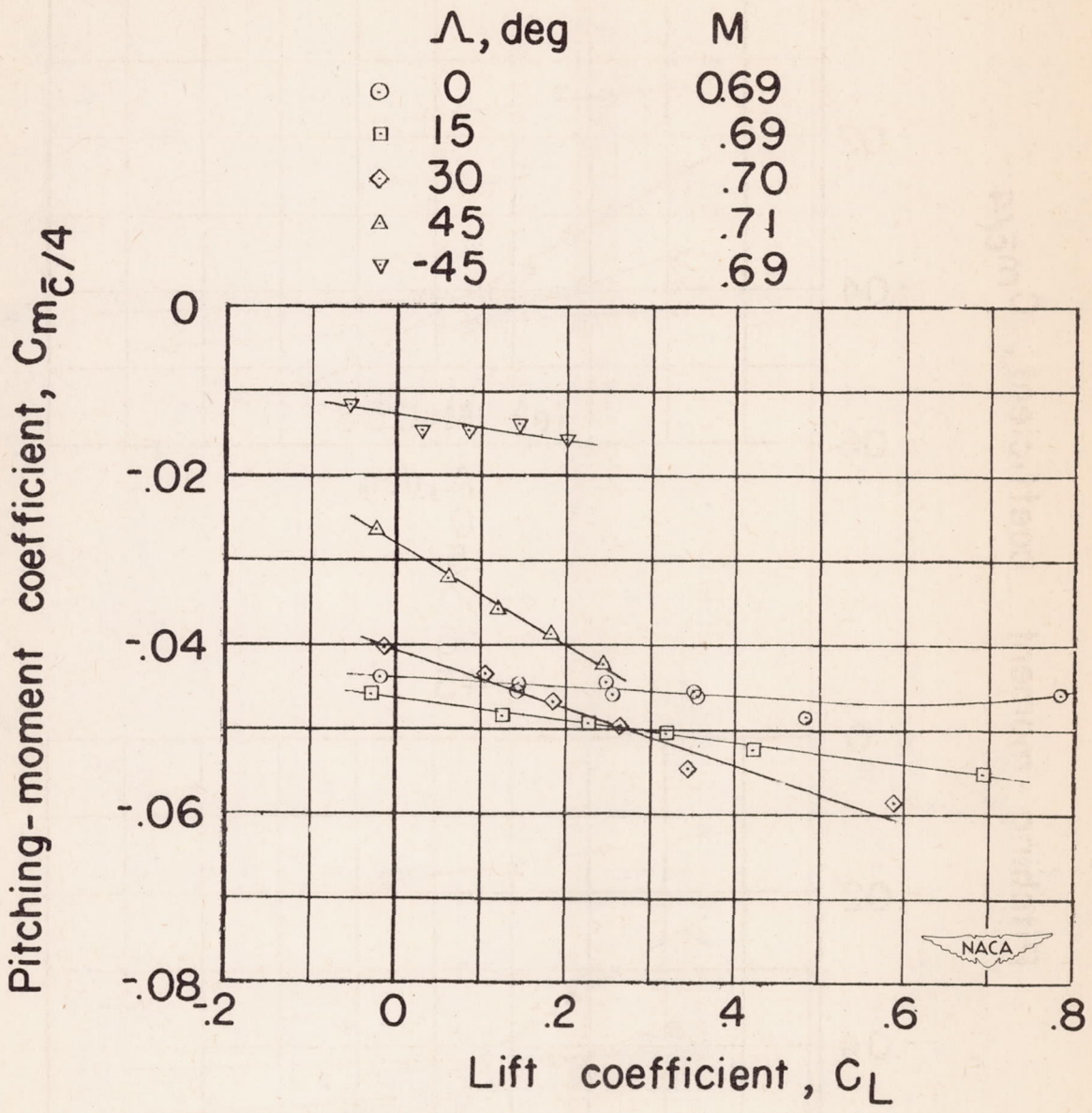


Figure 22. — Continued.



(h) M = 0.70 (approx.).

Figure 22. — Concluded.

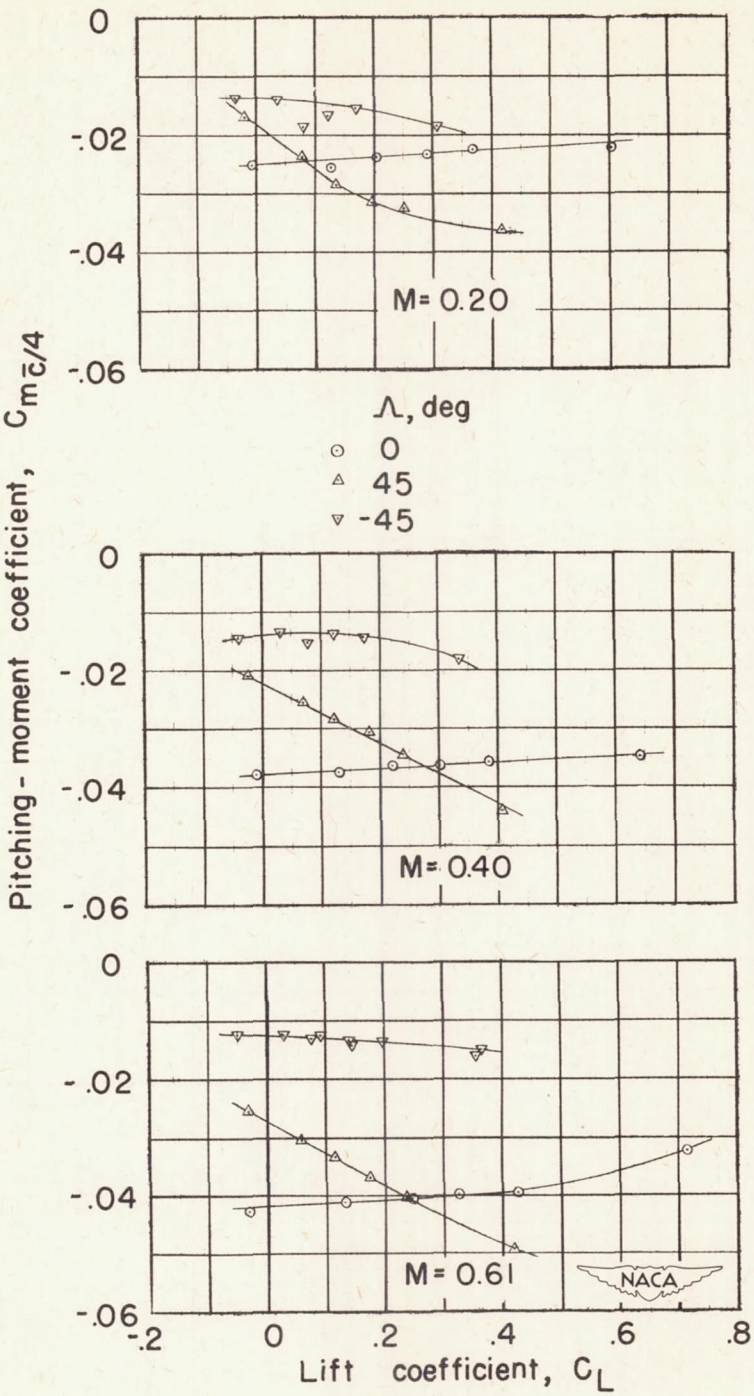


Figure 23.—Variation of pitching-moment coefficient with lift coefficient for wing-nacelle combination.

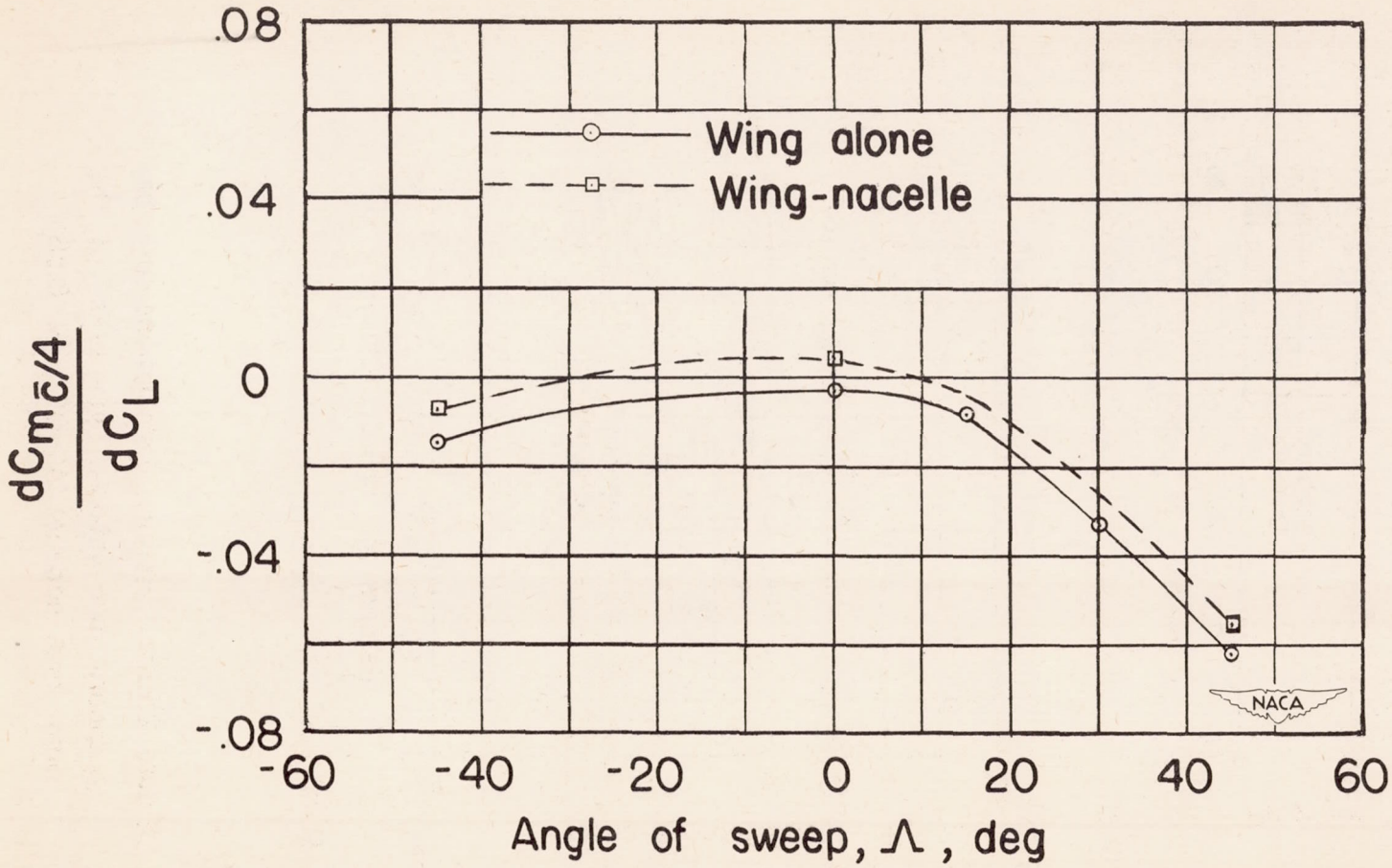
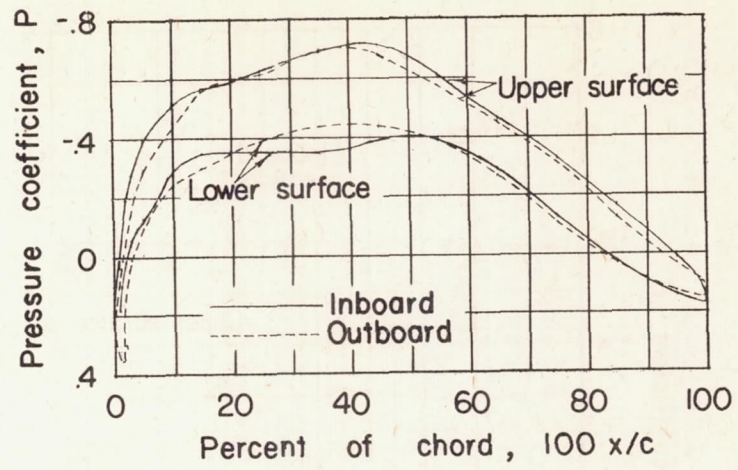
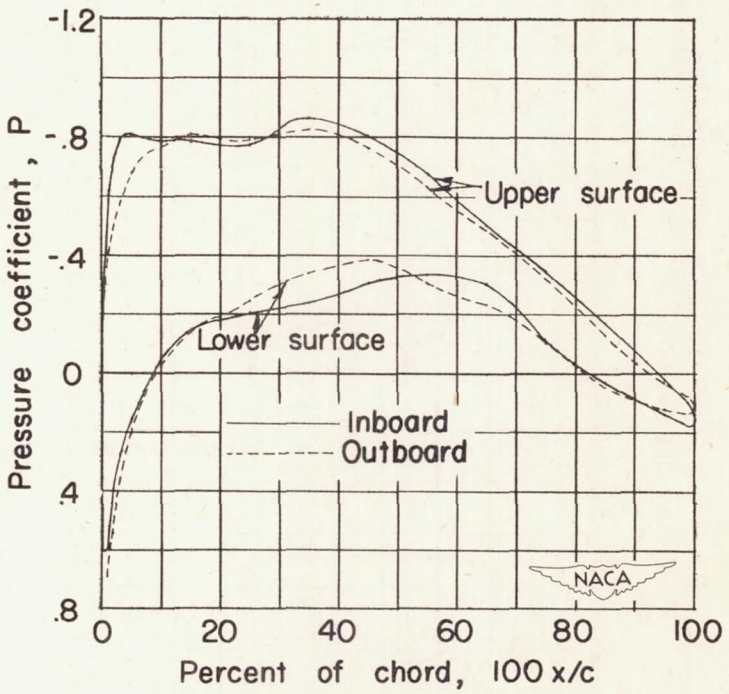


Figure 24.—Variation of $\frac{dC_{m_{\bar{c}/4}}}{dC_L}$ with angle of sweep. M=0.61.

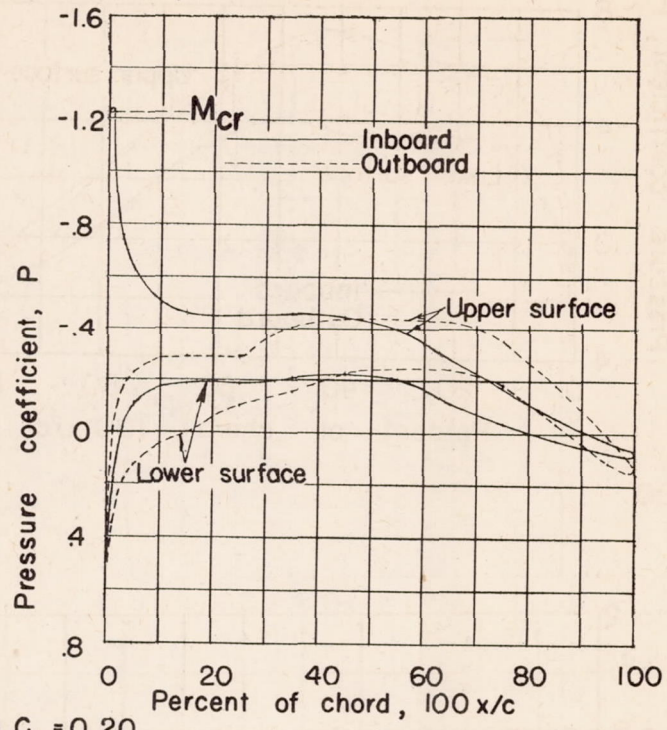


(a) $C_L = 0.20$.

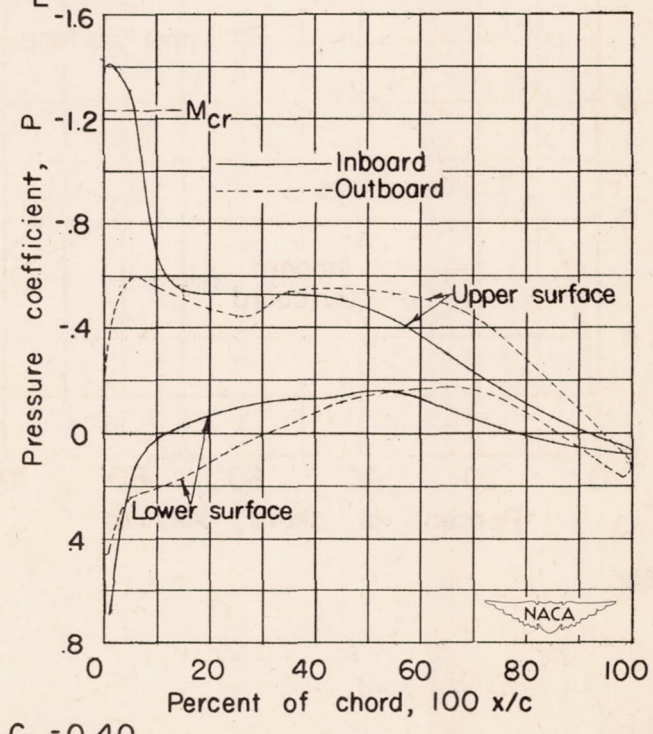


(b) $C_L = 0.40$.

Figure 25.— Pressure distributions at the outboard and inboard junctures of the wing and nacelle. $\Lambda = 0°$; $M = 0.58$.

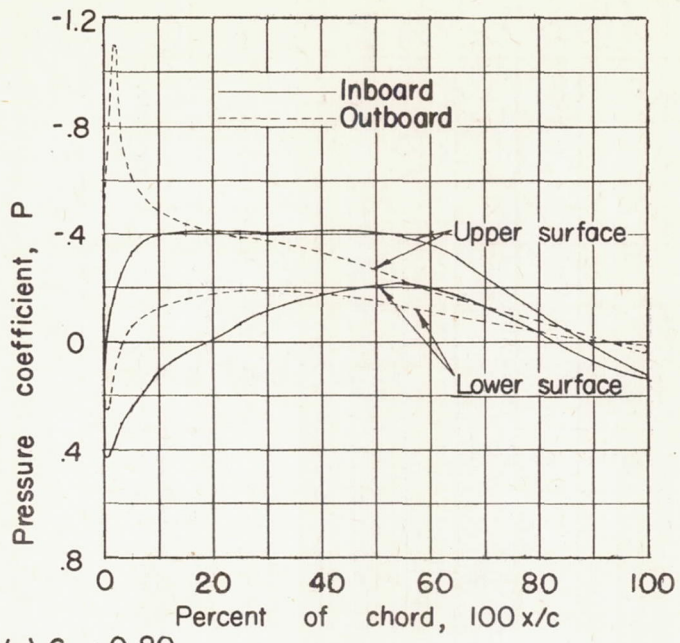


(a) $C_L = 0.20$.

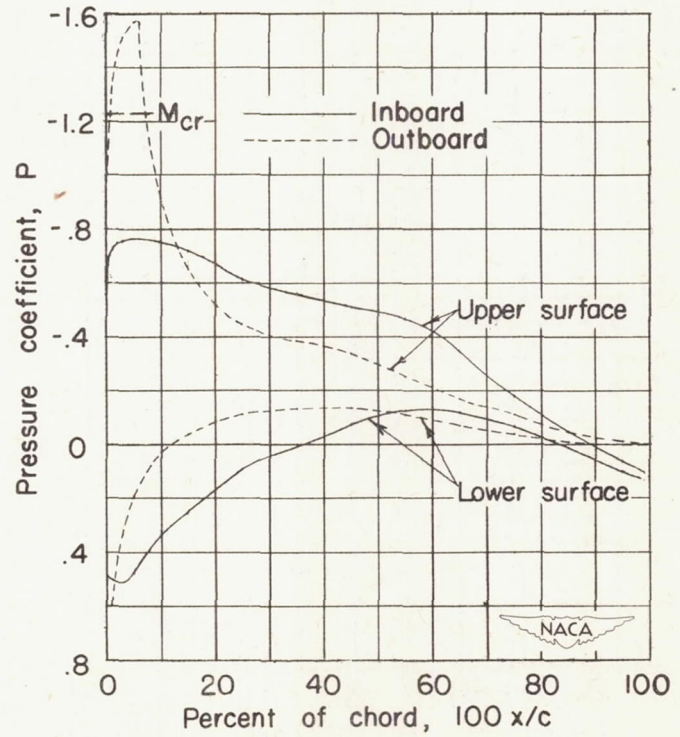


(b) $C_L = 0.40$.

Figure 26. — Pressure distributions at the outboard and inboard junctures of the wing and nacelle. $\Lambda = 45°$; $M = 0.61$.



(a) $C_L = 0.20$.



(b) $C_L = 0.40$.

Figure 27.— Pressure distributions at the outboard and inboard junctures of the wing and nacelle. $\Lambda = -45°$; $M = 0.61$.

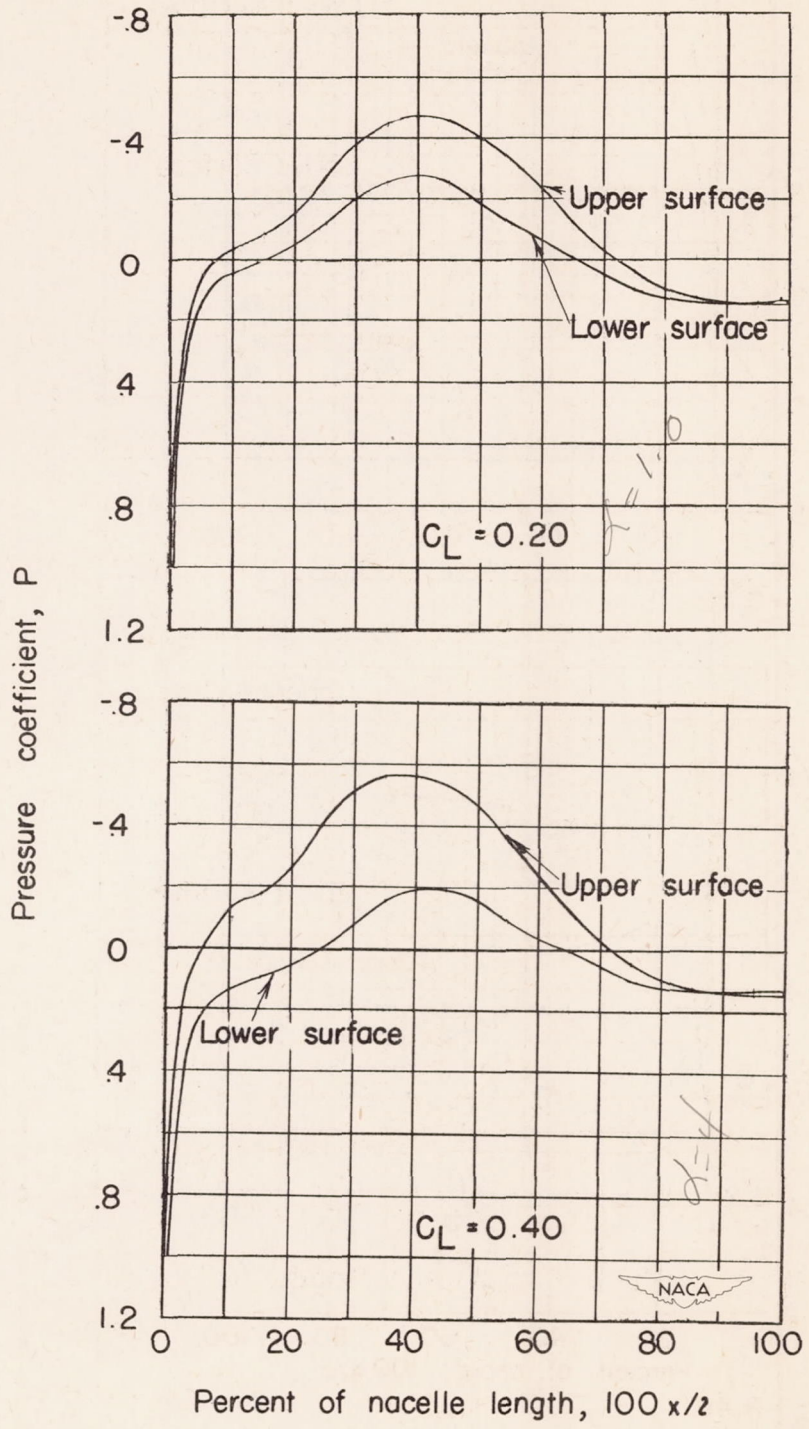


Figure 28.—Pressure distributions over the nacelle.

$\Lambda = 0°$; $M = 0.58$.

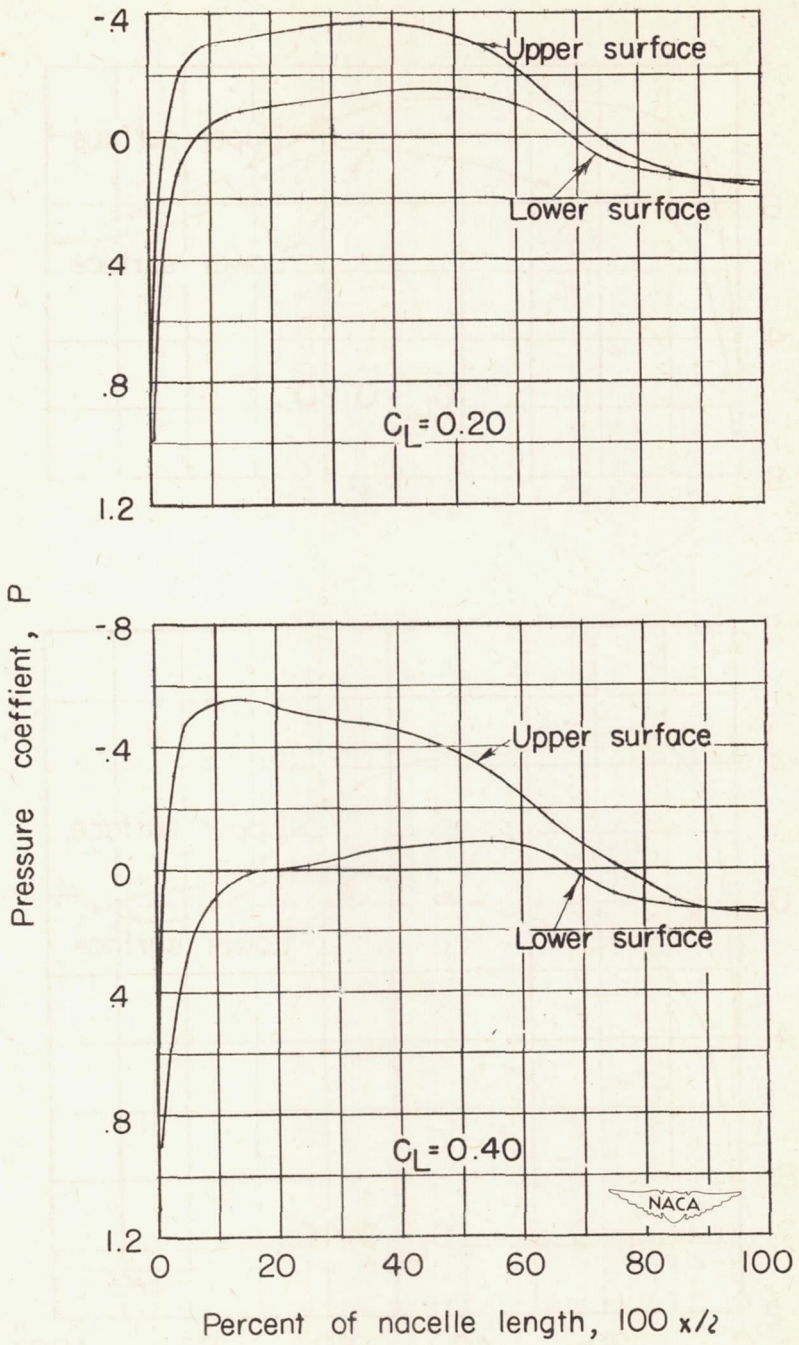


Figure 29.—Pressure distributions over the nacelle.

$\Lambda = 45°$; $M = 0.61$.

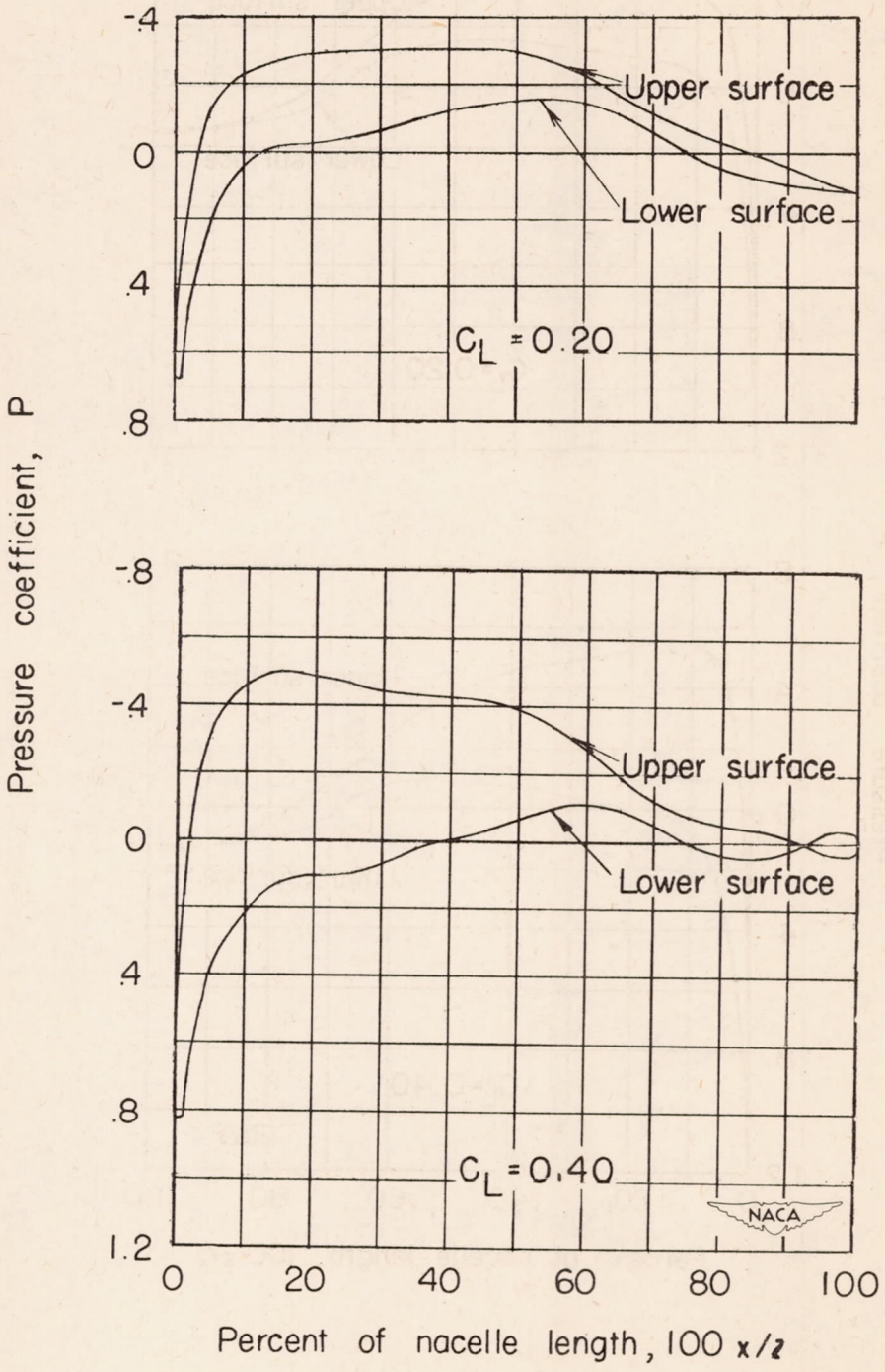


Figure 30.—Pressure distributions over the nacelle.

$\Lambda = -45°$; $M = 0.61$.

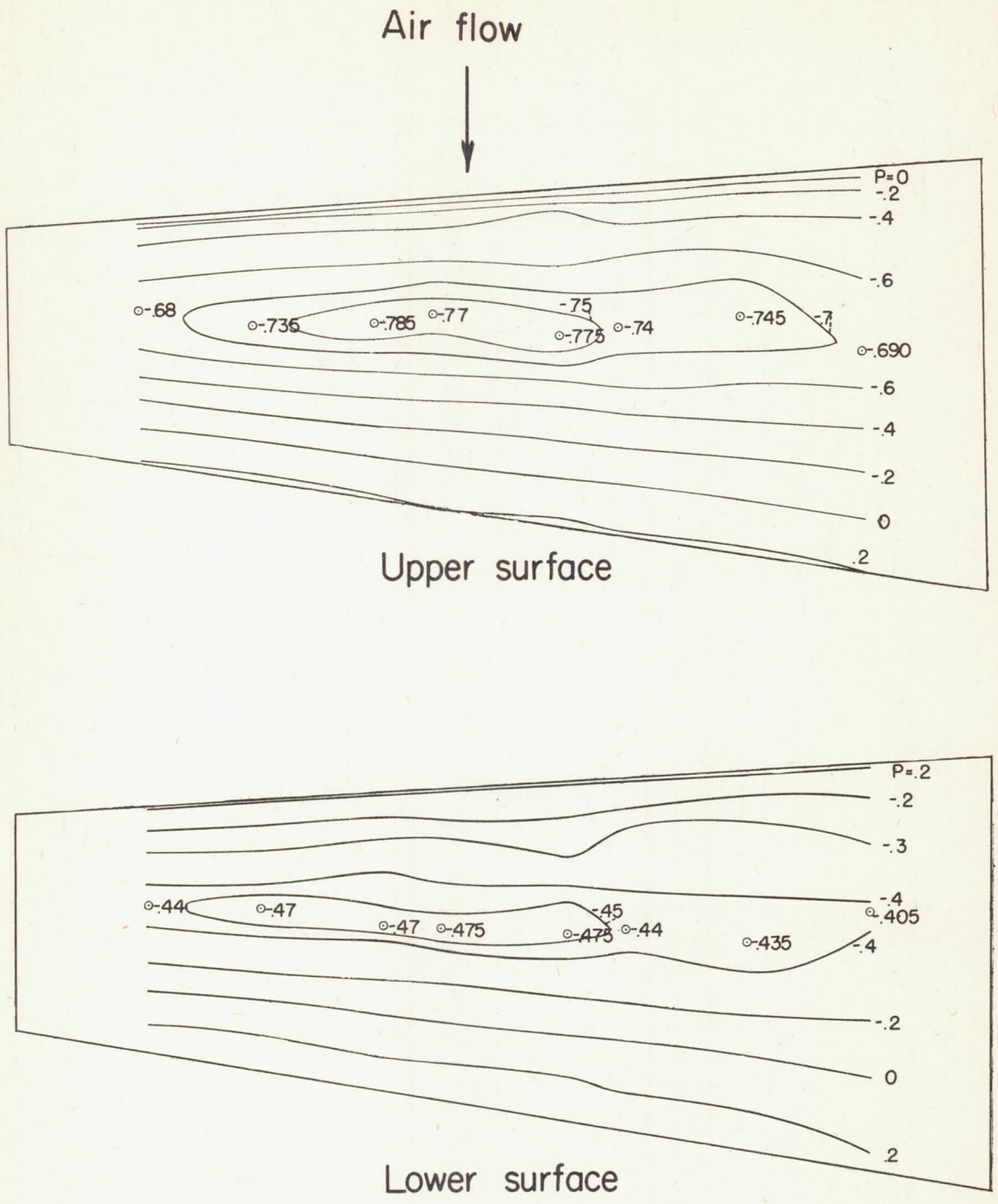


Figure 31.— Pressure contours for the wing alone. $\Lambda = 0°$; $C_L = 0.20$; $M = 0.61$.

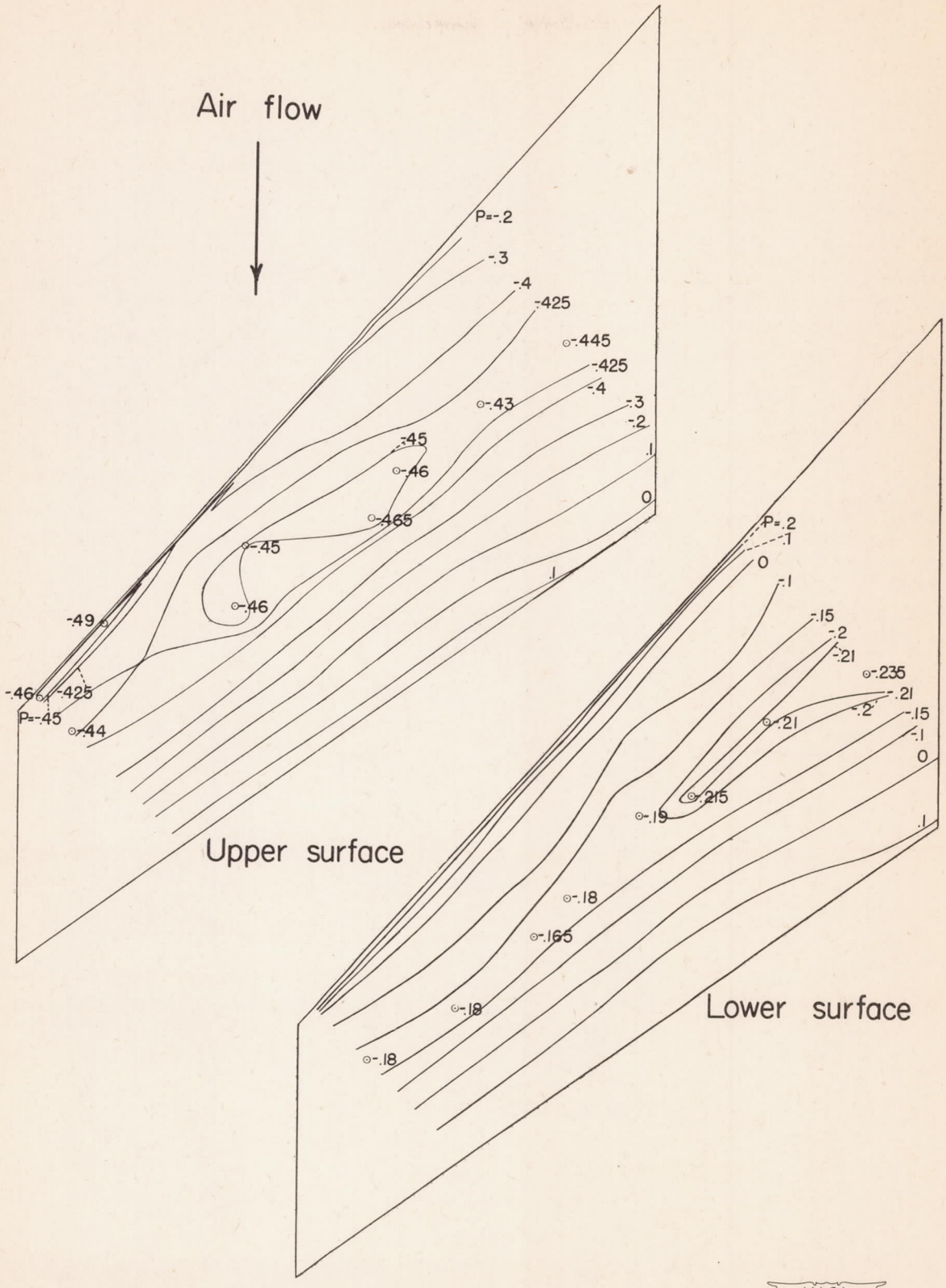


Figure 32.—Pressure contours for the wing alone. $\Lambda = 45°$; $C_L = 0.20$; $M = 0.61$.

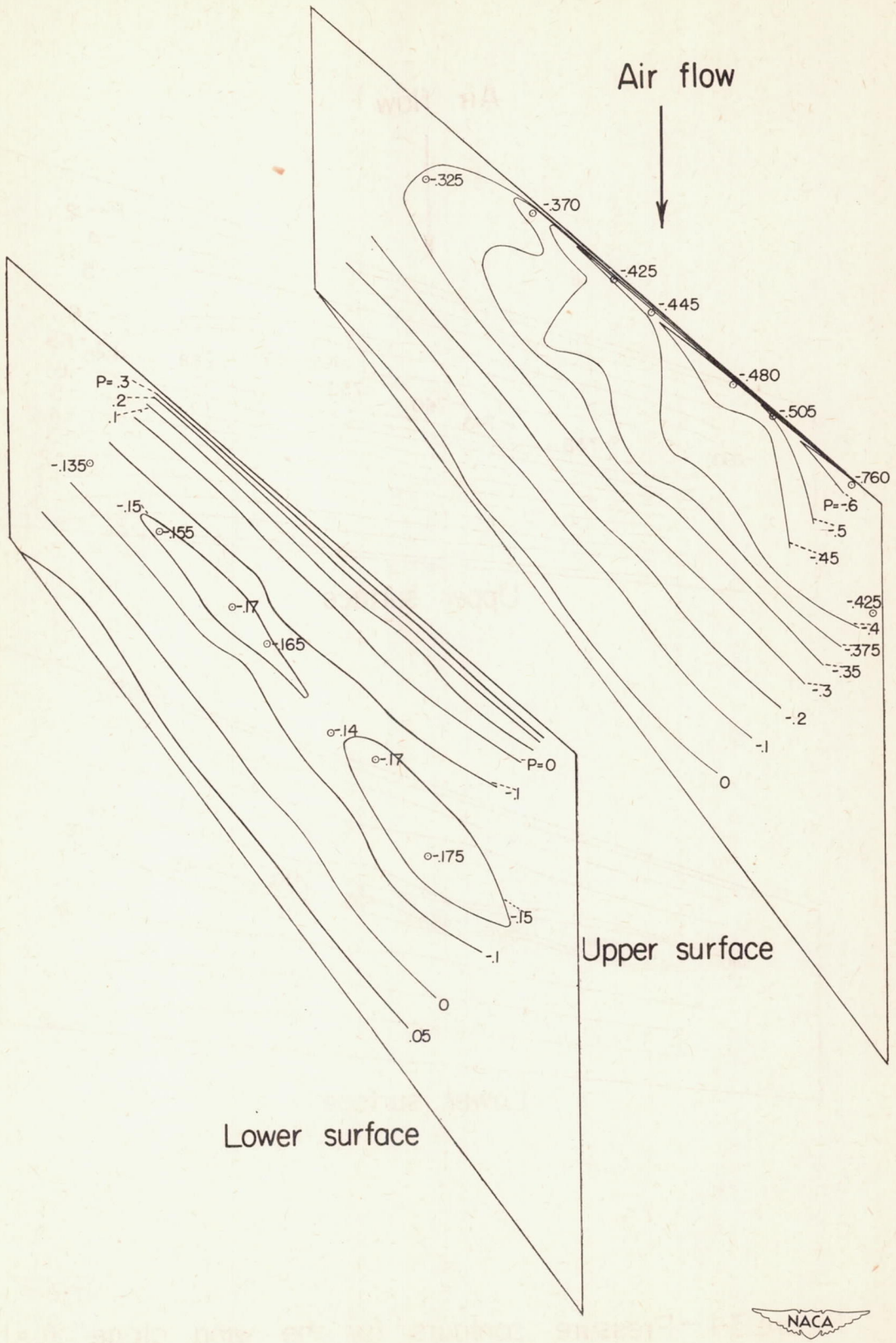


Figure 33.—Pressure contours for the wing alone. $\Lambda = -45°$; $C_L = 0.20$; $M = 0.61$.

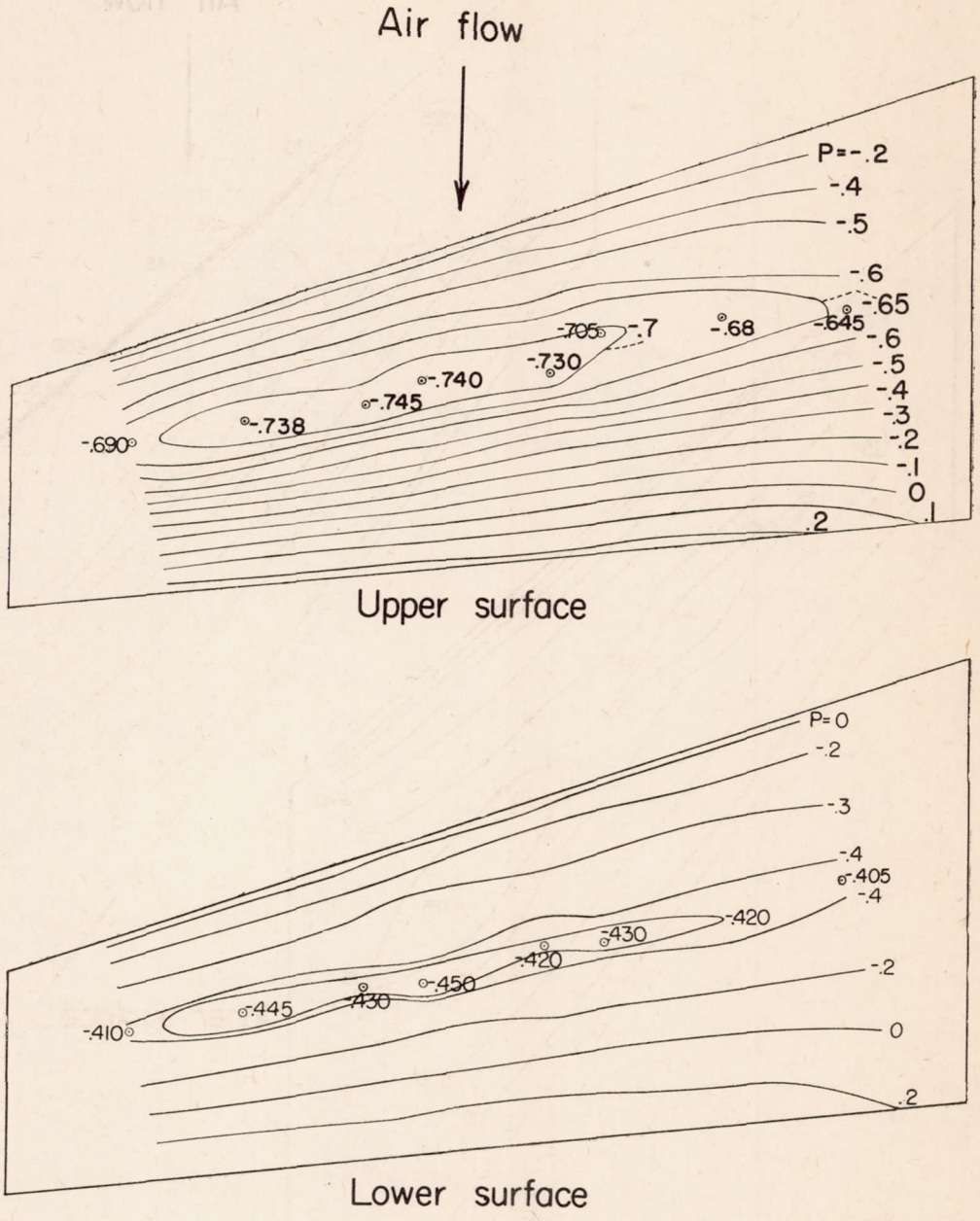


Figure 34.—Pressure contours for the wing alone. $\Lambda = 15°$; $C_L = 0.20$; $M = 0.61$.

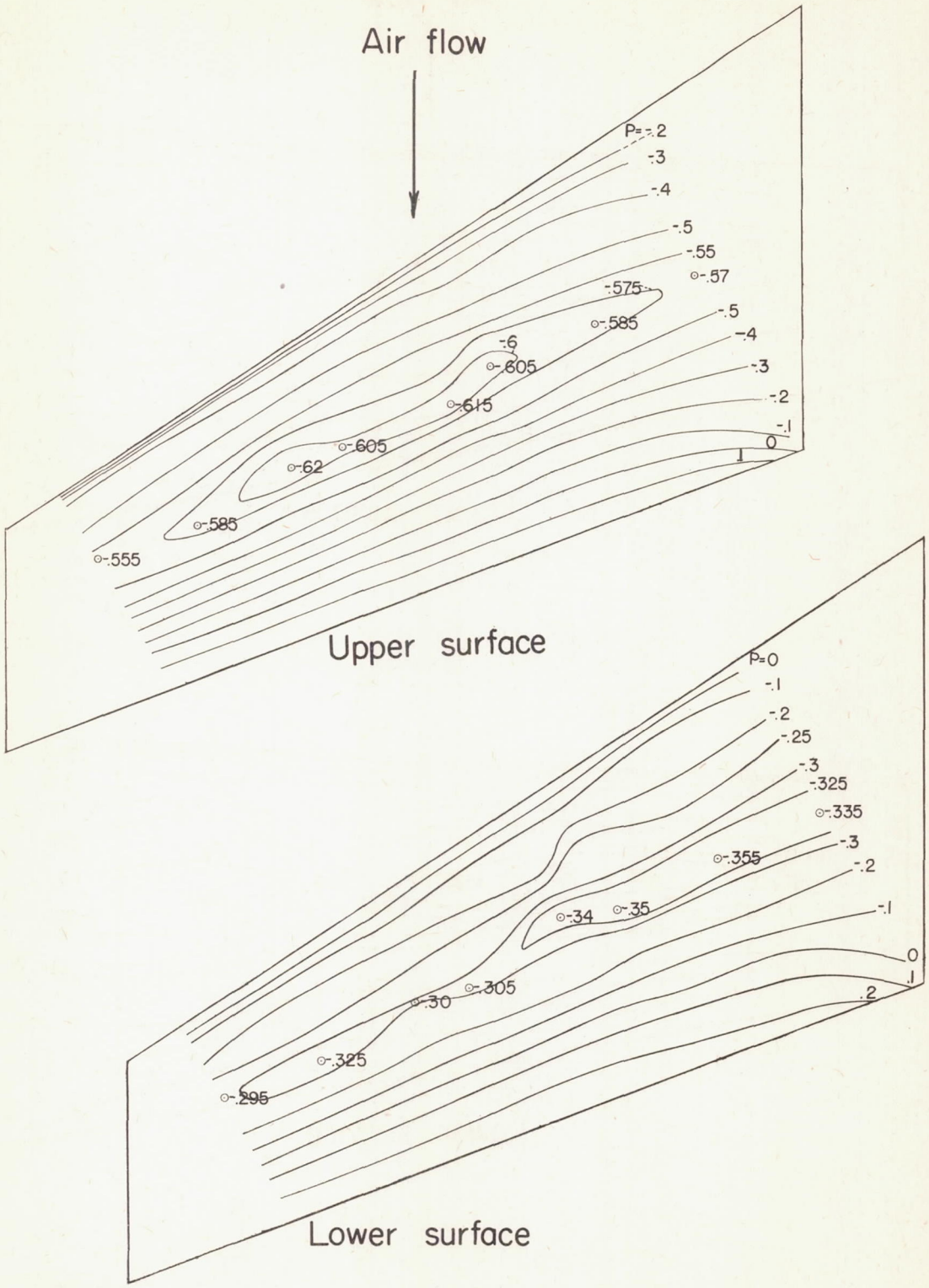


Figure 35.—Pressure contours for the wing alone. $\Lambda = 30°$; $C_L = 0.20$; $M = 0.61$.

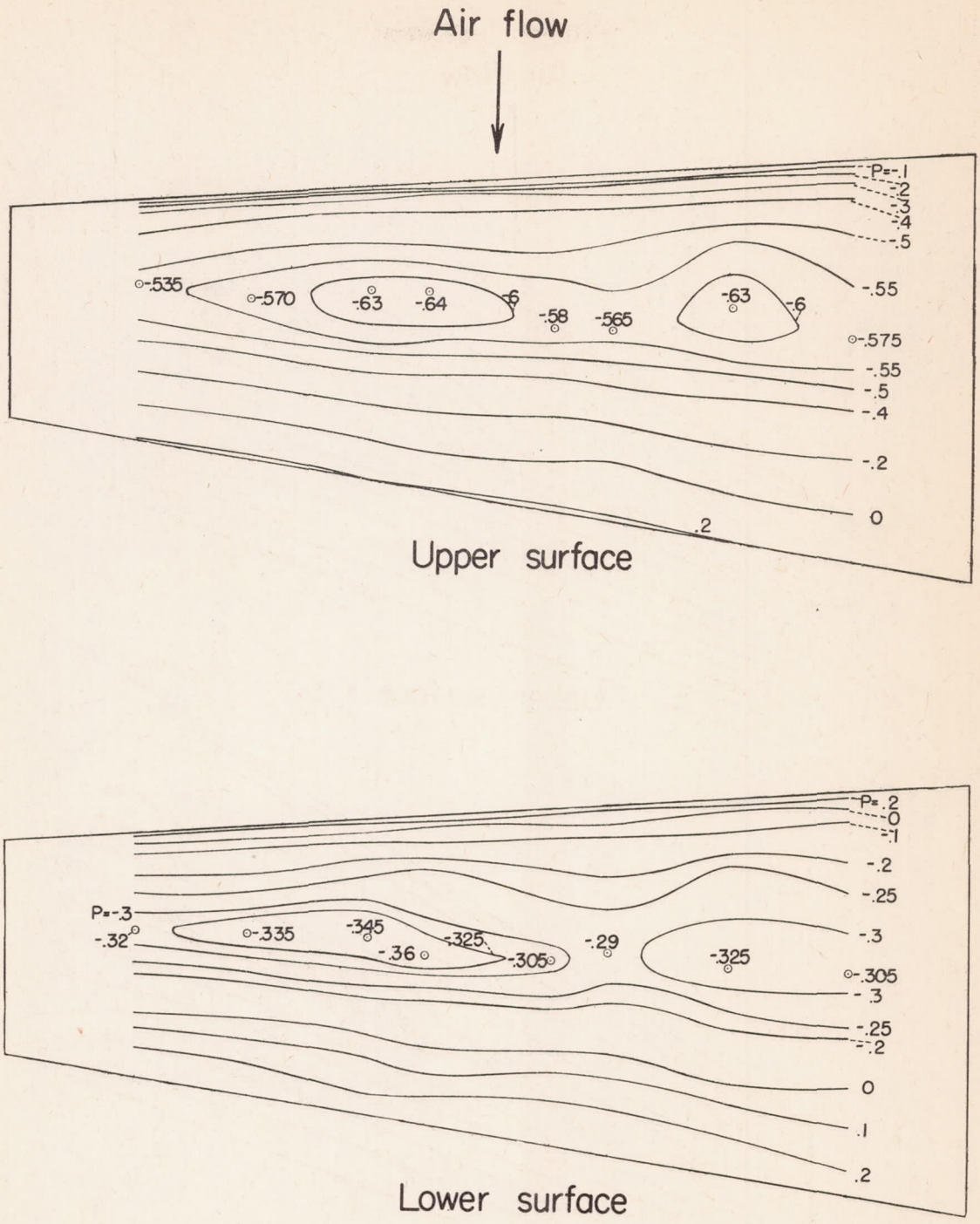


Figure 36.—Pressure contours for the wing alone. $\Lambda = 0°$; $C_L = 0.20$; $M = 0.20$.

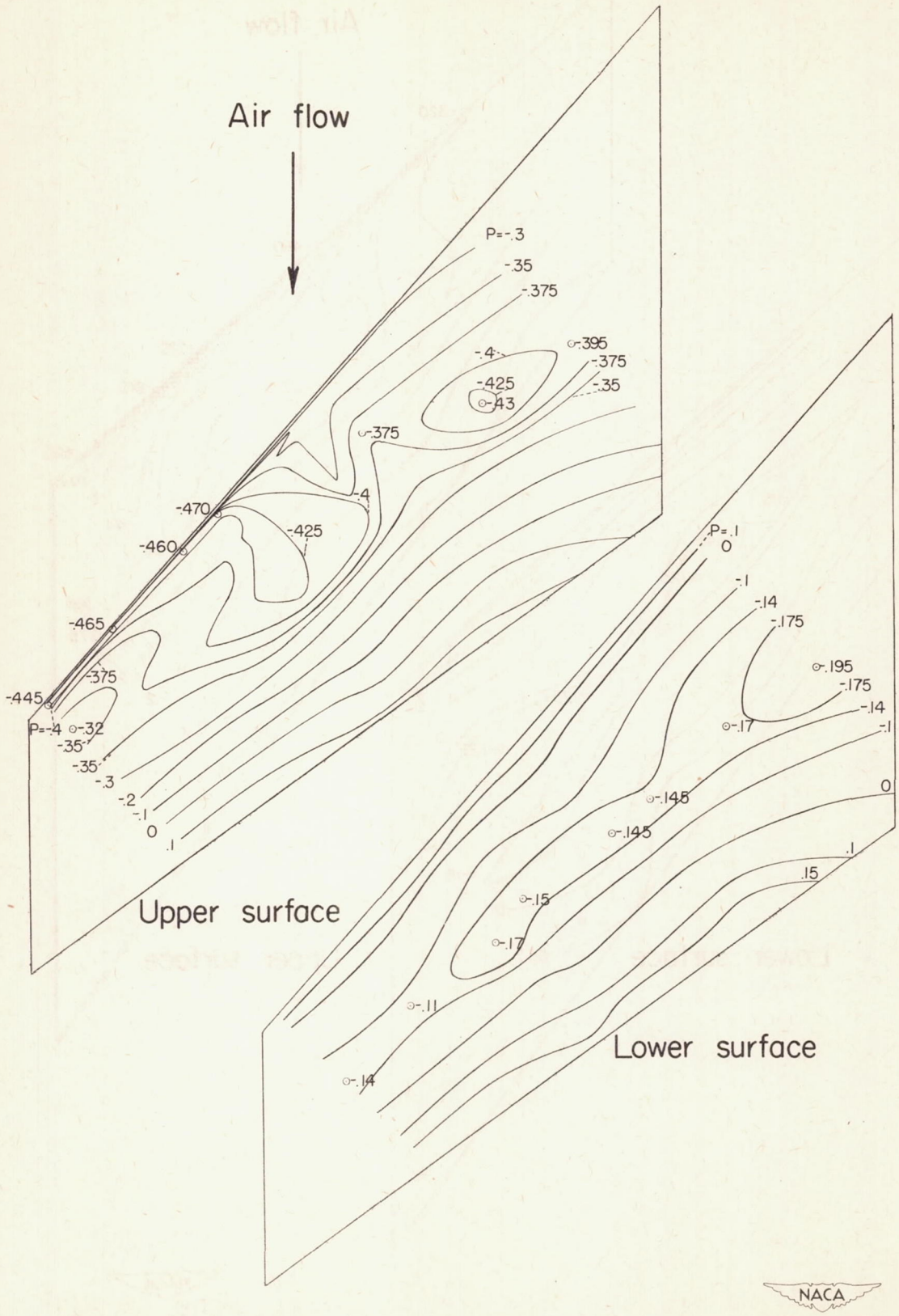


Figure 37.- Pressure contours for the wing alone. $\Lambda = 45°$; $C_L = 0.20$; $M = 0.20$.

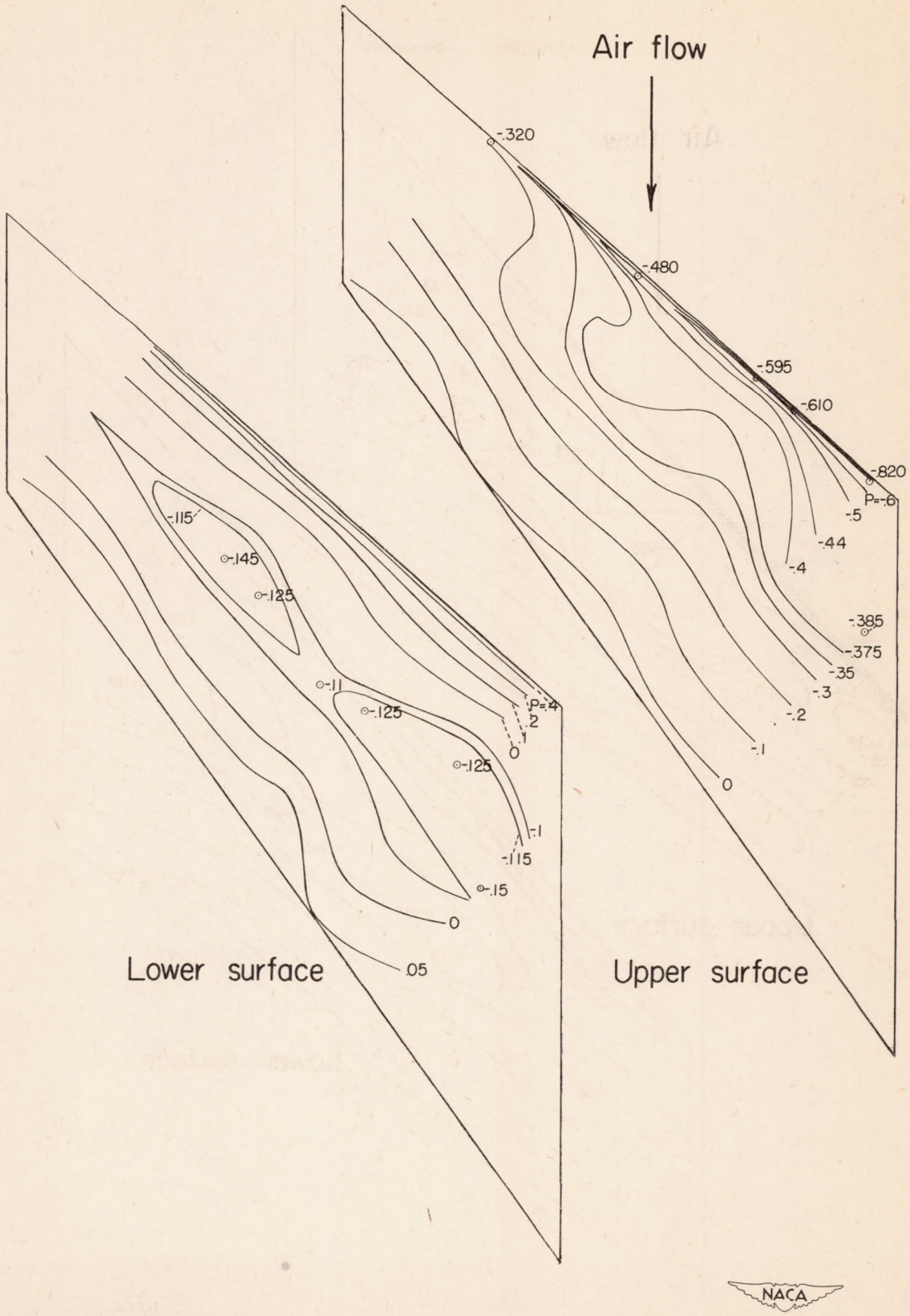


Figure 38.— Pressure contours for the wing alone. $\Lambda = -45°$; $C_L = 0.20$; $M = 0.20$.

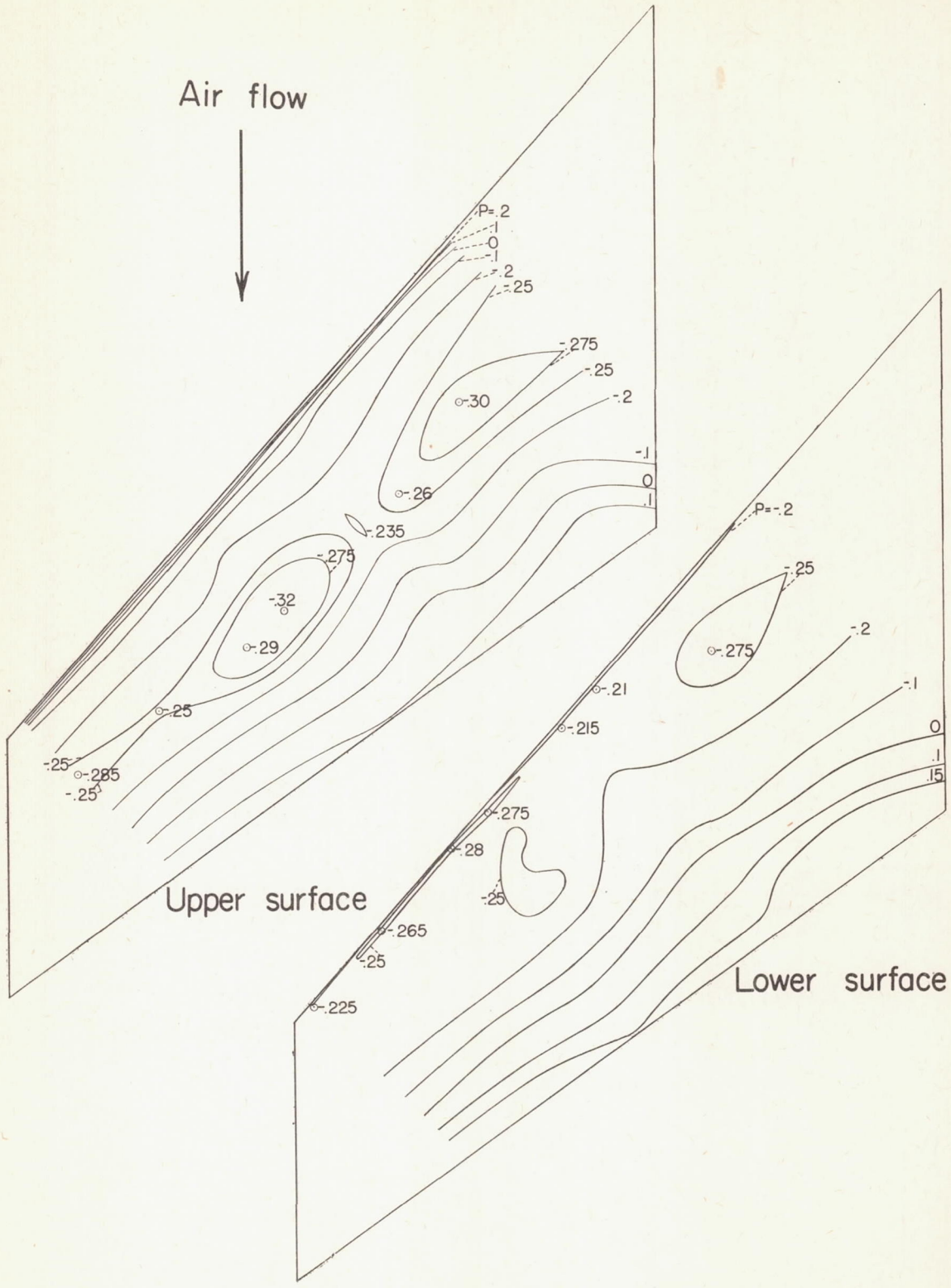


Figure 39.—Pressure contours for the wing alone. $\Lambda = 45°$; $C_L = 0$; $M = 0.20$.

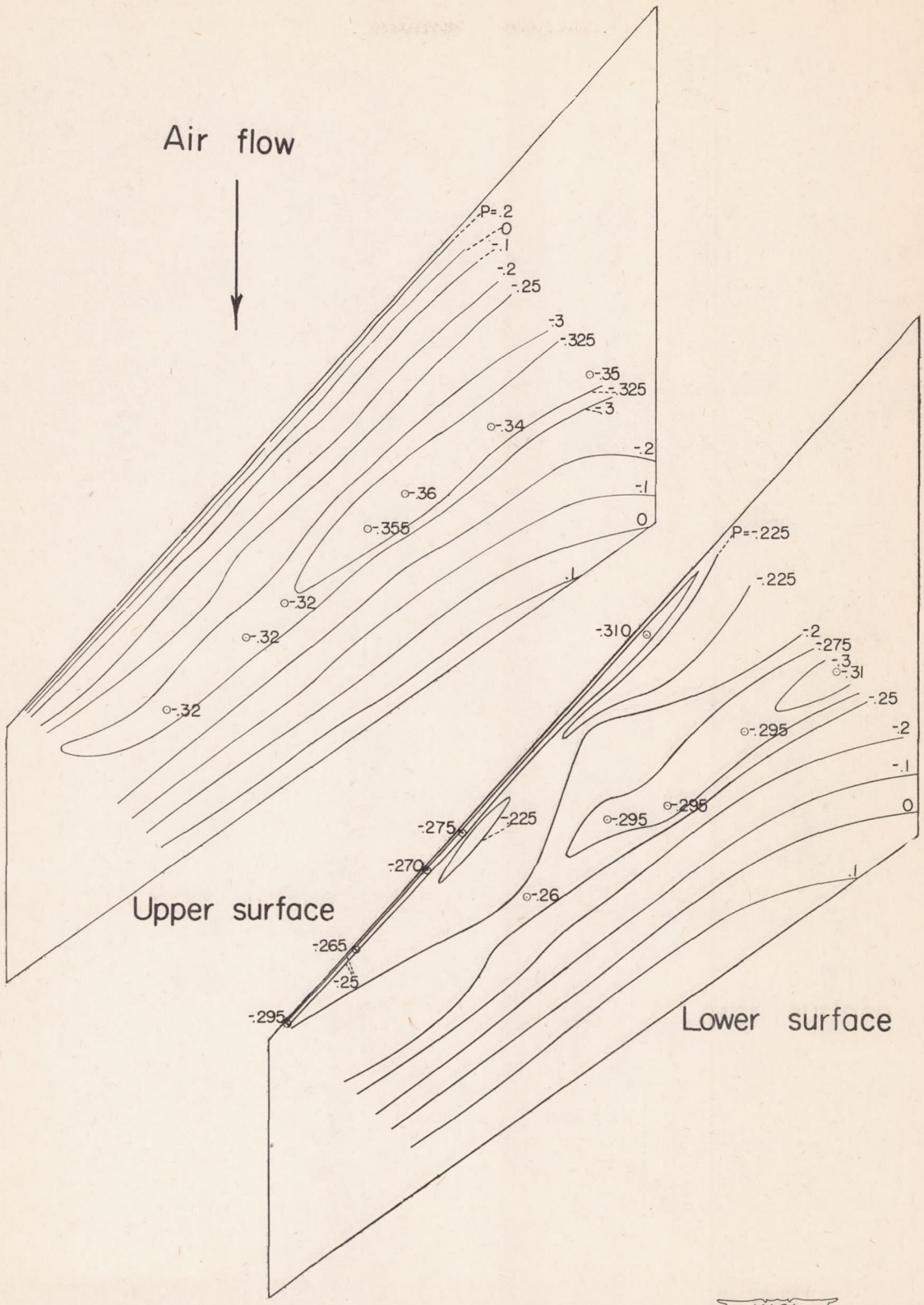
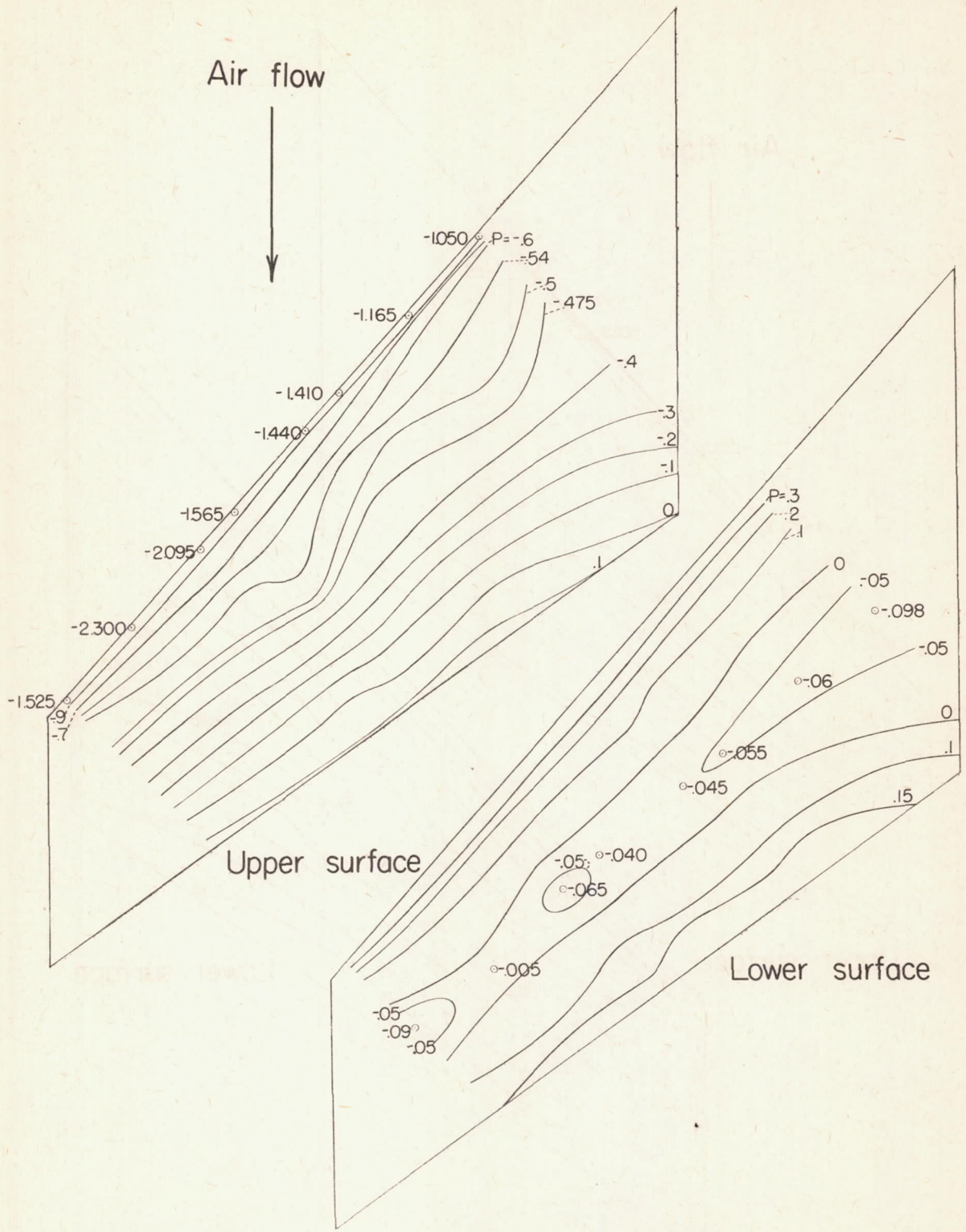


Figure 40 — Pressure contours for the wing alone. $\Lambda = 45°$; $C_L = 0$; $M = 0.61$.



NACA

Figure 41.- Pressure contours for the wing alone. $\Lambda = 45$; $C_L = 0.40$; $M = 0.20$.

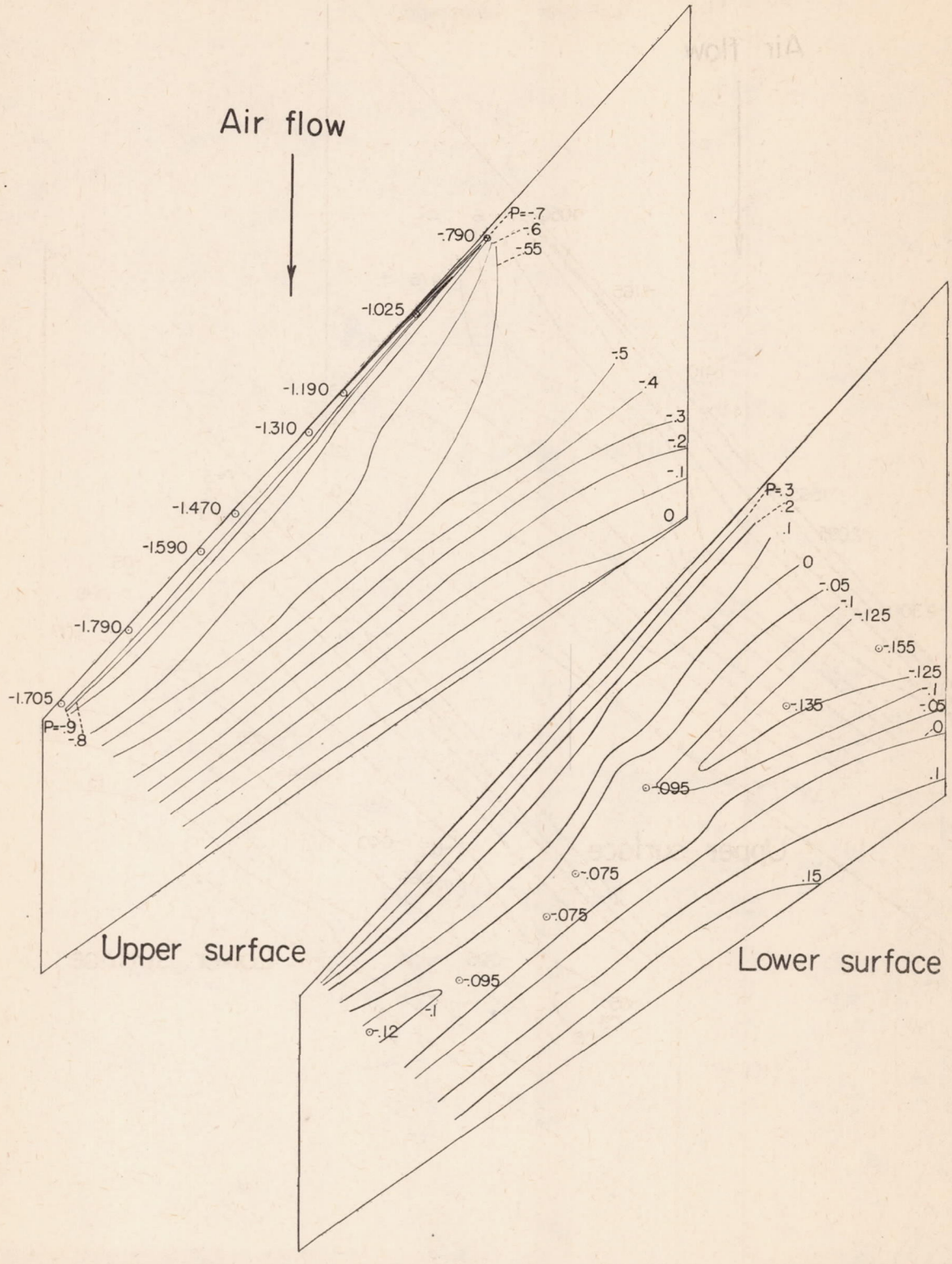


Figure 42.— Pressure contours for the wing alone. $\Lambda = 45°$; $C_L = 0.40$; $M = 0.61$.

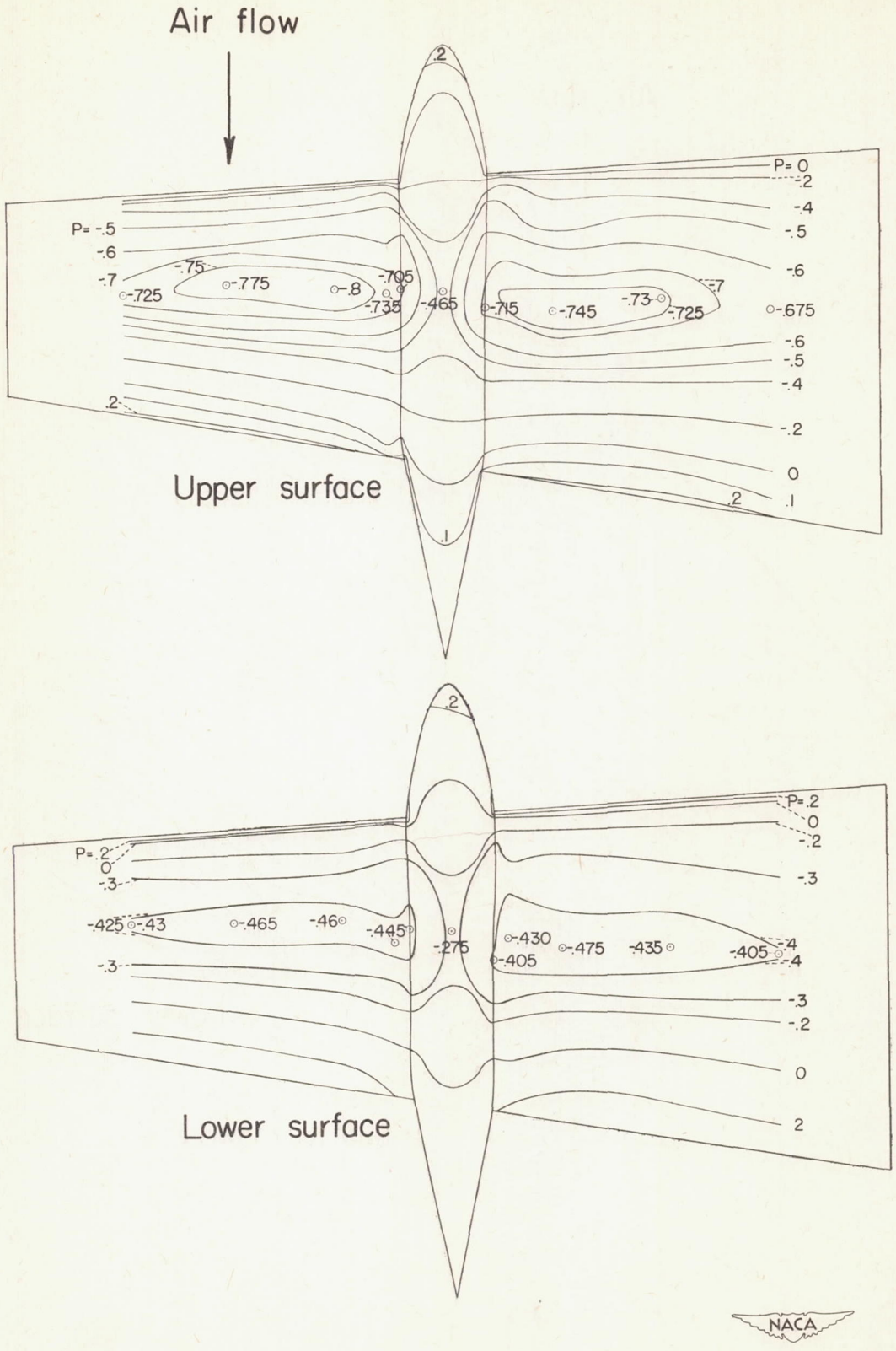


Figure 43.–Pressure contours for the wing-nacelle combination.

$\Lambda = 0°$; $C_L = 0.20$; $M = 0.58$.

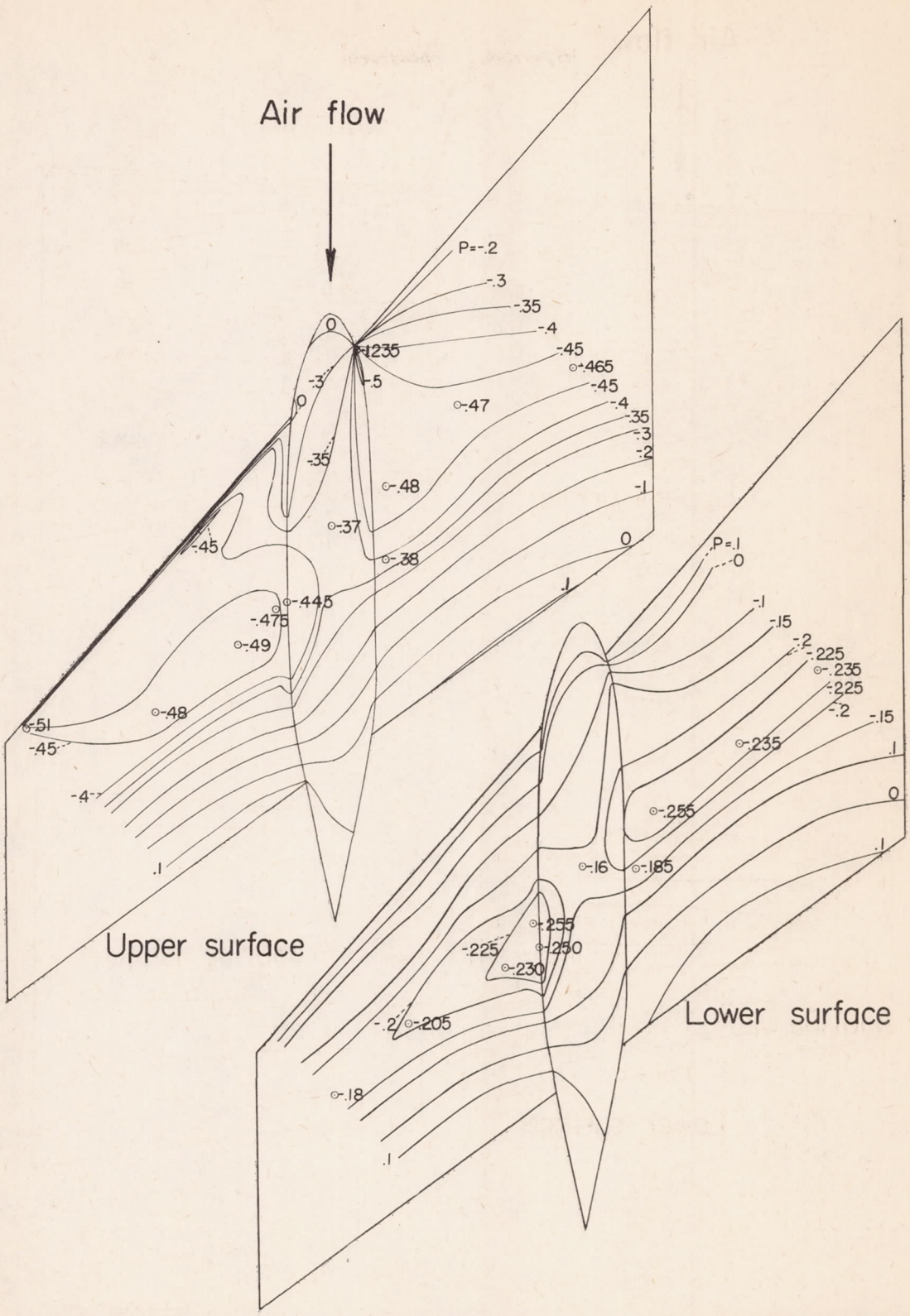


Figure 44.— Pressure contours for the wing-nacelle combination.

$\Lambda = 45°$; $C_L = 0.20$; $M = 0.61$.

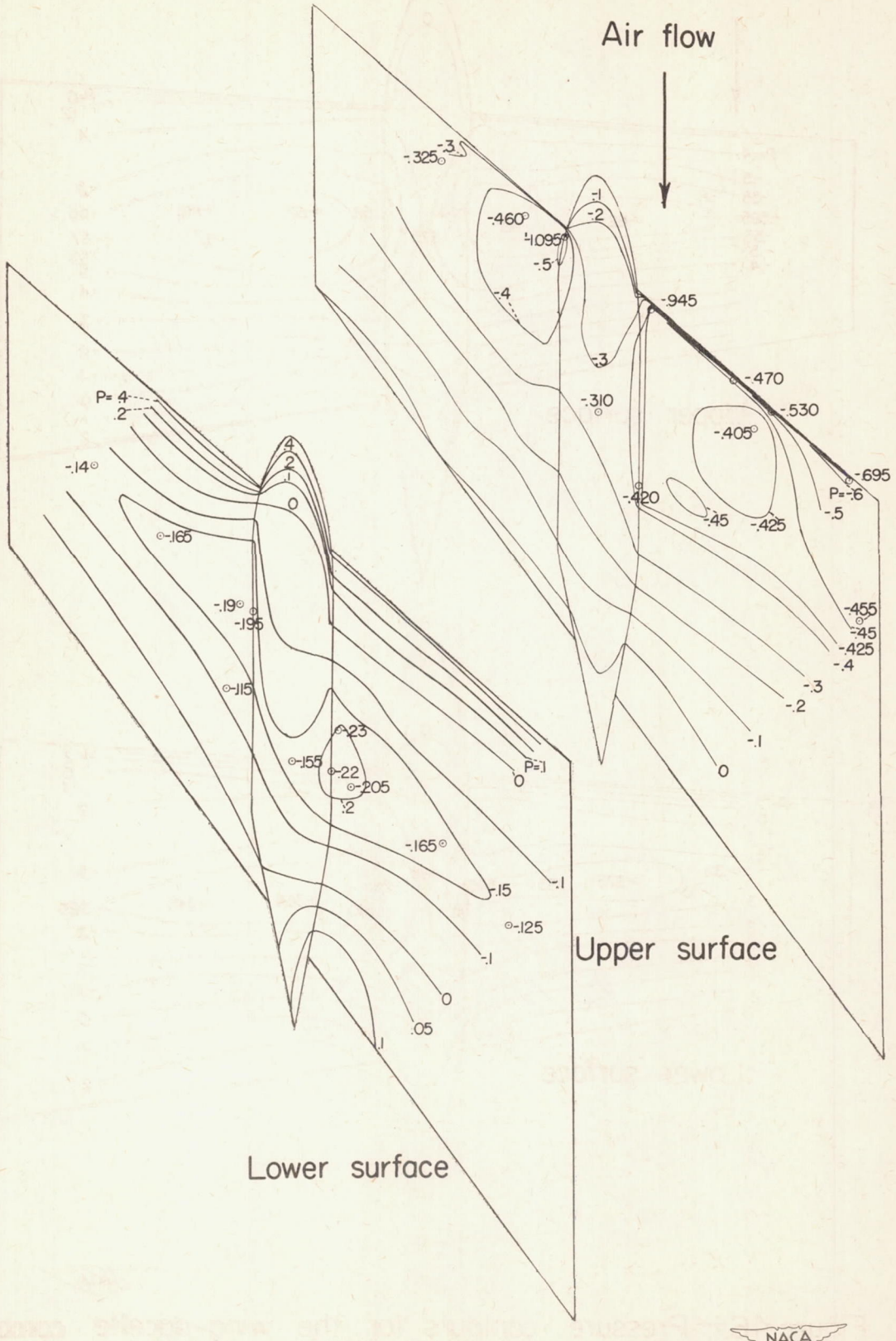


Figure 45.—Pressure contours for the wing-nacelle combination.

$\Lambda = -45°; C_L = 0.20$; $M = 0.61$.

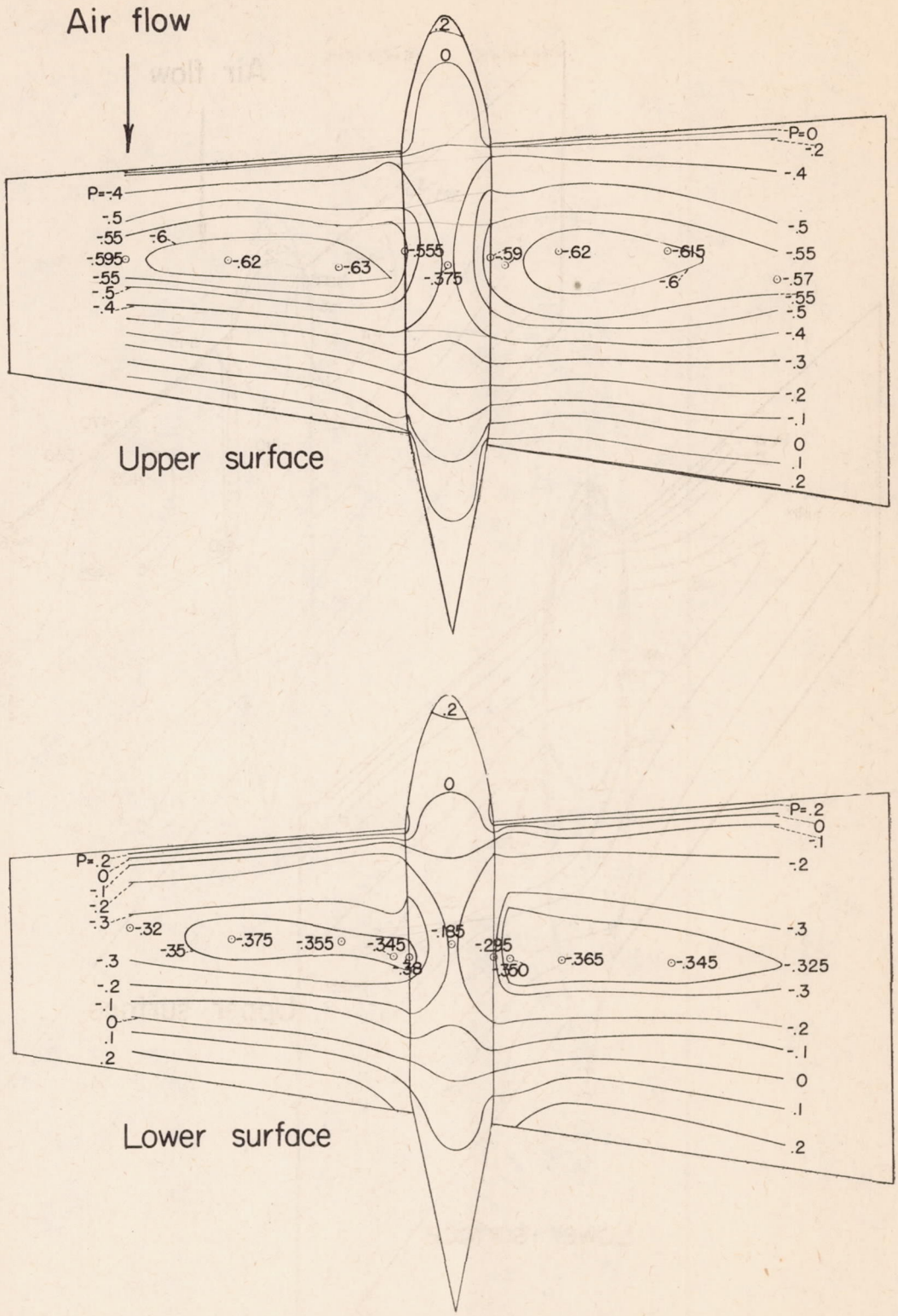


Figure 46.— Pressure contours for the wing-nacelle combination.

$\Lambda = 0°$; $C_L = 0.20$; $M = 0.20$.

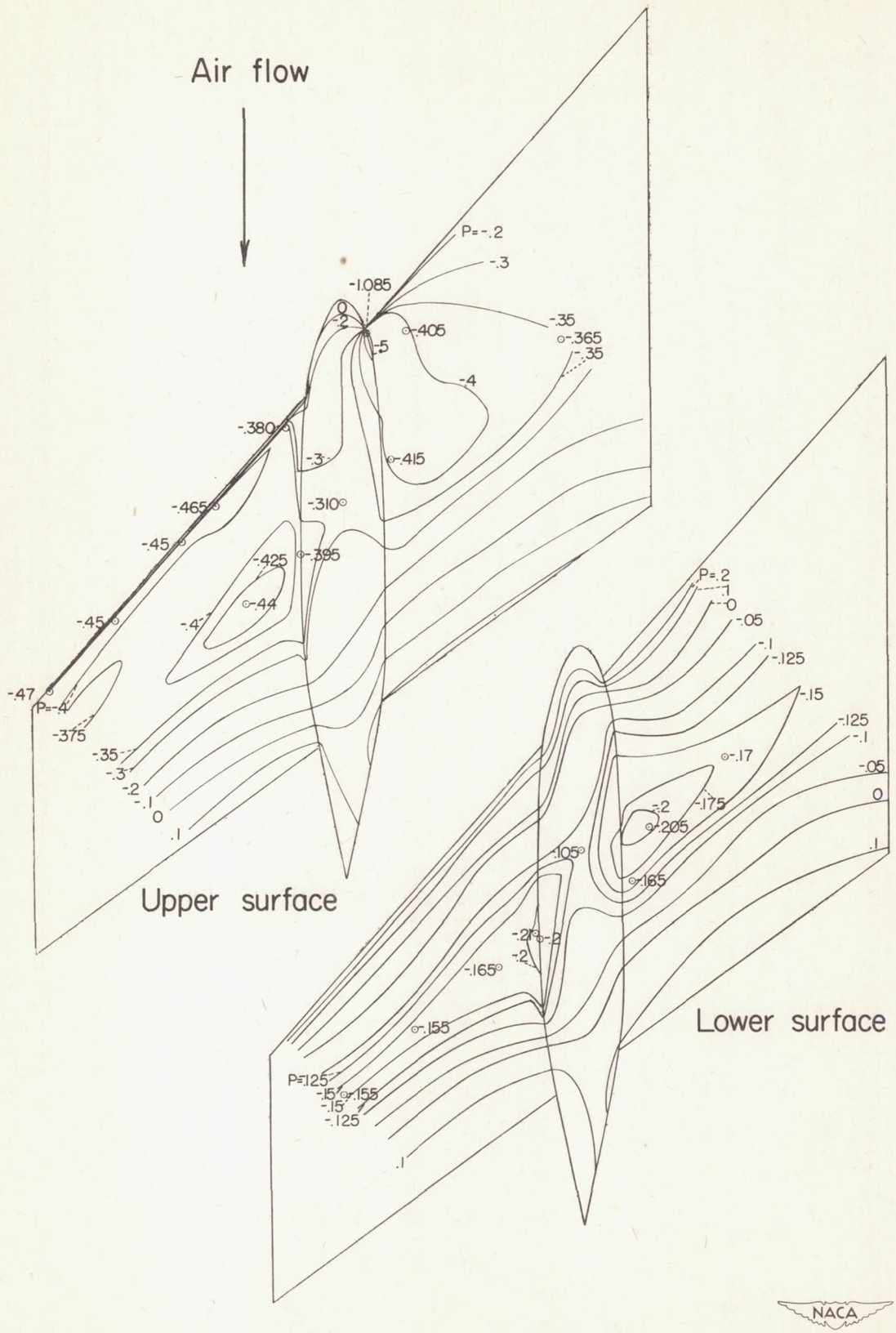


Figure 47.—Pressure contours for the wing-nacelle combination.

$\Lambda = 45°$; $C_L = 0.20$; $M = 0.20$.

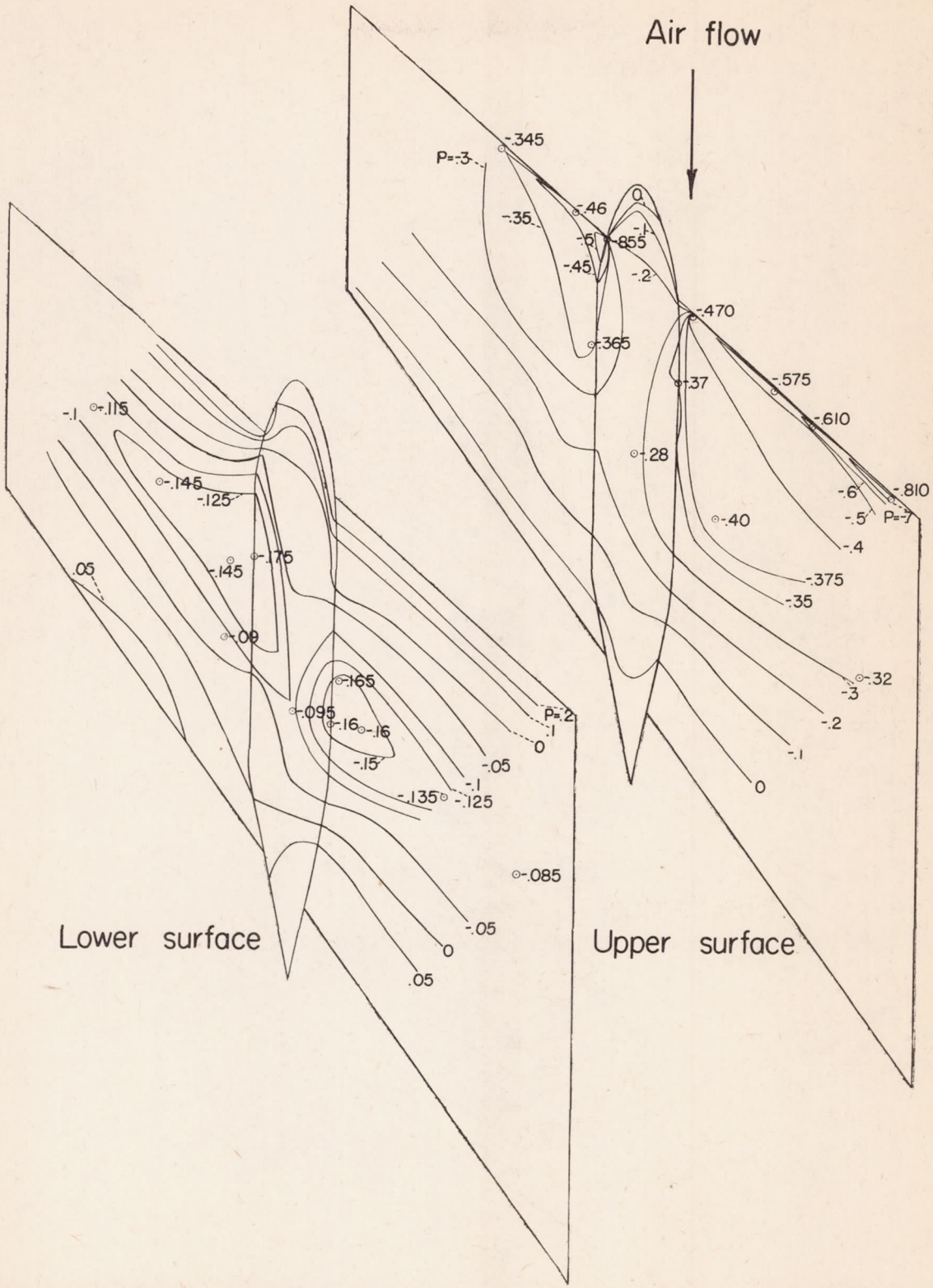


Figure 48.—Pressure contours for the wing-nacelle combination. $\Lambda=-45°$; $C_L = 0.20$; $M = 0.20$.

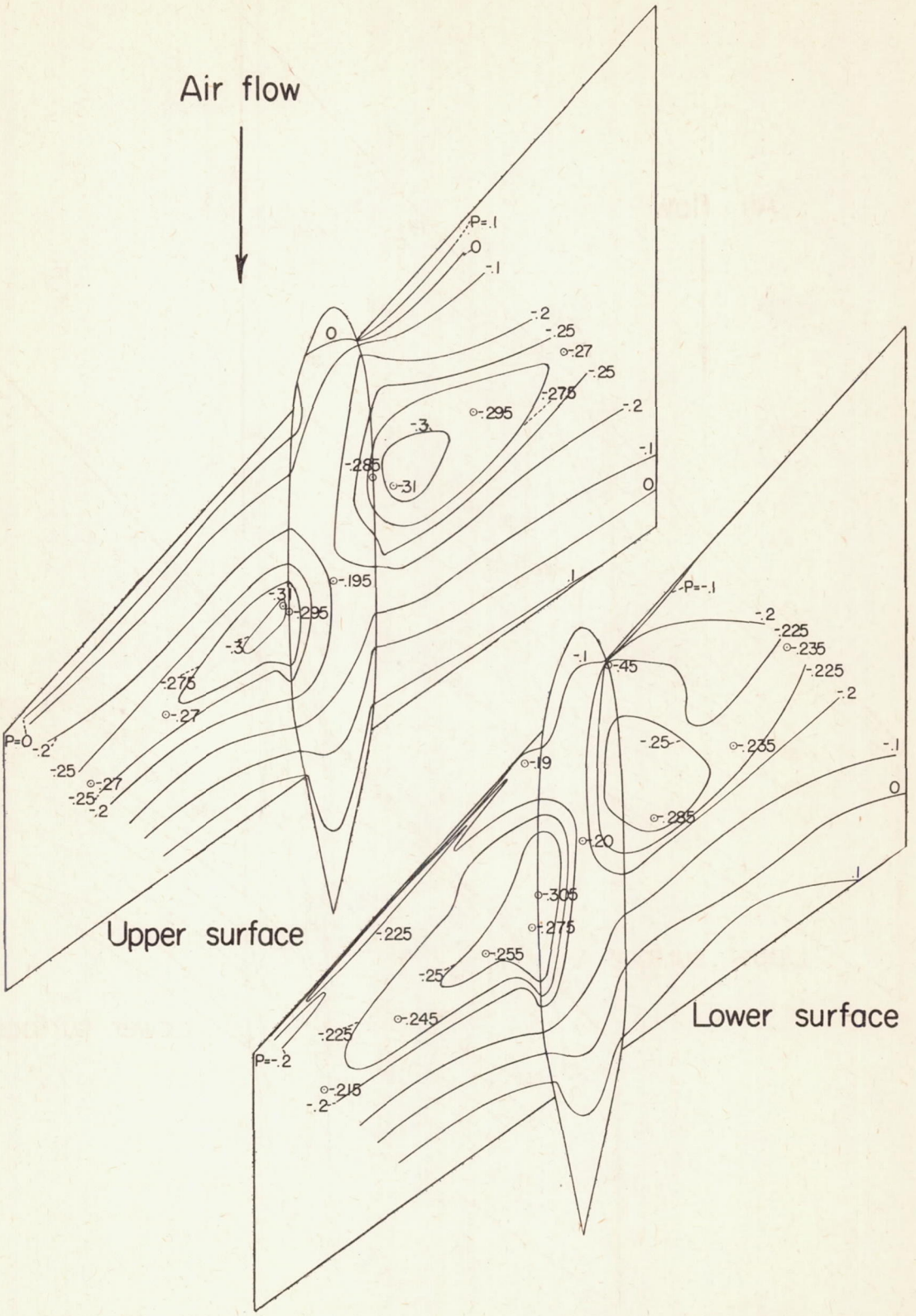


Figure 49.- Pressure contours for the wing-nacelle combination. $\Lambda = 45°$; $C_L = 0$; $M = 0.20$.

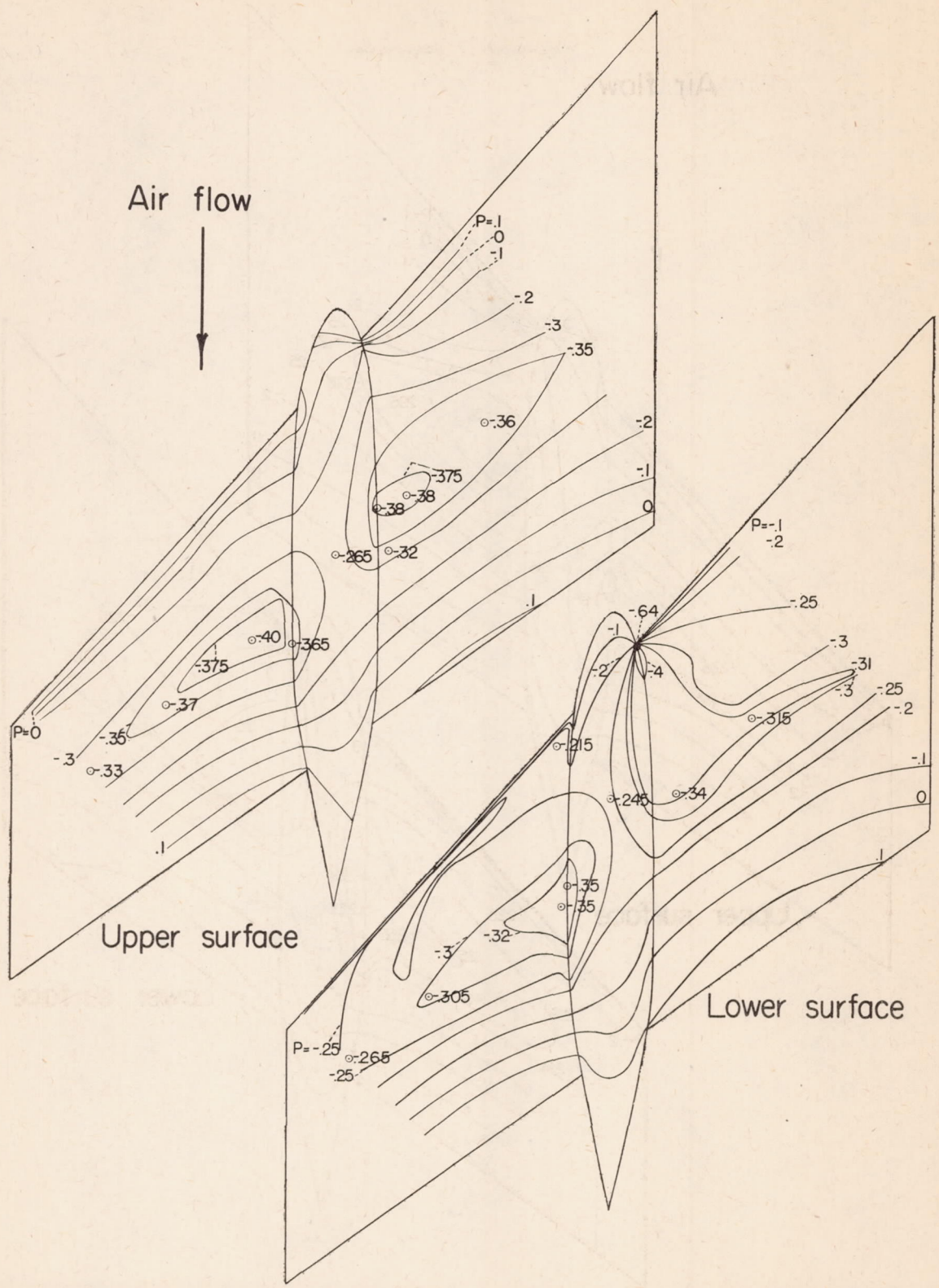


Figure 50.—Pressure contours for the wing-nacelle combination.

$\Lambda = 45°$; $C_L = 0$; $M = 0.61$.

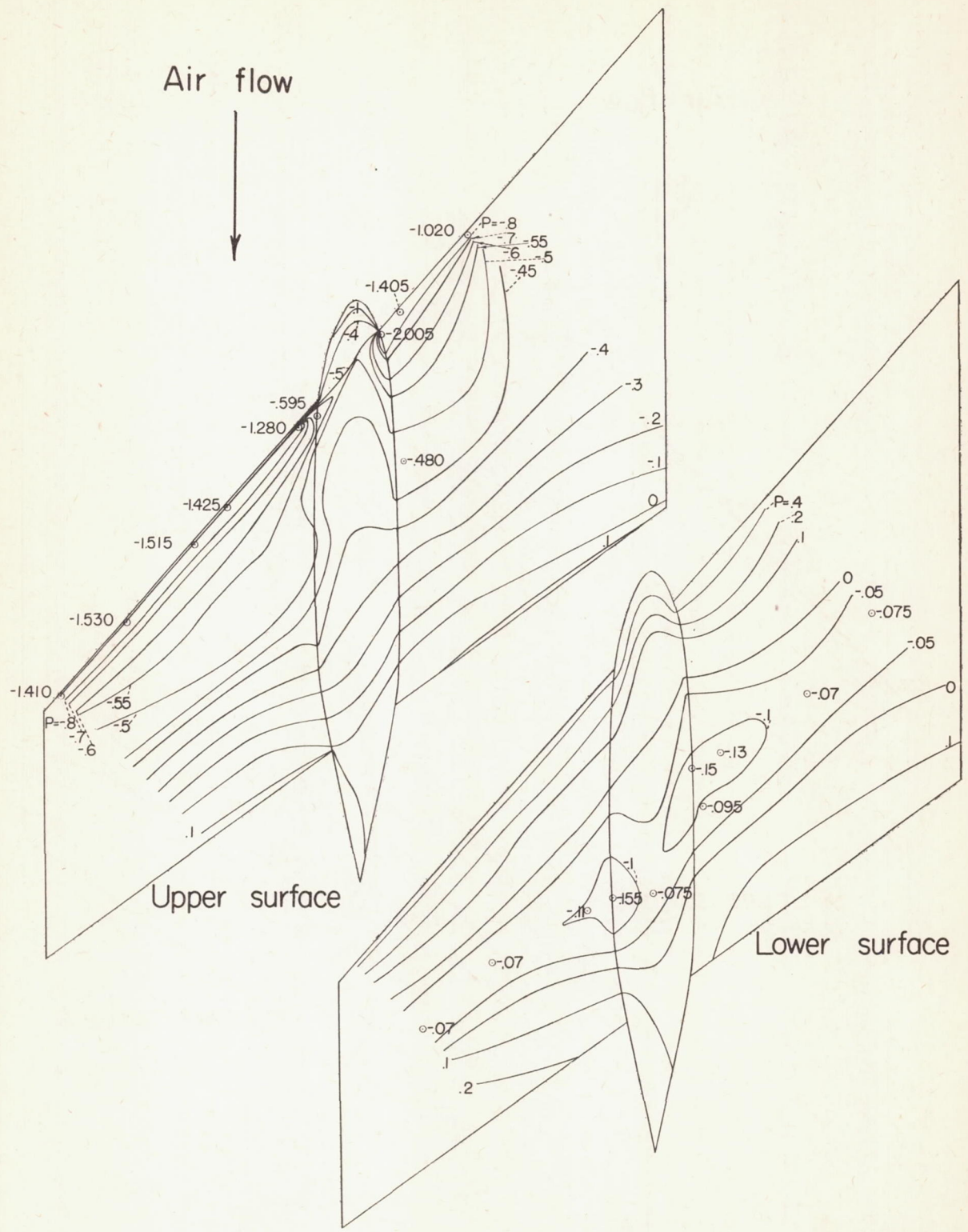


Figure 51.—Pressure contours for the wing-nacelle combination.

$\Lambda = 45°$; $C_L = 0.40$; $M = 0.20$.

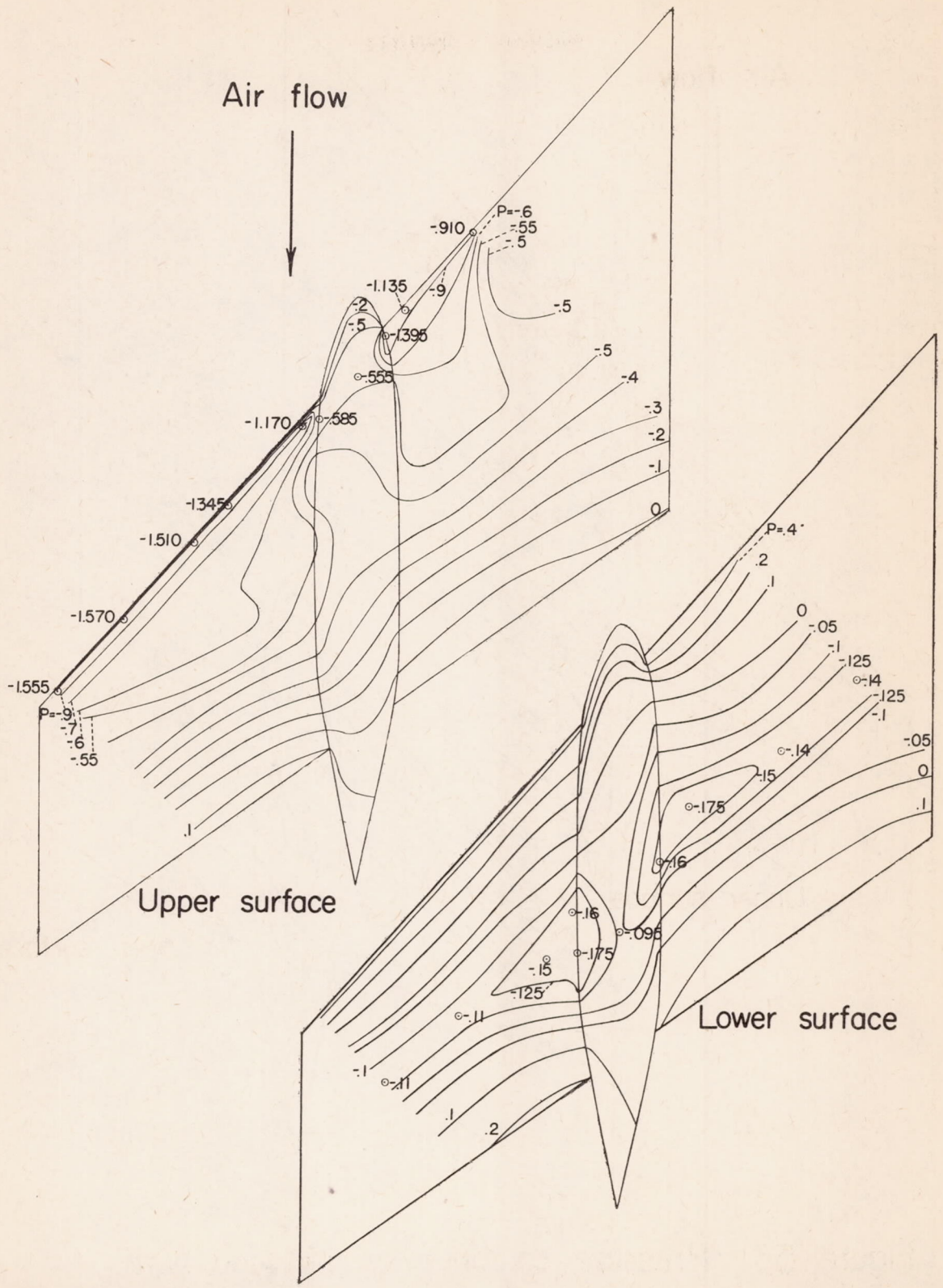


Figure 52.—Pressure contours for the wing-nacelle combination $\Lambda=45°$; $C_L=0.40$; $M=0.61$.

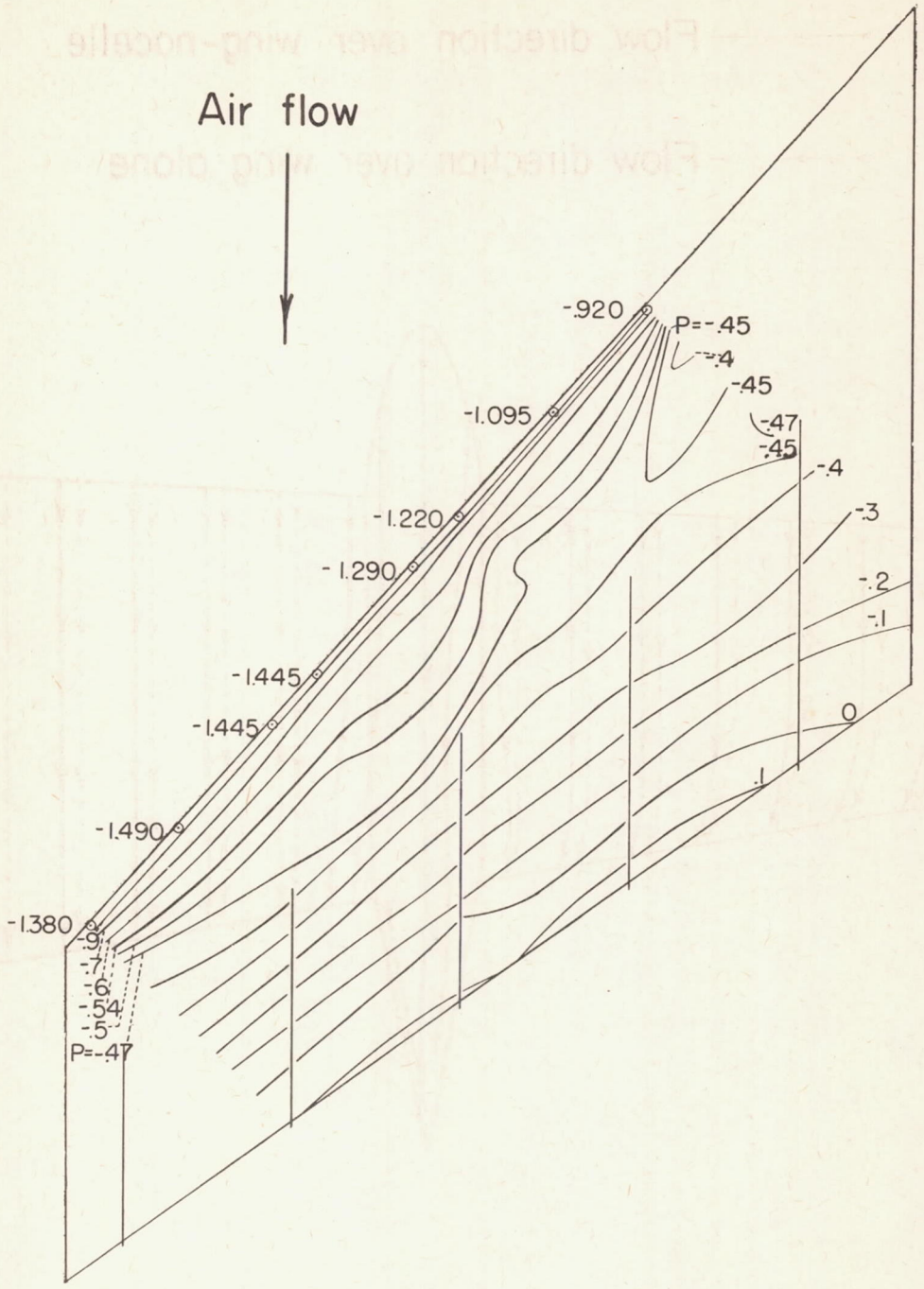


Figure 53.–Pressure contours for the wing with vertical plates on the upper surface.

$\Lambda = 45°$; $C_L = 0.40$; $M = 0.20$.

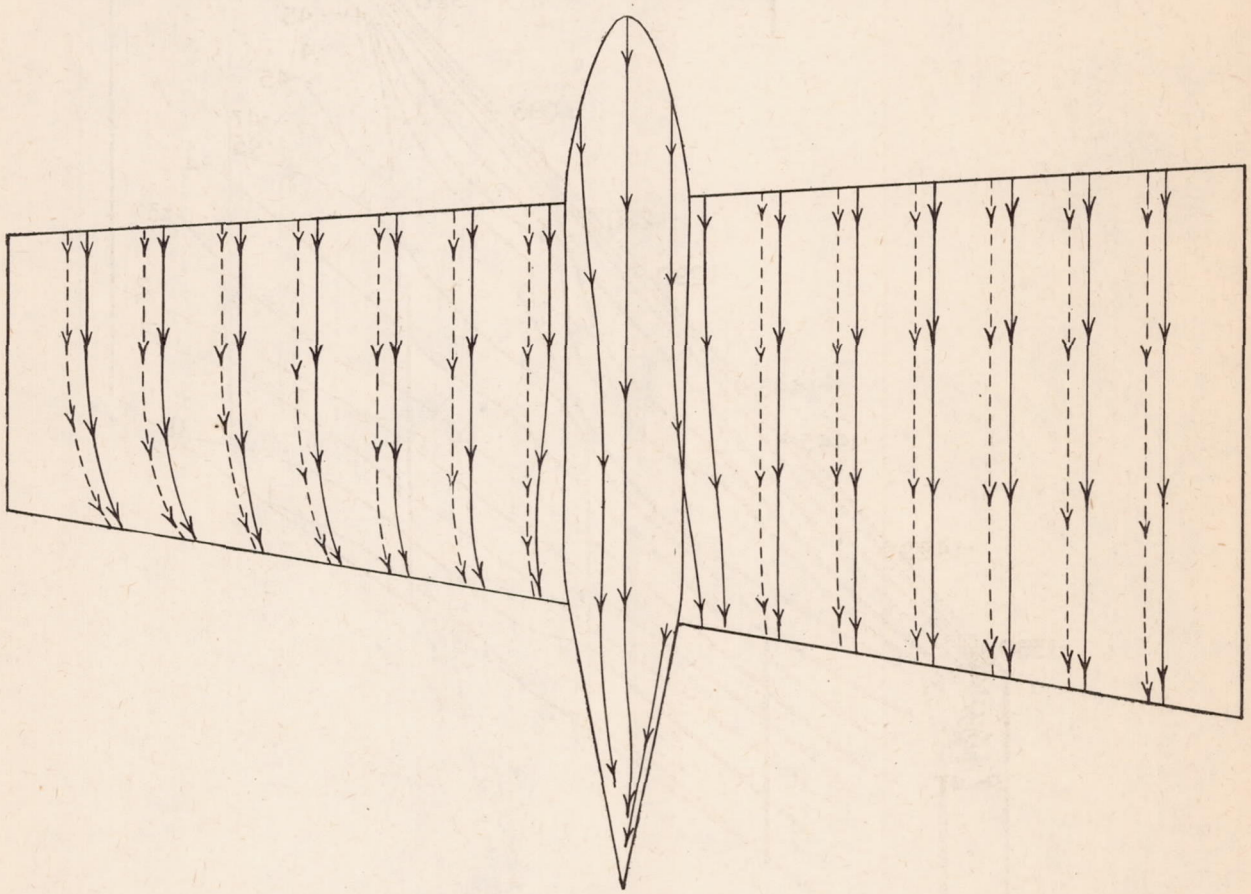


Figure 54.—Flow patterns over the wing and wing-nacelle combination. $\Lambda = 0°$; $\alpha_g = 4°$; $M = 0.13$.

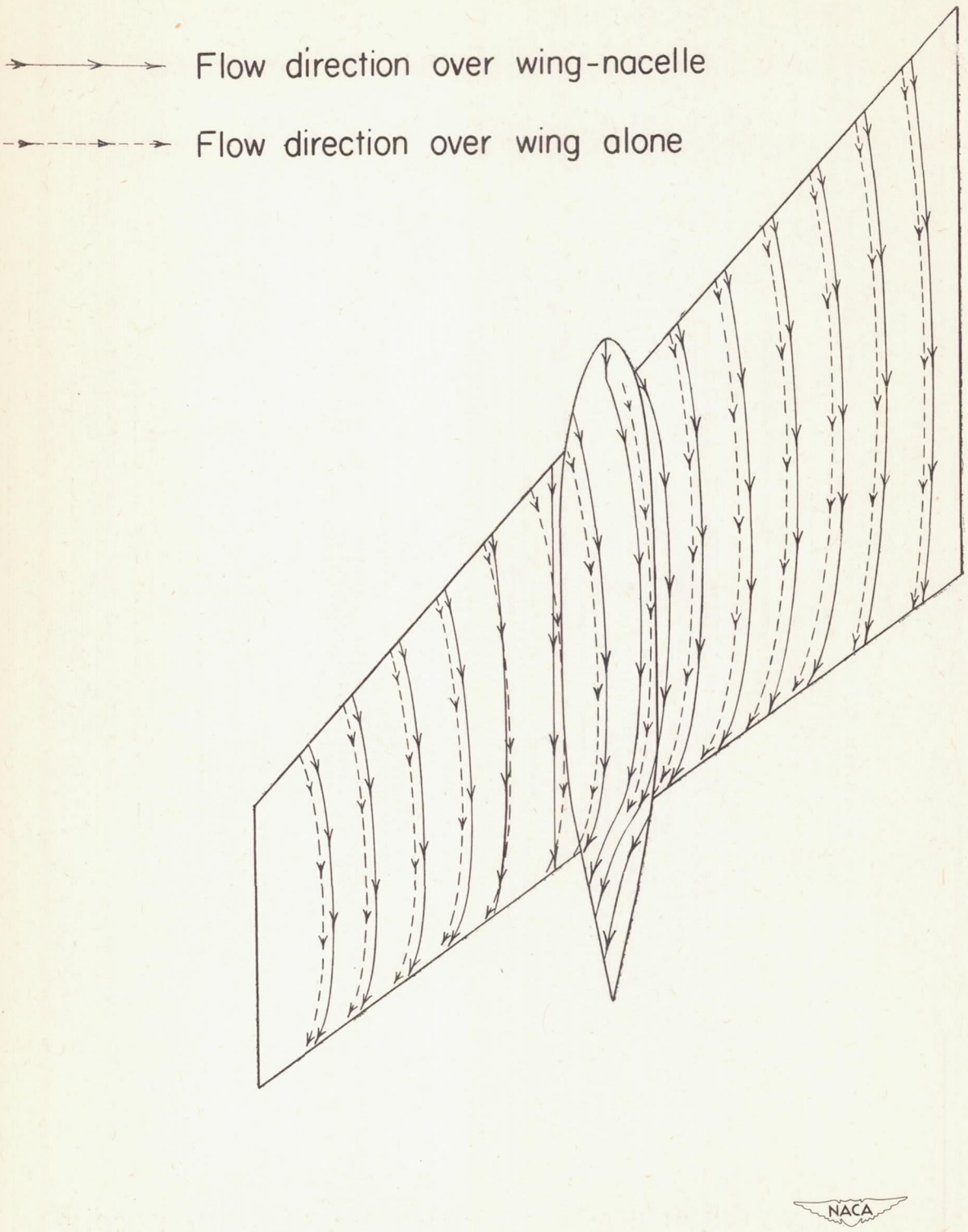


Figure 55.— Flow patterns over the wing and wing-nacelle combination. $\Lambda = 45°$; $\alpha_g = 7°$; $M = 0.13$.

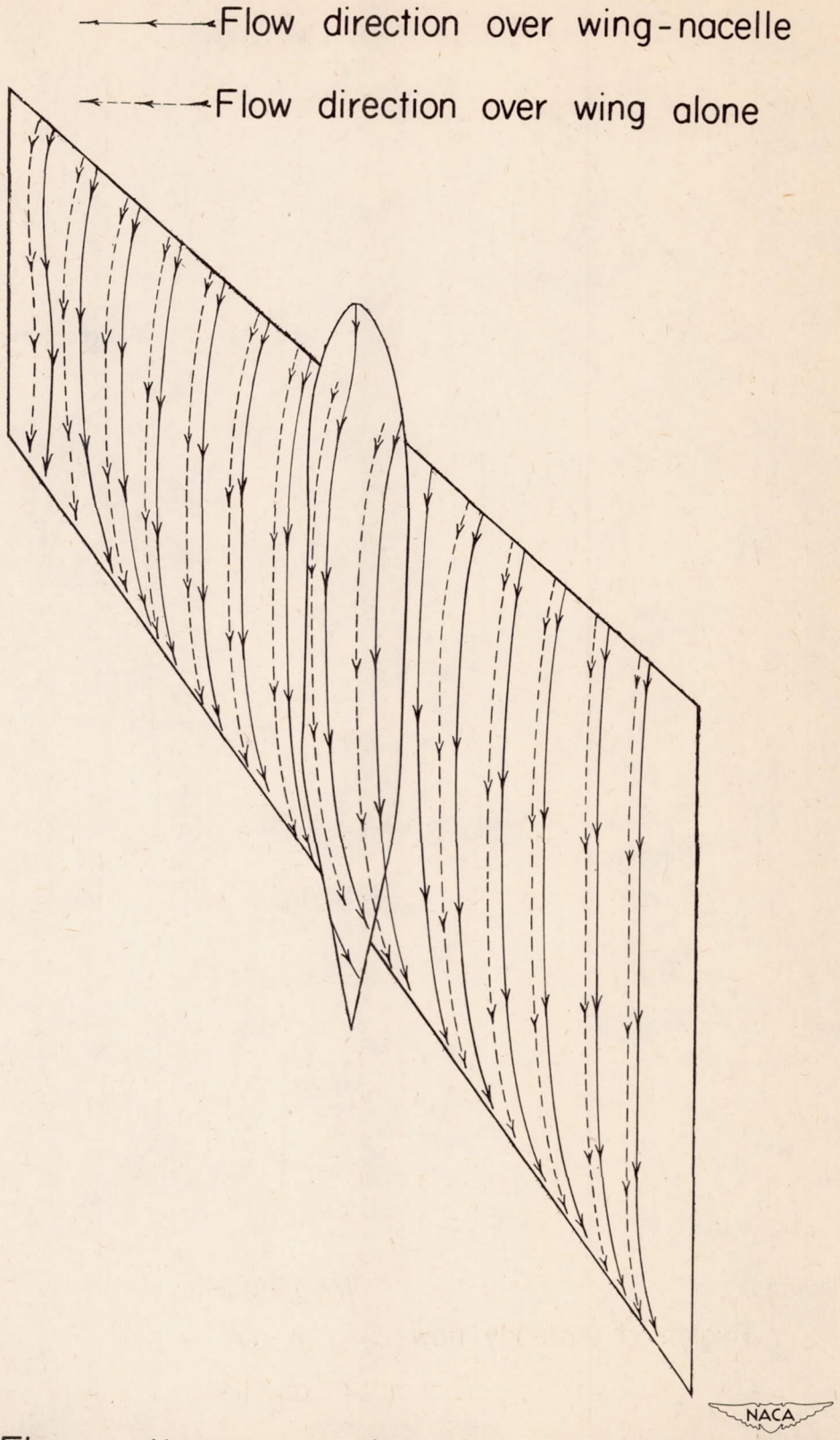


Figure 56.—Flow patterns over the wing and wing-nacelle combination. $\Lambda = -45°$; $\alpha_g = 9°$; $M = 0.13$.

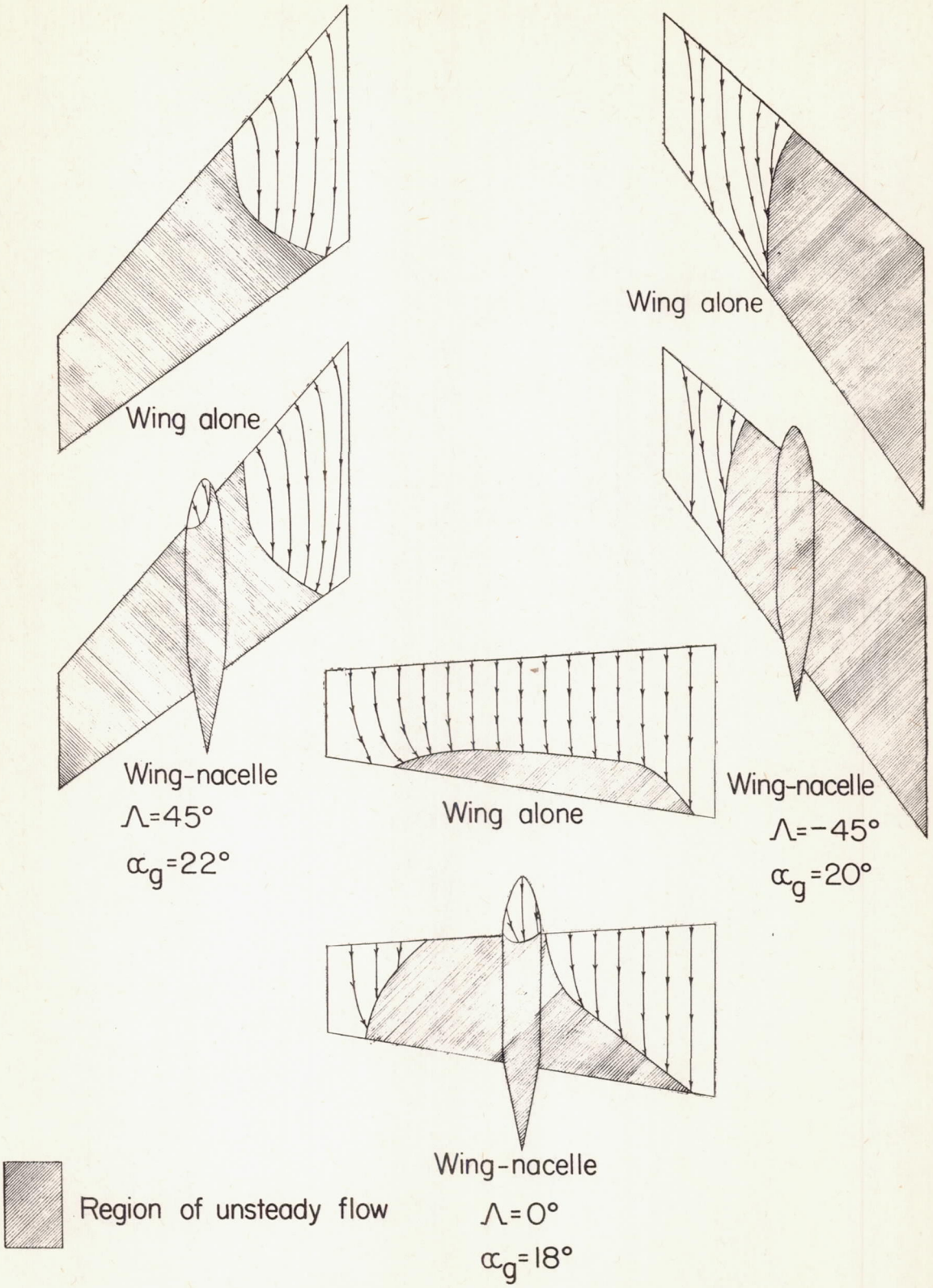


Figure 57.—Flow patterns over the wing and wing-nacelle combination. M=0.13

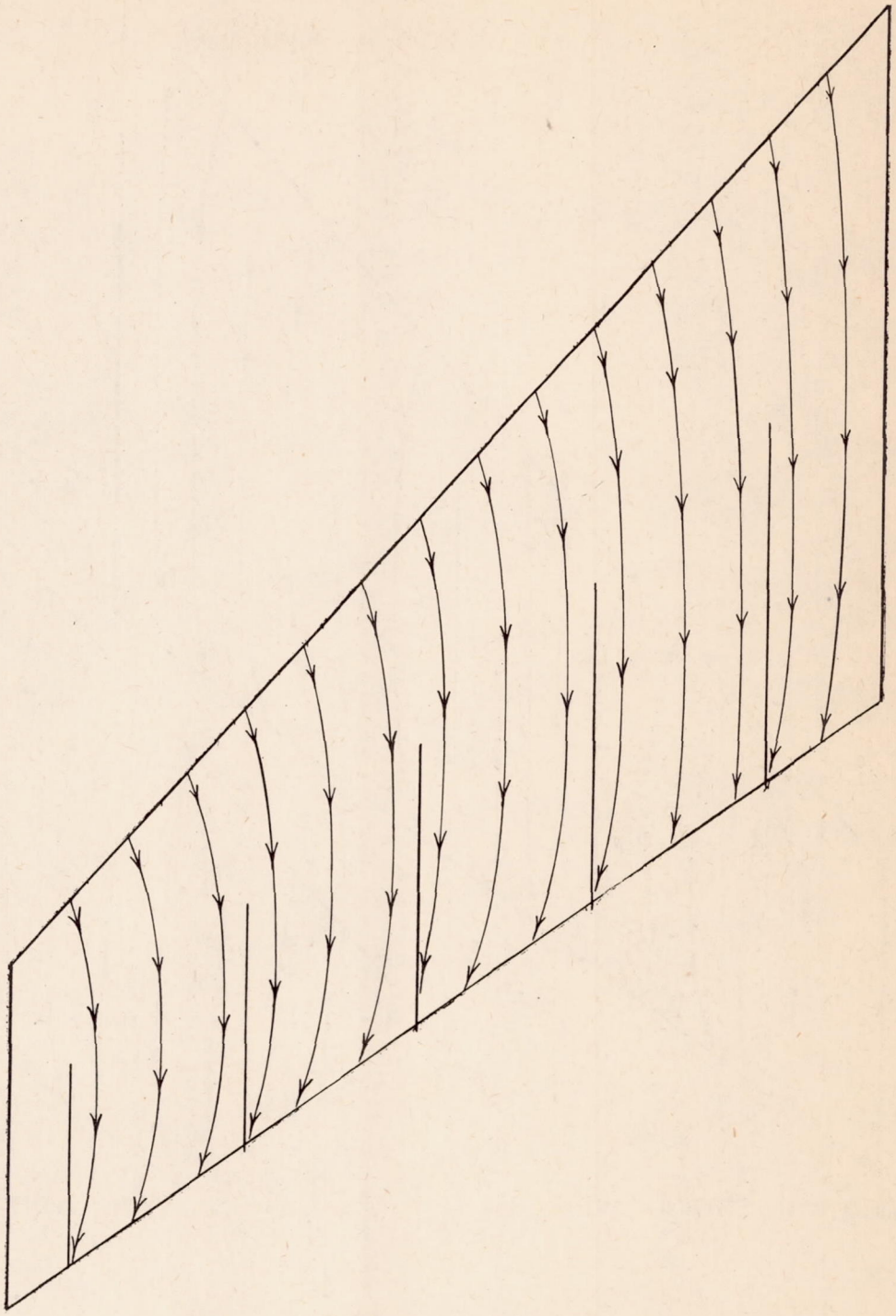


Figure 58 .—Flow patterns over wing upper surface with vertical plates installed. $\Lambda = 45°$; $\alpha_g = 6°$; M=0.13.

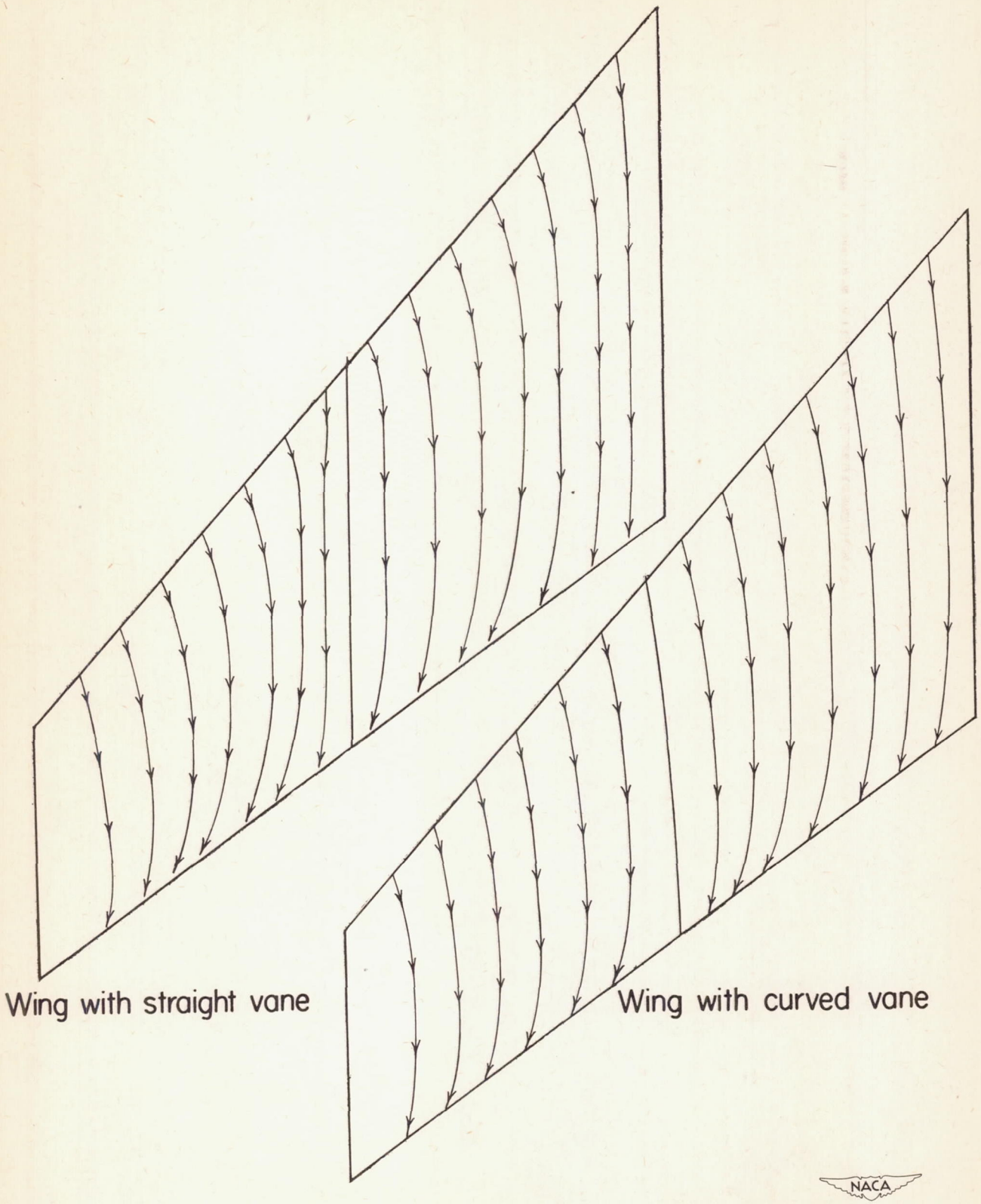


Figure 59.—Flow patterns over the wing with a straight vane and a curved vane at the midsemispan. $\Lambda = 45°$; $\alpha_g = 6°$; $M = 0.20$.